UPPSALA
UNIVERSITET

Immobilisation of Ru-Based Molecular Catalysts for Electrochemical Water Oxidation

ANDREW HOWE

Dissertation presented at Uppsala University to be publicly examined in Polhemsalen, Lägerhyddsvägen 1, 751 20, Uppsala, Friday, 28 October 2022 at 09:15 for the degree of Doctor of Philosophy. The examination will be conducted in English. Faculty examiner: Professor Javier Concepcion (Brookhaven National Laboratory).

Abstract

Howe, A. 2022. Immobilisation of Ru-Based Molecular Catalysts for Electrochemical Water Oxidation. *Digital Comprehensive Summaries of Uppsala Dissertations from the Faculty of Science and Technology* 2190. 131 pp. Uppsala: Acta Universitatis Upsaliensis. ISBN 978-91-513-1598-0.

Artificial photosynthesis requires catalysts for efficient and selective conversions of small molecules. Molecular catalysts are advantageous to use in these instances as they offer precise control over chemical reactivity. They are synthetically tuneable, and their catalytic mechanisms are often well documented and more readily understood than those of solid-state catalysts. In this thesis, the synthetic incorporation of molecular catalysts into heterogenised molecular anodes for water oxidation are evaluated. The catalysts are incorporated as structural linkers into porous metal-organic framework (MOF) structures, and as coordination oligomers stacked onto graphitic surfaces.

The preparation of MOF/molecular catalyst hybrid materials of two topologies, UiO (UiO = Universitet i Oslo) and NU-1000 (NU = Northwestern University), were investigated. Multiple synthetic methods for the incorporation of molecular ruthenium-based catalysts into MOFs were examined in papers I and II. In paper III of this thesis, a Ru-bda type molecular complex was successfully used in the solvothermal synthesis of a new MOF. The resulting material is the first of its kind that is built exclusively from molecular water oxidation catalyst linkers. It is shown that MOF incorporation greatly enhances the structural stability of the catalyst linker in chemical water oxidation experiments, giving rise to higher turnover numbers compared to that of a homogenous reference system. Finally, paper IV describes a stable and inert molecular ruthenium complex, which possesses a flexible adaptive multidentate equatorial (FAME) type equatorial ligand with a carbanion on the equatorial ligand that forms a C-Ru bond. This molecular complex is studied in homogeneous phase, and subsequently incorporated into a coordination oligomer, which can be activated for water oxidation catalysis. This finding broadens the field of molecular catalysis significantly, and proves that supramolecular interactions can be used to promote electrocatalysis in complexes which are otherwise too inert and stable to engage in electrocatalytic reactions.

Keywords: Molecular Catalysis, Metal-Organic Frameworks, Water Oxidation, Post-Synthetic Exchange, Electro-chemistry.

Andrew Howe, Department of Chemistry - Ångström, Synthetic Molecular Chemistry, 523, Uppsala University, SE-751 20 Uppsala, Sweden.

Science cannot solve the ultimate mystery of nature, and that is because in the last analysis, we ourselves are a part of the mystery that we are trying to solve.

Max Planck

List of Papers

This thesis is based on the following papers, which are referred to in the text by their Roman numerals.

I. **Synthetic strategies to incorporate Ru-terpyridyl water oxidation catalysts into MOFs: direct synthesis vs. post-synthetic approach**

Timofey Liseev, Andrew Howe, Md Asmaul Hoque, Carolina Gimbert-Suriñach, Antoni Llobet and Sascha Ott., *Dalton Trans.*, **2020**, 49, 13753-13759.

Author's contribution: Was involved in synthesis and characterisation of molecular complex. Carried out the initial direct synthesis experiments for the MOF, performed electrochemical analyses on MOF materials and contributed to manuscript writing and editing.

II. **Electrocatalytic water oxidation from a mixed linker MOF based on NU-1000 with an integrated ruthenium-based metallo-linker**

Andrew Howe, Timofey Liseev, Marcos Gil-Sepulcre, Carolina Gimbert-Suriñach, Jordi Benet-Buchholz, Antoni Llobet and Sascha Ott., Mater. Adv., **2022**, 3, 4227-4234

Author's contribution: Led the project, performed all synthetic work, performed all analyses except SEM and carried out all electrochemical analysis, including water oxidation experiments. Wrote and edited the manuscript.

III. Synthesis of a Metal-Organic Framework Made Entirely of the Molecular Ruthenium Water Oxidation Complex

Andrew Howe, Erik Sikma, Ryan Dodson, Seth Cohen and Sascha Ott., *Manuscript in preparation*

Author's contribution: Led the project, performed synthesis and characterisation of complex, metal-organic framework and thin film on gold plate and GC plate. This characterisation included SEM, PXRD and all electrochemical characterisation in bulk and on a thin film and all electrochemical and chemical water oxidation experiments. Wrote and edited the manuscript.

IV. Carbanion Ruthenium Complexes for Water Oxidation

Andrew Howe, Marcos Gil-Sepulcre, Carolina Gimbert-Suriñach, Dooshaye Moonshiram, Anders Thapper, Antoine Bousquet, Laurent Billon, Sascha Ott, Antoni Llobet., *Manuscript in preparation*

Author's contribution: led the project, performed all synthetic work, performed all analyses except XANES, and wrote and edited the manuscript.

Reprints were made with permission from the respective publishers.

Papers not included in this thesis

V. Robust and Efficient Screen-Printed Molecular Anodes with Anchored Water Oxidation Catalysts

Robin N. Dürr, Sirikorn Chasvised, Marcos Gil-Sepulcre, Andrew Howe, Md Asmaul Hoque, Van N'Guyen, Saeed Sadeghi, Stephanie Reynaud, Cyril Cugnet, Laurent Authier, Carolina Gimbert-Suriñach, Antoine Bousquet, Antoni Llobet, and Laurent Billon., *ACS Appl. Energy Mater.* **2021**, 4, 10, 10534–10541.

Author's contribution: Carried out the water oxidation experiments of the printed electrode.

Contents

Abbreviations

α	alpha
Ω	omega
bdc	benzenedicarboxylic acid
bipy	4,4'-bipyridine
bda	2,2'-Bipyridine-6,6'-dicarboxylic Acid
BET	Brunauer-Emmett-Teller
CN	cyanide
CNT	carbon nanotubes
CV	cyclic voltammetry/voltammogram
DEF	diethylformamide
DMA	dimethylacetamide
DMF	dimethylformamide
DMSO	dimethylsulfoxide
Dpa	((5-methyl-1,3-phenylene)bis(pyridine-6,2-diyl))bis(phosphonic acid)
Edba	4,4'-ethynedibenzoic acid
EDX	energy-dispersive X-ray spectroscopy
GC	glassy carbon electrode
HER	hydrogen evolution reaction
ICP-OES	inductively coupled plasma-optical emission spectroscopy
Ina	iso-nicotinic acid
IPCC	Intergovernmental Panel on Climate Change
LbL	layer-by-layer
MOF	metal-organic framework
MWCNT	multi-walled carbon nanotubes
NHE	normal hydrogen electrode
NMR	nuclear magnetic resonance
NU	Northwestern University
phbs	Phosphate Buffer Solution
PSE	post-synthetic exchange
PSI	post-synthetic insertion
PXRD	powder X-ray diffraction
Py	pyridine
PyR	pyridine derivative
Py(PhCOOH)	4,4'-(pyridine-3,5-diyl)dibenzoic acid
SALE	solvent-assisted linker exchange

SALI	solvent-assisted ligand insertion
SAM	self-assembled monolayer
SBU	secondary building unit
SEM	scanning electron microscopy
SLI	sequential linker installation
SURMOF	surface-mounted metal-organic framework
H$_4$TBAPy	(1,3,6,8-pyrenetetrayl)tetrakis-benzoic acid
Tda	2,2':6',2''-terpyridine-6,6''-dicarboxylic acid
UiO	Universitet i Oslo
UNECE	United Nations Economic Commission for Europe
WO	water oxidation
WOC	water oxidation catalyst
WWCNT	Multi-wall Carbon Nanotubes
XPS	X-ray photoelectron spectroscopy
XRD	X-ray diffraction

Symbols

Symbol	Meaning	Standard Unit
C_i	Concentration of species i	M, mol cm^{-3}
C_{Ru}^o	Total concentration of molecular Ru catalyst within MOF	M, mol cm^{-3}
C_A^o	Bulk concentration of solution species A	M, mol cm^{-3}
C_P^o	Total electroactive concentration of redox active linker, P	M, mol cm^{-3}
C_P^*	Total concentration of redox-active linker, P	M, mol cm^{-3}
C_S^o	Bulk concentration of substrate	M, mol cm^{-3}
d_f	Film thickness	cm
D_i	Diffusion coefficient of species i	cm^2 s^{-1}
D_e	Electron hopping diffusion coefficient for charge transport	cm^2 s^{-1}
D_s	Intra-MOF diffusion coefficient of substrate	cm^2 s^{-1}
E	Electrode potential	V
E_i	Initial potential	V
E_P	Peak potential	V
$E_{P/2}$	Potential at half peak current	V
ΔE_P	Peak potential separation	V
E^o	Standard potential	V
$E^{o\prime}$	Formal potential	V
$\boldsymbol{F}_i$	Molar flux of species i	mol cm^{-2} s^{-1}
F	Faraday Constant	C mol^{-1}
i	Current	A
i_p	Peak current	A
i_{pa}	Peak anodic current	A
i_{pc}	Peak cathodic current	A
i_A	Characteristic current density for substrate diffusion in solution	A cm^{-2}
i_s	Characteristic current density for substrate diffusion within film	A cm^{-2}
i_e	Characteristic current density for diffusional charge transport	A cm^{-2}

i_k	Characteristic current density for catalytic reaction	A cm^{-2}
j	Current density	A cm^{-2}
k	Second order rate constant of chemical step	M^{-1} s^{-1}, cm^3 mol^{-1} s^{-1}
k_s	Standard interfacial rate constant	cm s^{-1}
k_f	Forward interfacial electron transfer rate constant	cm s^{-1}
k_b	Backward interfacial electron transfer rate constant	cm s^{-1}
k_{ox}	Overall second order rate constant for O$_2$ release step	M^{-1} s^{-1}, cm^3 mol^{-1} s^{-1}
k_{oxj}	Second order rate constant of the jth oxidation state reaction	M^{-1} s^{-1}, cm^3 mol^{-1} s^{-1}
k_{wna}	Second order rate constant of water nucleophilic attack	s^{-1}
K_{O_2}	First order rate constant for O2 release step	s^{-1}
k_{cat}	Observed catalytic rate constant	s^{-1}
k_i	Rate of consumption/production of species i by chemical reaction steps	M s^{-1}, mol cm^{-3} s^{-1}
N_A	Avogadro constant	mol^{-1}
R	Ideal Gas Constant	J K mol^{-1}
S	Surface area	cm^{-2}
t	Time	s
T	Temperature	K
TOF	Turn Over Frequency	S^{-1}
TON	Turn Over Number	n.a.
v_{O_2}	Total production rate of O$_2$	mol s^{-1}
$v_{O_2}^{max}$	Maximum production rate of O$_2$	mol s^{-1}
Γ_i^o	Electroactive surface coverage of species i	mol cm^2
Γ_i^*	Total surface concentration of species i	mol cm^{-2}
δ_{rxn}	Reaction-diffusion layer thickness	cm
δ	Diffusion layer thickness	cm
η	Overpotential	V
n^{e-}	Number of Electrons	C
k_S	Partition equilibrium constant for substrate crossing MOF film-solution interface	n.a.
v	Scan rate	V s^{-1}
∇^2	Laplacian operator	n.a.
Q	Charge	C

1 Introduction

1.1 Natural Photosynthesis

Photosynthesis is the process in which green plants, algae and cyanobacteria store the energy from the sun in the form of chemical bonds. In this process, the energy gathered from sunlight is utilised to oxidise water into dioxygen, which is released into the environment as a by-product. Generated protons and electrons are ultimately combined with carbon dioxide to form carbohydrates. The overall reaction is summarised in Figure 1.1.

Figure 1.1. *Simplified equation for the process of natural photosynthesis.*

Nature has evolved various enzymes to catalyse key transformations in natural photosynthesis. Oxidation of water takes place in a complex protein system called photosystem II (PSII) and, more specifically, in its oxygen evolution centre (OEC). PSII is situated in the thylakoid membrane together with cytochrome b6f, photosystem I (PSI) and ATP synthase, which are the responsible for the formation NADPH and ATP.

The process of photosynthesis starts with the adsorption of sunlight by chlorophyll P680 and pigments in PSII. The excited P680* engages in an electron transfer to pheophytin (pheo), which generates a charge separated state with the highly oxidising species P680*$^+$. This species provides the driving force for the oxidation of a nearby tyrosine residue (Yz), which is responsible for abstracting one electron from the OEC.[1] This process is repeated four times to accumulate enough oxidising equivalents to oxidise water. The electrons that are produced in the process are channelled away from P680 through an electron transport chain, ultimately arriving at PSI (Figure 1.2.).

In PSI, NADPH (Nicotinamide Adenine Dinucleotide Phosphate) as a hydrogen carrier is produced from NADP$^+$, as well as the energy vector molecule

ATP (Adenosine Triphosphate). Afterwards, NADPH and ATP will be used for fixing atmospheric CO_2 in the stroma of the chloroplast.[2, 3]

Many XRD, XAS and DFT studies have been carried out to determine the structure of the OEC responsible for water oxidation in natural systems.[4] These studies show that the OEC is comprised of a Mn_4CaO_5 cluster. The calcium and three of the four manganese cations are bridged by oxo species to form a cubane structure, with the fourth manganese centre being linked to two Mn cations of the cubane through μ-oxo bridges. Amino acid residues from the surrounding peptide backbone, as well as water molecules, Complete the coordination sphere around the cluster (Figure 1.3).[5]

1.2 Artificial Photosynthesis Devices

Artificial photosynthesis deals with the use of sunlight in order to oxidize water (eq. 1) with the aim of using the released H^+ and e^- for reducing either H^+, CO_2 or N_2 into H_2, hydrocarbons or NH_3 (eq 2-4). Conversion of solar energy to chemical energy effectively stores the energy for later use, hence has potential for applications in renewable energy.

$$2H_2O \rightarrow O_2 + 4e^- + 4H^+ \qquad \textbf{eq. 1}$$

$$4e^- + 4H^+ + CO_2 \rightarrow [CH_2O] + H_2 \qquad \textbf{eq. 2}$$

$$4e^- + 4H^+ \rightarrow 2H_2 \qquad \textbf{eq. 3}$$

$$4e^- + 4H^+ + \frac{2}{3}N_2 \rightarrow \frac{4}{3}NH_3 \qquad \textbf{eq. 4}$$
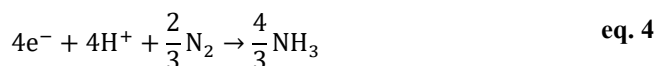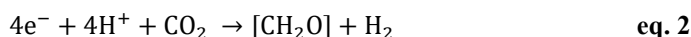
The splitting of two water molecules to produce hydrogen is the result of two coupled half-reactions, the oxidation of the water (eq. 1) and the reduction of the generated protons to molecular hydrogen using the released electrons (eq. 3). Treating water-splitting as two separate half reactions allows rational design and optimisation of catalysts for the cathode and anode materials Artificial photosynthetic devices have been developed using three different approaches,[6] which are photovoltaic electrolyser cells (PV/electrolyser), photoelectrochemical cells (PECs) and mixed colloid devices (Figure 1.4).[7]
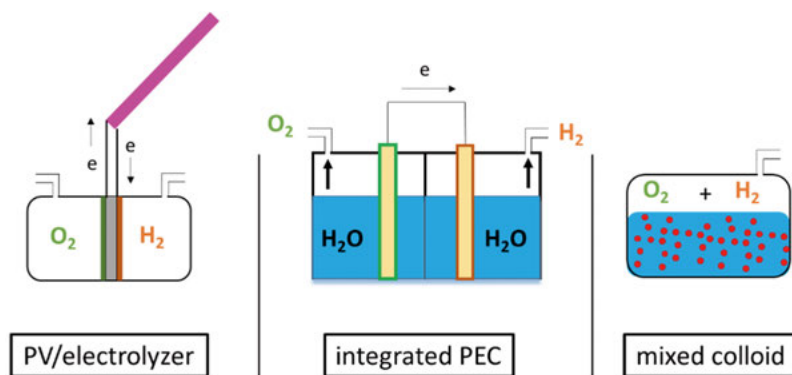
Figure 1.4. *Artificial photosynthetic devices for hydrogen production. Left is the PV/electrolyser, centre is the photoelectrochemical cell and right is the mixed colloid device. Reprinted with permission from the American Chemical Society. J. R. McKone et al / Chem. Mater.* ***2014***, *26, 1, 407 – 414.*

The PV/Electrolyser design consists of two autonomous devices; a commercial PV cell as light absorber, which is connected to the water oxidation and proton reduction catalysts. The main advantage is the large amount of PV cells and heterogeneous catalysts that are available. One of the main problems for large-scale applications is the high costs of PV cells. An alternative design is found in mixed colloids, where the photosensitizer and catalyst are integrated in particles and suspended in an electrolyte. Although this is a low-cost alternative, these systems are not yet viable and require improvements in solar to hydrogen efficiencies.

PECs represent a balance between the efficiency and viability of PV/electrolyser cells and the simplicity of mixed colloids. These types of cells consist of separate photoanodes and photocathodes which are connected by a separate junction. The anode compartment contains an electrode with photosensitive material capable of adsorbing photons from sunlight and provoke charge separation (n-type), and a water oxidation catalyst which is often based on metal oxides or anchored molecular catalysts. The cathode compartment consists of a p-type photosensitive material and a hydrogen evolution catalyst.

A membrane junction physically separates the two compartments and allows the flow of protons from the anode to the cathodes. Under operation, absorption of a photon by the photosensitive semi-conductive material, results in the excitation of an electron from the valence band to the conduction band, creating an electron-hole pair. The electron is going to the back contact and ultimately through the external circuit to the cathode, while the holes accumulates oxidative equivalents to the anode catalyst. This is regenerated by the WO catalyst, which accumulates oxidative equivalents. When four oxidative equivalents are accumulated, water oxidation can take place. At the same time, light (preferably of a different wavelength) is absorbed by the cathode semiconductor, leading to other electron-hole pair. The holes combine with the electrons from the anode, while the electrons accumulate at the reduction catalyst to reduce protons to molecular hydrogen.

In an ideal case, new components such as light absorbers or catalysts should be studied in such a device context. For practical reasons, this is normally not the case, and newly designed catalysts studied independently by using sacrificial electron donors and acceptors as replacements of the anode and cathode, respectively. Newly designed catalysts are often studied without the limiting light reaction, using chemical oxidants or reductants in dark reactions.

The most common sacrificial oxidants that are used in the context of water oxidation are cerium ammonium nitrate (CAN), $[Ru(bpy)_3]^{3+}$, potassium periodate or potassium peroxymonosulfate (OXONE) while ascorbic acid or trimethylamine (TEA) are the most common reductants for the hydrogen

evolution reaction. Electrochemically triggered WO and HER processes have also been extensively studied during the last years, providing fast and simple setups for analysing the catalytic performance of new catalysts.

1.3   Water Oxidation Catalysts

The oxidation of two molecules of H_2O requires the transfer of four electrons, the breaking of four O-H bonds and the formation of an O=O bond. Due to its molecular complexity, the oxidation half reaction is currently the bottleneck of this process for developing an efficient and robust water splitting device.

Moreover, it's a thermodynamically highly demanding reaction ($E° = 1.23$ V vs. NHE at pH= 0), that depending on the catalyst, can exhibit high activation barriers for some of the elementary steps. Thus, a catalyst capable of accumulating four oxidative equivalents and operating close to the thermodynamic WO potential is necessary. Besides, an ideal WO catalyst must be able to interact with photosensitizing materials and be stable in water at high oxidation states to avoid degradation during catalysis.

1.4   Mechanism of Water Oxidation Catalysis

An important factor for the design of molecular water oxidation are the mechanisms by which they operate. Transition metals in their high oxidation states containing the M-O group can be described using two resonance forms, depending on whether the oxidation involved predominantly the metal centre or at the oxygen. Water oxidation complexes usually have two possible pathways of operation, which water nucleophilic attack (WNA) or interaction of two M-O units (I2M) (Figure 1.5.).

A WNA mechanism is found when the auxiliary ligands favour the stabilisation of the peroxo intermediate. The mechanism usually begins with a Ru-aqua species. At this point, an incoming water molecule from the solvent attacks the M=O bond via nucleophilic attack to generate an intermediate hydroperoxide species. The formation of the hydroperoxide intermediate from $Ru^{(V)}$ is followed by another two electron reduction to generate a [$Ru^{(III)}$-OOH] species.[8] The solvent water molecules also have additional affects, as the presence of two or three water molecules lowers the transitional energy of the O-O bond formation step via creation of a network of H-bonds, whilst also acting as a base to promote proton shuttling.[9] The I2M mechanism involves a radical coupling, when the oxidation state of the metal centre is unchanged and when the favoured species resembles the oxyl radical form.[10]
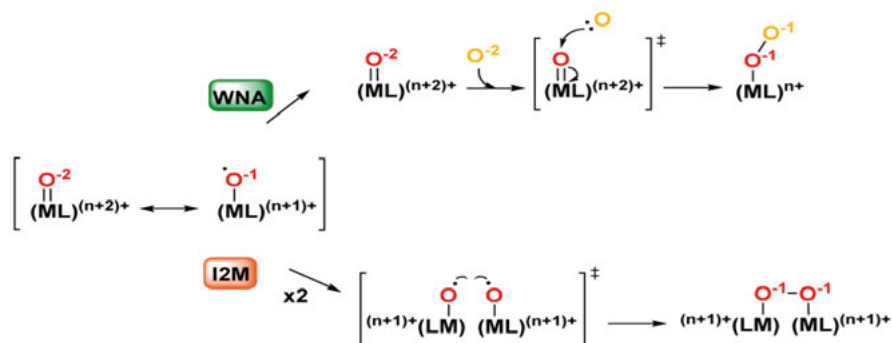
Figure 1.5. *Illustration of the two standard mechanisms of water oxidation. The water nucleophilic attack mechanism illustrated above involves water acting as a nucleophile, with a generation of a hydroperoxide intermediate. I2M mechanism of water oxidation involves radical coupling, with two metal atoms interacting via an μ-oxo-bridge. Reprinted with permission from the American Chemical Society. I. Funes-Ardoiz et al / ACS Catal.* **2017,** *7, 3, 1712 – 1719.*

1.5   Proton-Coupled Electron Transfer (PCET) In Ru-Based Molecular Complexes

Ruthenium is located in the second row of the d-block transition metal series. Its electronic configuration $4d^7\ 5s^1$ gives access to the widest variety of oxidation states, ranging from (+8) as in RuO_4 to (-2) in $[Ru(CO)_4]^{2-}$, which equate to d^0 and d^{10} electronic configurations.

When combined with polypyridyl ligands, ruthenium complexes are generally stable at high oxidation states and its octahedral geometry allows a tailor-made fine tuning of their redox potentials. All these properties make ruthenium polypyridyl complexes appealing candidates as catalyst for oxidation reactions, including water oxidation as well as the oxidation of other organic and inorganic compounds.[11-13]

An interesting redox behaviour can be found when a water molecule is directly bonded to a metal centre. Upon oxidation, the metal-aqua complex often loses a proton, giving rise to proton-coupled electron transfer (PCET) reactions. This redox behaviour was described by Thomas J. Meyer in 1970, and has been extensively studied for the case of ruthenium aqua complexes.[14, 15]

This also occurs in other transition metal complexes which can facilitate the four electron transfers necessary for water oxidation. The loss of each electron is coupled to the loss of one proton, which is facilitated by the increase of the acidity of the aqua ligand due to its ligation to a Lewis acidic transition metal.

$$[M^{n+}(O)] \xrightarrow[ET]{+e^-} [M^{(n-1)+}(O)]^-$$

$$PT \downarrow +H^+ \qquad CPET \qquad PT \downarrow +H^+$$
$$H^+ + e^-$$

$$[M^{n+}(OH)]^+ \xrightarrow[ET]{+e^-} [M^{(n-1)+}(OH)]$$
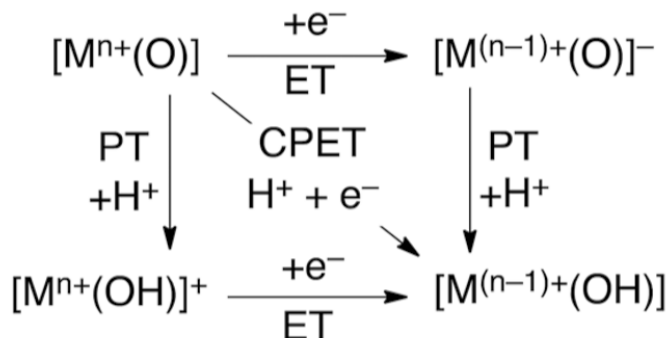
Figure 1.6. *Illustration of the proton-coupled electron transfer (PCET) process, in comparison to single, concerted electron transfer and proton transfer processes.*

PCET effectively allows the total charge of the complex to remain constant throughout the multi-redox process, thus avoiding the formation of high-energy intermediates due to charge accumulation.[16] This charge equilibration results in a decreased energy input, and thus overpotential requirement to reach highly oxidising species. The dependence of the $E_{1/2}$ redox potentials as a function of pH variation follows the Nernst equation. Thus, for a one electron/one proton transfer process, the multi-redox potential diminishes by 59mV per pH unit.

The redox properties of ruthenium polypyridyl complexes, in particular the $Ru^{(III/II)}$ and $Ru^{(IV/III)}$ redox couples are strongly influenced by the nature of the ligands surrounding the metal centre. The $Ru^{(II)}$ state is stabilised by Ru d-π-ligand π^* back-bonding interactions thanks to the presence of π electron-rich systems, while the $Ru^{(III)}$ state is stabilised by the electron-donating characteristics of the oxygen-containing ligands that diminish the necessary potential to reach the $Ru^{(III)}$ state.[17]

In the case of the $Ru^{(III/II)}$ redox couples, this is less sensitive to ligand modification in comparison with the $Ru^{(IV/III)}$ couples. This phenomenon is due to the control on the π-binding properties exerted by the oxo ligand of the $Ru^{(IV)}$=O species through a d-π-Ru interaction. In conclusion, the ability to accumulate high oxidation states in a narrow potential window utilising PCET reaction in metal aqua complexes is key for the development of WOCs.

1.6 Water Oxidation with Multiple Ruthenium Centres

One of the first molecular complexes capable of accumulating four oxidising equivalents and oxidising water was reported in the 1980s by Meyer and coworkers (Figure 1.7.).[16, 18, 19] Llobet[20] subsequently prepared a modification involving a 3,5-bis(2-pyridyl)pyrazolate (bpp-) bridging ligand that brings two Ru-bound water ligands in close proximity, which is a structural prerequisite for their coupling at high oxidation states via an I2M mechanism.

Owing to the conjugated nature of the bpp ligand, the electronic communication between the two metal centres is improved relative to the early example from Meyer. Despite the TOF being increased by a factor of 3 in the bridged complexes, these early examples have moderate catalytic performances with a maximum turnover number of 17.5 and relatively low efficiency (70% relative to the sacrificial oxidant).

This behaviour is attributed to the oxidation of the CH group of the pyrazole moiety present in the bridging ligand. Introduction of an extra methyl group in the pyrazole ring stabilises the complex under WO conditions, improving efficiencies up to 90%.[18, 19]

Cis,cis-[(bpy)$_2$(H$_2$O)Ru^{III}(μ-O)Ru(H$_2$O)(bpy)$_2$]$^{4+}$
1

In,in-{{(Ru^{II}(trpy)(H$_2$O)}}$_2$(μ-bpp)}$^{3+}$
2

{(Ru^{II}(Py)$_2$(H$_2$O)}$_2$(μ-Mebbp)}$^+$
3
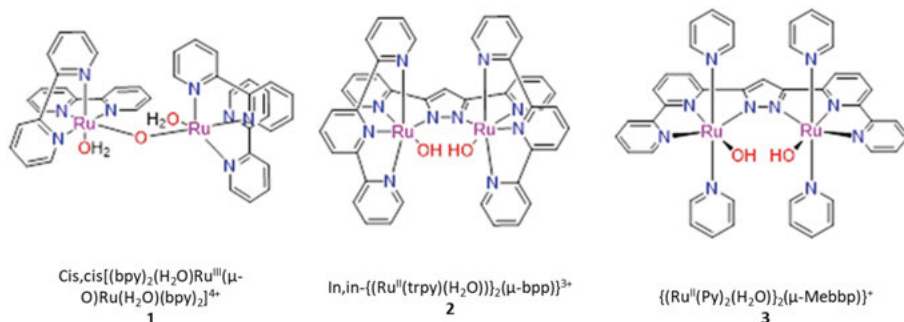
Figure 1.7. Examples of complexes with an electronic communication between the two metal centres through a conjugated bridge.

1.7 Single-Site Water Oxidation Catalyst

This field of molecular WOCs made a big step forward in 2004, when Thummel reported for the first time that the four-electron transfer steps that are necessary for oxidising water could occur on a single-site metal complex (Figure 1.8.).[21, 22] This group published the first family of mononuclear complexes bearing the tridentate polypyridyl ligand 2,6-di(1,8-naphthyridin-2-yl)pyridine capable of catalysing water oxidation, albeit with moderate performance.

It was not until later that Meyer and co-workers reported a thorough mechanistic study that demonstrated the mononuclear nature of the catalyst.[8] The proposed catalytic cycle has been later adapted for several catalysts, which are proposed to follow a WNA mechanism.[23-25]

From 2009 onwards, Sun and co-workers have reported a series of mononuclear complexes based on the bda^{2-} ligand (H$_2$bda is [2,2'-bipyridine]-6,6'-dicarboxylic acid).[26] These complexes showed the best catalytic activity reported till that point, achieving the impressive TON and TOF values of 8360 and 303 s^{-1}, respectively. The strong electron-donating ability of the carboxylate moieties present in the bda^{2-} ligand,[27] the expansion to a seven-coordination Ru species at higher oxidation states and the highly efficient bimolecular (I2M) O-O bond formation assisted through π-stacking interactions between the axial ligands are considered the main reasons for this high catalytic performance.
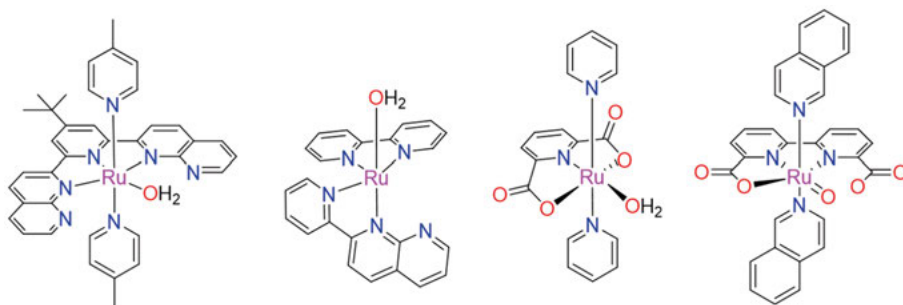
Figure 1.8. *Illustration of mono nuclear molecular complexes for water oxidation. The complexes on the left follow the WNA mechanism, while the ones to the right the I2M mechanism.*

In this particular case, the catalytic cycle begins in a similar manner to that of WNA, reaching a Ru$^{(V)}$=O species from Ru$^{(II)}$-H$_2$O through mainly PCET processes. The equilibrium between the Ru$^{(V)}$=O and Ru$^{(IV)}$=O$^{\bullet}$ species allows the dimerization of the complex, forming the corresponding peroxide intermediate Ru$^{(IV)}$-O-O-Ru$^{(IV)}$, which is highly favoured by π-stacking interactions between the axial pyridyl-based ligands. The next step is the reductive elimination of the bridging peroxide ligand to form dioxygen, which is the rate-determining step and closes the catalytic cycle.
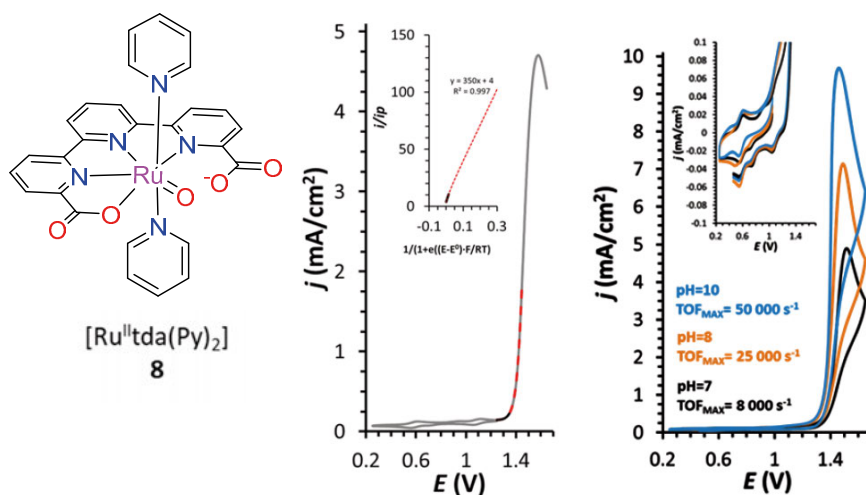
Figure 1.9. *[Ru(tda)(py)₂] with a tda²⁻ ([2,2':6',2"-terpyridine]-6,6"-dicarboxylate) ligand in its 7-coordinate state. Its catalytic performance was measured by electrochemical methods achieving the impressive TOF values of 8000 s⁻¹ and 50000 s⁻¹ at pH 7 and 10. Reprinted with permission from the American Chemical Society. R. Matheu et al / J. Am. Chem. Soc.* **2015***, 137, 33, 10786 – 10795.*

In a follow up study, Sun et al took advantage of the bda²⁻ framework and the tuned axial ligands, developing a new set of complexes.[28] Using the Ce$^{(IV)}$ as sacrificial oxidant, an increase of reaction rate (TOFs of 380 to 1000 s⁻¹) and elevated TON values (11300 to 1010000 s⁻¹) were achieved. Llobet and co-workers synthesised and tested a new ruthenium mononuclear complex based on the ligand tda²⁻ ([2,2':6',2"-terpyridine]-6,6"-dicarboxylate) shown in Figure 1.9.[29] Its catalytic performance was measured by electrochemical methods achieving the impressive TOF values of 8000 s⁻¹ and 50000 s⁻¹ at pH 7 and 10 respectively, according to the foot of the wave analysis (FOWA).[30]

This represents the best results reported for molecular water oxidation catalysis thus far. The high catalytic activity is mainly assigned to two factors: a) the easy access to high oxidation states and stabilisation of a seven-coordination environment for Ru, provided by the anionic ligand tda²⁻, and the presence of a pendant base, which acts as a proton acceptor and has a key role during the critical O-O bond formation step. In contrast with the I2M mechanism identified for Ru-bda²⁻ complexes, Ru-tda²⁻ forms to the O-O bond through the nucleophilic attack of a water molecule to a M-O species (WNA). Given that this pathway is not require diffusional encounter of the catalysts, this fact has been found particularly relevant when targeting to the generation of efficient anodes[31] and photoanodes.[32]

1.8 Other Transition Metal Complexes as Water Oxidation Catalysts

Other transition metal complexes, other than those based on ruthenium, have been reported to operate as water oxidation catalysts. Molecular Iridium complexes have gained popularity as water oxidation catalysts, with the first reported were cyclometalated phenylpyridine iridium complexes by Bernhard[33] (Figure 1.10). Subsequently, iridium-based WO catalyst containing the pentamethylcyclopentadienyl (cp*) ligand and cyclometalated N,N-bidentate ligands were developed, with the best results achieving a TOF of 0.24 s^{-1} and a TON ~320 at pH when Ce$^{(IV)}$ was used as sacrificial oxidant.

A follow-up study showed that carbene-type ligands improved the performance of the Ir complexes. This significantly improves the performance in water oxidation catalysis, obtaining TON's of ~10000 at pH~1.[34, 35] Although these complexes exhibit long-term activity, full characterisation of the active species is not straightforward due to the partial or complete oxidation of the ligands under the strong oxidising conditions,[36] or by decomposition which forms iridium oxides.[37-39]
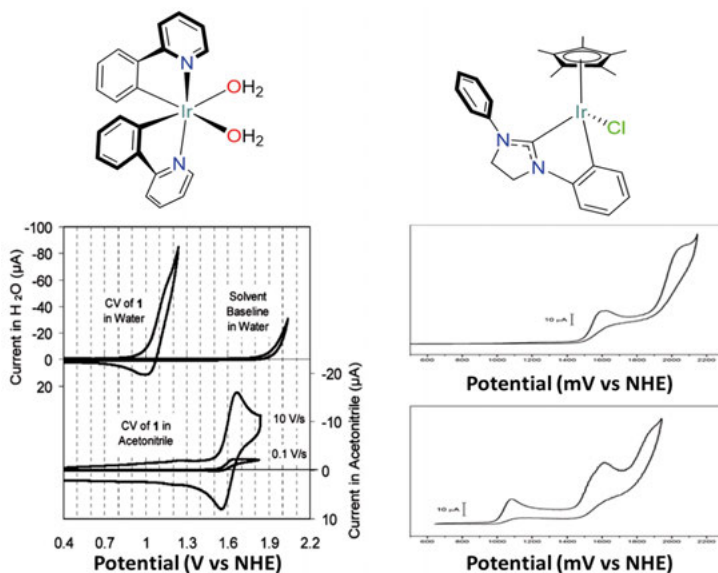
Figure 1.10. *Bernhard's Iridium-based WO catalyst containing cyclometalated N,N-bidentate and pentamethylcyclopentadienyl (cp*) ligands. Using Iridium complexes containing carbenes further improves the TOF frequency to up to 10000. Reprinted with permission from American Chemical Society. N. D. McDaniel / J. Am. Chem. Soc.* ***2008****, 130, 1, 210 - 217 and T. P. Brewster et al / Organometallics* ***2011****, 30, 5, 965 - 973.*

Cobalt based water oxidation has also evolved very fast, with Berlinguette[40] reporting the first cobalt complex being capable of electrochemically oxidising water via a PCET mechanism at neutral to basic pH. Follow up studies showed a wide variety of complexes with ligands bearing corroles,[41, 42] porphyrines,[43, 44] salen-base ligands,[45, 46] polyoxometalates[47, 48] and the bpp- ligand[49] were suitable for water oxidation applications.

The ques to develop alternative catalysts based on metals of high natural abundance, low toxicity and low-cost resulted in examples based on manganese and iron. Crabtree[50] discovered the first binuclear manganese complex capable of oxidising water into molecular oxygen. The strategy of this work was to produce oxygen, inspired by examples observed in nature, and involving the high valance di-oxo-intermediate (Figure 1.11). This paper described for the first time that di-oxo dimanganese complexes require an O-O bond forming reaction to take place before oxygen evolution is observed.
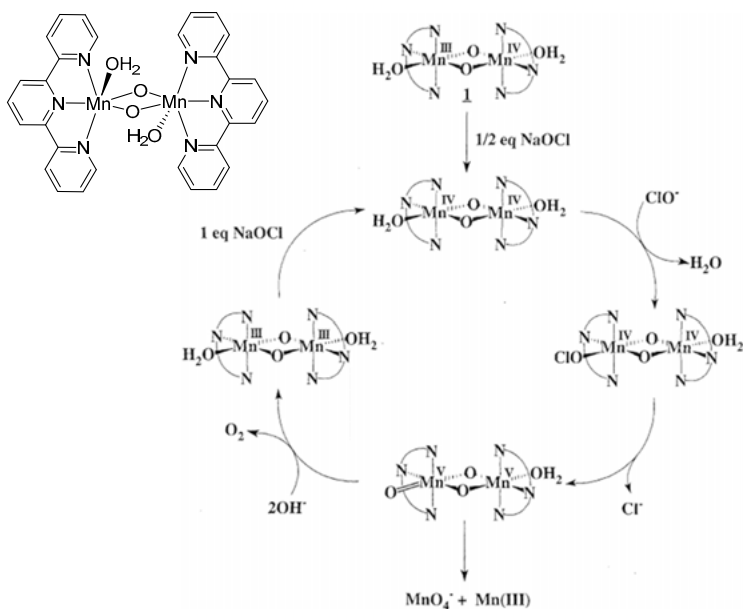
Figure 1.11. Crabtrees's discovery of the first artificial molecular manganese complex capable of oxygen evolution. Reprinted with permission from Science. J. Limburg et al / SCIENCE **1999**, 283, 5407, 1524 - 1527.

This work found the X-ray crystal structure of the precursor, and used spectroscopic and O^{18} labelling to find that the reaction mechanism involved a Mn=O intermediate, making this system a viable model for photosynthetic water oxidation. The crystal structure shows the complex as a mixed valence dimer, the two Mn units are identical to each other due to the di-inversion

centres present. The di-oxo core has dimensions that are typical of dimanganese complexes (Mn-Mn bond distance is approximately 2.7 A).

The most important feature of this complex is the presence of exchangeable aqua coordination sites on each of the Mn ions, resulting from the meridionally coordinated terpyridine ligands. The di-manganese complex is further wrapped in sheaves of hydrogen bonding water molecules that function to interlock the oxo bridges and water molecules.

Oxygen labelling experiments using $NaClO^{18}$ revealed that the first step of catalytic turnover is most likely Mn=O formation. The terminal oxo ligand can rapidly exchange with the O^{18}-labelled hydroxide or aqua on the other Mn ion of the dimer. The final step is the $O^{18}H$ that forms can rapidly exchange with the solvent to produce a complex that are both O^{18} labelled.

The Mn=O species can be thought of as either an electrophile, which is open to attack by a hydroxide species that is free or ligated to the other Mn ion, or as a radical species that has the ability to react with water molecule outside of the complex. Both pathways are valid as both can result in oxygen production the isotopic composition similar to the solvent.

Åkermark[51, 52] subsequently reported new manganese molecular complexes bearing imidazole and carboxylate groups that lower the overpotential for catalysis (Figure 1.12). This decrease in potential also allows the complexes for compatible with oxygen-free sacrificial oxidants such as $[Ru(bpy)_3]^{3+}$.

A crystal structure obtained by reflux in methanol and crystallisation at room temperature showed the loss of an acetate ion and the formation of an S2-symmetric dimer. The bond lengths of this structure exhibit a resemblance to the four manganese cations bridged by oxygen atoms in the Mn_4Ca cluster of the oxygen evolution catalyst in Photosystem II. The oxidation state of the Mn atoms was determined to be Mn^{II} and Mn^{III}, with the oxygens bridging the Mn ions being deprotonated. Light induced oxygen formation using $[Ru(byp)_2(deeb)](PF_6)_2$ as a photosensitiser gave a TON of 4.

Bernhard[53] reported the first family of molecular iron complexes that were capable of oxidising water into dioxygen with moderate TOFs > 1.3 s^{-1} with $Ce^{(IV)}$ used as a sacrificial oxidant. At the time, this was a record for transition metal complexes other than ruthenium, although catalysis only lasted for a couple of seconds. Lloret-Fillol subsequently reported a family of molecular iron catalysts containing easily accessible modular tetradentate nitrogen-based ligands, which are able to perform the oxidation of water with high efficiency.
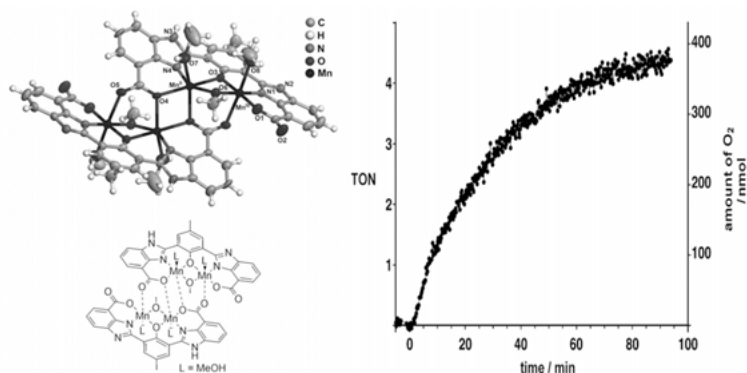
*Figure 1.12. Akermark's manganese complex capable of oxygen evolution. X-ray crystal structure of the complex shows that this complex exists as a symmetric dimer, similar to one found in photosystem II. Was subsequently tested using a photosensitizer. Reprinted with permission from Wiley publishing. E. A. Karlsson et al / Angewandte Chemie International Edition **2011**, 50 (49), 11715 - 11718.*

Labelling experiments confirmed that oxygen is the sole gaseous product, with the activity depending strongly on the concentration of both the catalyst (1–0.01 mM) and the oxidant (50–200 mM), with the highest record TON of 360 and a turnover frequency of 9.23 s^{-1} using Ce$^{(IV)}$.[54]

The very robust and neutral tetradentate pyridine triazacyclononane ligand Me$_2$Pytacn coordinates strongly through three aliphatic amines and one pyridine to the iron centre, leaving two adjacent extra coordination sites. Other prototypical nitrogen-based ligands with diverse coordination, electronic and steric properties were tested to alter the ligand rigidity and ligand basicity. This study found that similar or better water oxidation can be found in complexes that have two available coordination sites in a cis relationship relative to each other. Complexes that had the two coordination sites in trans position, or contained only one single coordination site were inactive for water oxidation.

On the basis of all the experimental evidence, it is proposed that iron complexes of general formula [Fe(X)$_2$(LN$_4$)] shares a common catalytic cycle. Spectroscopic monitoring demonstrates that the initial Fe$^{(II)}$ complexes [Fe(X)$_2$(LN$_4$)] are oxidised by Ce$^{(IV)}$ to yield the water–oxo compound [Fe$^{(IV)}$(O)(H$_2$O)(LN$_4$)]$^{2+}$, LN$_4$Fe$^{(IV)}$OH$_2$, which is the resting state of the complex (Figure 1.13). The RDS involves further oxidation of the oxo-Fe$^{(IV)}$ complex by Ce$^{(IV)}$, to form a highly oxidizing [Fe$^{(V)}$(O)(OH$_2$)(LN$_4$)]$^{3+}$ intermediate.
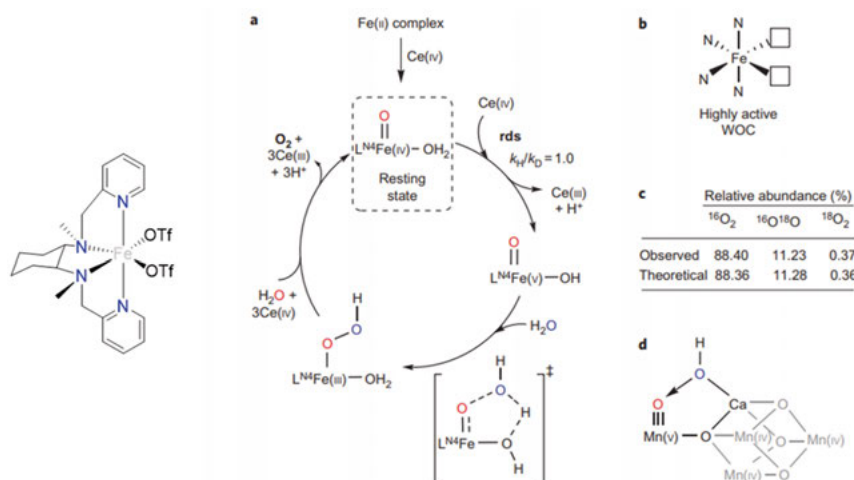
Figure 1.13. *Barnhard's Iron complex for molecular water oxidation and mechanism. Reprinted with permission from Nature. J. L. Fillol et al / Nature Chemistry* **2011**, *3 (10), 807 – 813.*

Given the high oxidation state of the metal centre, the water ligand must be very acidic and the $[Fe^{(V)}(O)(OH)(LN_4)]^{2+}$ intermediate $LN_4Fe^{(V)}OH$ is expected to be formed. Subsequent attack of a water molecule, assisted by a hydrogen-bond interaction with the hydroxide ligand, forms the O–O bond, which reduces the iron$^{(V)}$ to $[Fe^{(III)}(OOH)(H_2O)(LN_4)]^{2+}$ intermediate $LN_4Fe^{(III)}$–OOH.

The catalytic cycle can be closed, following two possible pathways. The first possibility comprises further oxidation of intermediate $LN_4Fe^{(III)}$–OOH to give $LN_4Fe^{(IV)}$–OOH or $LN_4Fe^{(V)}$–OOH, and O_2 extrusion via reduction of the metal centre to $Fe^{(II)}$ or $Fe^{(III)}$. This mechanism finds precedent in the water oxidation at mononuclear ruthenium complexes.[27] The second possibility involves protonation of the hydroperoxide ligand in $LN_4Fe^{(III)}$–OOH extruding H_2O_2 and forming a $Fe^{(III)}$ species that is oxidized rapidly by $Ce^{(IV)}$, and thus closes the catalytic cycle. The nature of these molecular iron catalysts and their active species is still under investigation.[55]

1.9 Anchoring Molecular Species via Non-Covalent Interactions

Molecular transition metal are excellent candidates for catalytic oxidation due to their rapid oxygen evolution rates relative to many solid-state devices, as well as due to their highly tuneable structures. For their adoption in large-scale devices, heterogenisation of molecular species is required. These anchored

catalysts must run at a higher current density of at least 10 mA/cm^{-2}, the anchorage must be stable under oxidative conditions, the O-O bond formation step may preferably occur via a water nucleophilic attack (WNA) mechanism, owing to the restricted diffusion.[56-58]
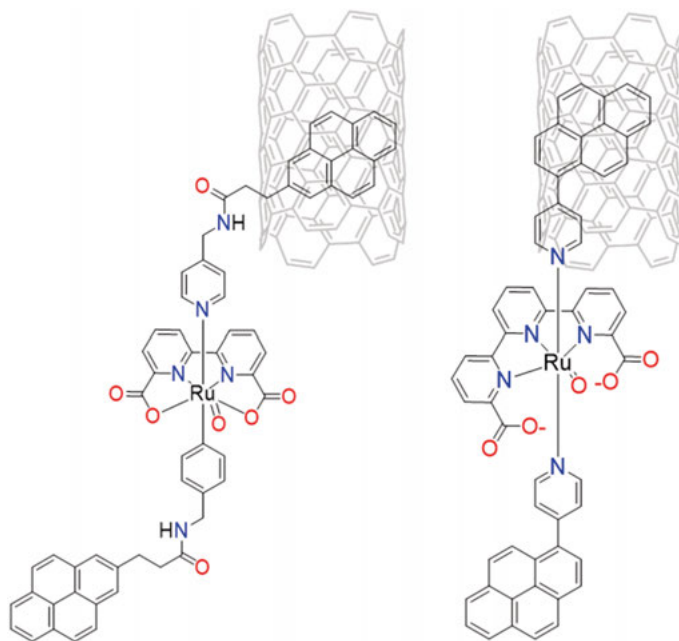
Figure 1.14. *π-π stacking of Ru-bda and Ru-tda pyrene derivatives on the surface of multi-wall carbon nanotubes.*

A couple of examples of π-stacking anchorage on the surface of multi-wall carbon nanotubes is reported by Sun and Llobet, who independently reported complexes that have their axial ligands modified with pyrene moieties (Figure 1.14.).[59, 60] A variation of this methodology is molecular coordination oligomers that can be adsorbed onto graphitic surfaces such as multiwalled carbon nanotubes (MWCNT) through aromatic catalyst–surface CH–π interactions.[61, 62]

1.10 Covalent Surface Immobilisation of Molecular Complexes for Water Oxidation

There are numerous methods to covalent anchor molecular catalysts to different substrates. One of the most popular approaches is the use of anchoring groups at the molecular complex for its attachment to metal oxides. This anchoring group must be hydrolytically stable, resistant to oxidation and stable under different pH conditions.
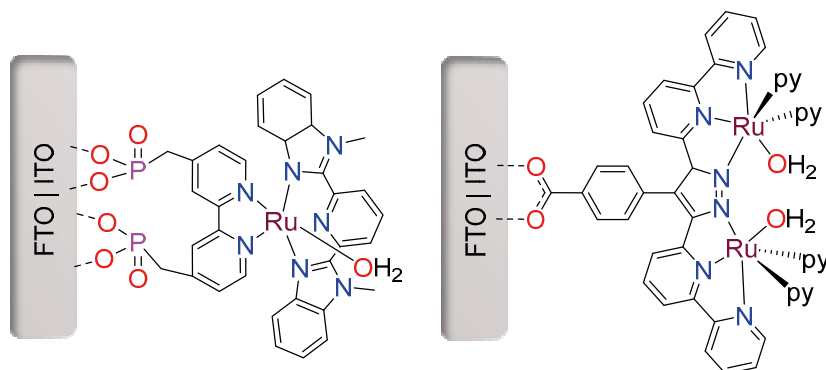
Figure 1.15. *Attachment of molecular complexes to metal oxides via the use of anchoring groups on the molecular complex. Two examples using phosphonates and carboxylates as the anchoring group on the complex.*

There are four classes of commonly used anchoring groups, which are carboxylates, phosphonates, silatranes and hydroxamic acids.[63] This strategy has been used for mono and dinuclear water oxidation catalysts, with carboxylates and phosphonates having been most popular for anchorage on the surface of $FTO|TiO_2$[64, 65] (Figure 1.15).

Another strategy that has been employed to covalently anchor the catalyst is based on electrografting. Which permits binding of an organic layer to a conducting substrate. Oxidative electrografting is one form of covalent bonding, where a substrate is exposed to an oxidative potential which initiates a radical chain reaction that results in electropolymerisation.[66] Such an example of this process is the oxidative electropolymerisation of a Ru-tda complex with a thiophene substituent on the surface of glassy carbon or carbon paper to afford surface-immobilised catalyst material. Upon activation of this electrode, the electrode proved to be a powerful molecular anode for water oxidation, with high Faradaic efficiencies and stability.[67]

This strategy of anchorage is also applicable to reductive electro grafting of diazonium salts. For example, this strategy was utilised for the [Ru(bda)(4-pyridin-4-yl)$_2$] complex (Figure 1.16). Treatment of this di-analine complex with nitric oxide converts the amino groups to the highly reactive diazonium salt, which upon exposure to reductive potentials results in the covalently anchored catalyst.[56]
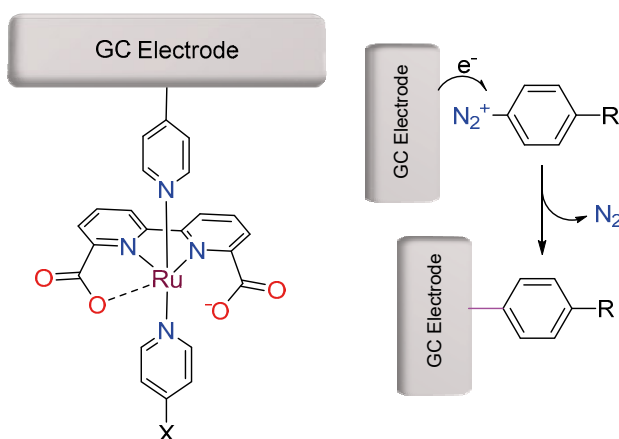
Figure 1.16. *Scheme for diazonium grafting of [Ru(bda)(4-pyridin-4-yl)$_2$] on the surface of glassy carbon.*

Another alternative mechanism is the use of pyrazine linkage, which relies on a condensation reaction of o-phenylenediamine derivatives to form graphite-conjugation catalysts (GCCs) which exhibit strong electronic coupling to the electrode, leading to electron transfer (ET) behaviour that diverges fundamentally from that of solution-phase or surface-tethered analogues. The complex [Ru(dmbpy)$_2$(phenda)]Cl$_2$, was anchored in this manner (Figure 1.17).[68]
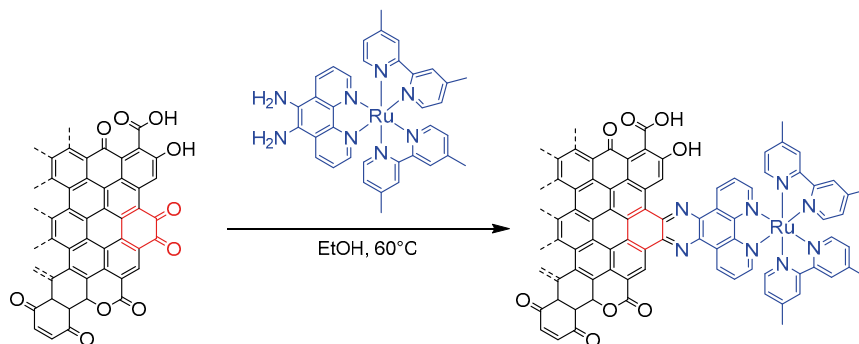
Figure 1.17. *An example of pyrazine linkage of the ruthenium molecular water oxidation complex [Ru(dmbpy)$_2$(phenda)]Cl$_2$.*

1.11 Metal Organic Frameworks (MOFs)

Metal organic frameworks (MOFs) are a class of porous crystalline materials made from polydentate organic linkers and inorganic metal nodes (secondary-binding units, SBUs).[69, 70] MOFs are usually crystalline and porous, but this is not always a strict requirement for such materials.[70] Many MOFs can contain pores of various sizes, which can range from meso or nanopores with high internal surface areas. At the same time owing to the modularity of the linkers and SBUs, a seemingly infinite numbers of possible structures can be obtained, with UiO-type MOFs (UiO = Universitetet i Oslo)[71] and NU-1000 (North-Western University)[72] being a couple of well-known examples. Once synthesised, MOFs also be further functionalised through post-synthetic modifications (PSM):

1) Organic linkers which can be functionalised using many typical organic chemistry transformations.

2) Post-synthetic exchange (PSE) of linkers of similar size of a parent MOF.

3) Post-synthetic insertion (PSI) of a linker into a vacant pocket that is already present in a parent MOF structure.

The use of MOFs presents multiple opportunities that could be favourable in water oxidation applications, such as the permanent porosity that facilitates fast substrate diffusion, as well as site isolation that inhibits bimolecular decomposition pathways of incorporated molecular catalysts. MOFs also provide an exceptionally high surface areas with potential catalyst loadings that are orders of magnitude higher than those of corresponding monolayers on electrode surfaces. However, MOFs have only been used on a limited number of occasions as their linkers and metal clusters are often non-conducting, leading to poor charge transport to the MOF-embedded catalysts. As a consequence, realisation of effective electrocatalytic MOFs have remained challenging. MOFs that exhibit electroactive behaviour or high conductivities typically are constructed from specialised linkers that promote conduction through the framework.

As already insinuated, each individual linker that the MOF is composed of can have one or more functions. It can be catalyst, carry specific functionalities to tune the pore environment and facilitate charge transport throughout the framework. So far, several research groups focused their efforts on the development of polyoxometalates (POMs) as catalysts for water oxidation by Bonchio[73] and Hill[74] (Figure 1.18). These systems provide a robust all-

inorganic framework environment coordinating the metal core, which makes them promising for applications in WO.
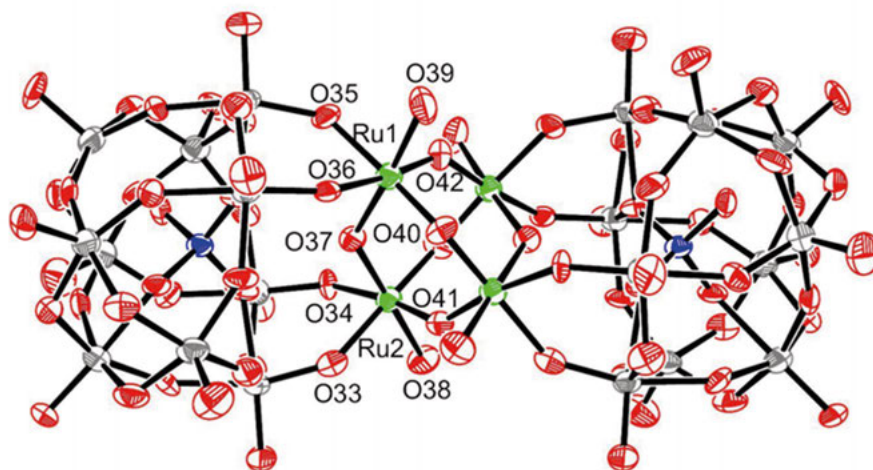
Figure 1.18. *Structure of the polyoxometalate (POM), integrated with a ruthenium core for water oxidation applications. Reprinted with permission from American Chemical Society. Y. V. Geletil et al / J. Am. Chem. Soc. **2008**, 130 (15), 5006 - 5007.*

2 Charge Transport in Porous Frameworks

2.1 Fickian Diffusion in Metal Organic Frameworks (MOFs)

In the case of porous frameworks, substrates need to be able to diffuse inside the porous structures to engage in catalytic reactions, which create situations where the overall reactivity is limited by mass transport. In the case of redox catalysis as the case in water oxidation, the transport of charge may too constitute an additional limitation. This is an important fact to bear in mind, as the materials that are discussed in this thesis are micro or mesoporous in nature.

The fundamentals of this phenomenon were first demonstrated by Alfred Fick in 1855.[75, 76] Mass transport of a free species is considered, but we can extend this concept to diffusion of charge as it propagates through heterogeneous materials by a hopping mechanism between redox active, but immobilised discrete molecular units. When a species is introduced into a solution, a concentration gradient is established, which creates a driving force for the diffusion to occur. This describes Fick's first law where molar flux F_i (mol cm^{-2} s^{-1}) for a species i is given by:

$$F_i = -D_i \nabla C_i \qquad \text{Eq 5.}$$

Where D_i is the diffusion coefficient (cm^{-2} s^{-1}), and ∇C_i is the divergence or gradient of the concentration of species i. Applying the conservation equation, also known as the diffusion equation:

$$\frac{\partial c_i}{\partial t} = -\nabla \cdot F_i \qquad \text{Eq 6.}$$

We then arrive at Fick's second law, also known as the diffusion equation:

$$\frac{\partial c_i}{\partial t} = D_i \nabla^2 C_i \qquad \text{Eq 7.}$$

For the majority of electrochemical methods, diffusion can be described as one-dimensional normal to the electrode surface. Parallel chemical reactions must be modified by the kinetic term K_i, which accounts for the rate of consumption or production of each species i:

$$\frac{\partial C_i}{\partial t} = D_i \nabla^2 C_i + K_i \qquad \textbf{Eq 8.}$$

This chemical consumption/production rate is written as a chemical reaction rate law. The equation on the right-hand side gives the rate of change in concentration as a result of diffusive spreading, with the second term accounting for the rate of change in concentration resulting from chemical reactions. If a species X is diffusing and reacting according to the chemical reaction X + Y → Z, with a second order rate constant κ, the overall diffusion equation can be expressed as:

$$\frac{\partial C_X}{\partial t} = \left(\frac{\partial C_X}{\partial t}\right)_{diff} + \left(\frac{\partial C_X}{\partial t}\right)_{rxn} = D_X \nabla^2 C_X + K_X \qquad \textbf{Eq.9.}$$

$$\left(\frac{\partial C_X}{\partial t}\right)_{diff} = D_X \nabla^2 C_X \qquad \textbf{Eq 10.}$$

$$\left(\frac{\partial C_X}{\partial t}\right)_{rxn} = K_X = -k C_X^a C_Y^b \qquad \textbf{Eq 11.}$$

Where *a* and *b* are reaction orders for X and Y. All that was required for the above analysis was a chemical reaction rate law combined with the application of conservation of mass to Fick's first law. The physico-mathematical description of any reaction-diffusion problem will be composed of a system of second order partial differential equations, with one for each species involved in the reaction. This system of equations must be solved simultaneously, considering the appropriate and initial boundary conditions for a particular geometry and experimental set up.

These interfacial interactions are ubiquitous in catalysis research as they are of particular consequence when molecular catalysts are heterogenised onto a solid support. One consequence that arises when going from a homogeneous phase to a heterogeneous surface or film is that consideration needs to be made for the necessary transport of both charge and substrates to the catalytic sites. The concentration of substrate and catalytic intermediates of interfacial reactions will be a function of at least one spatial coordinate in addition to time.

2.2 Charge Transport in MOFs

As previously mentioned, MOF materials are highly tuneable and modular. As individual building blocks are molecular in nature, each unit can potentially host a redox-active catalyst,[77-80] which alters the properties of the material at hand, and facilitates charge transport through the MOF by an electron hopping mechanism.[81-85]

When creating electroactive MOFs, two general strategies are applicable. The first such strategy involve through-bond approaches in which a continuous path for electron transfer is needed. This can be achieved in two main ways, either through specifically designed molecular orbital overlap of the electroactive MOF components or coordination of conducting bridging guest molecules (Figure 2.1. A). Alternatively, through-space approaches which can be attained through π-π stacking of electroactive linkers (Figure 2.1. B) or electron hopping mechanisms between discrete redox-active centres in the MOF scaffold (Figure 2.1. C). Many electroactive MOFs take advantage of the latter electron hopping design, which is synthetically the most straightforward approach to accomplish with the selection of appropriate redox-active linker components.
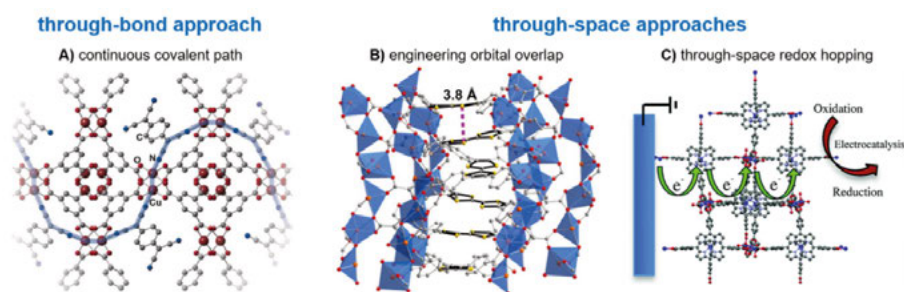
Figure 2.1. *Schematic representation of (A) through-bond and (B & C) through-space approaches to improving conductivity in MOFs. Reprinted with permission from The Royal Society of Chemistry. B.D. McCarthy et al. / Coordination Chemistry Reviews.* **2020**, *406, 213137.*

Charge transport via redox hopping is best described as a series of electron self-exchange events between adjacent redox-active centres paired with the diffusion of counter ions through the framework to maintain charge neutrality.[86-88] As the redox-active centre is spaced periodically throughout a MOF architecture, each electron hopping step will occur over an associated time step. Also, as a MOF is periodic, the electron can hop to any of its nearest neighbours such as a linker or SBU. These electron hopping steps do not proceed in a pre-determined path, but are random steps that can be classified as diffusive charge transport.[86, 89, 90]

This understanding of diffusion of charges in self-exchange reactions was first described by Dahms[91] and Ruff[92-94], who developed the first proposed expressions for the rate of charge transport by diffusional charge translation between molecular units in aqueous and organic solutions. This was further interpreted by Buttry[95], Savéant[96] and Bard[97, 98] when evaluating charge transport in redox-active polymers in which the redox-active units are anchored in space, which is analogous to the situation in MOFs. [86, 89, 99]

When MOFs are constructed from redox-active linkers, the electroactive components should have defined positions in the MOF structure, so that the electron hopping distances can be approximated. Similar to charge transport studies on redox polymers described in literature, charge transport of MOFs is also most easily assessed when the material is immobilised at an electrode surface.

Charge hopping through MOF films involves forward self-exchange of electrons at redox active centres from the electrode surface throughout the film, and corresponding diffusion of counter ions into the film from the solution-film interface, in order to maintain charge neutrality.[88, 89, 99]

The overall observed charge mobility can be described as a diffusive process that follows Fick's Law. As such, the global rate of diffusive charge transport via electron hopping can be simply related to an associated diffusion coefficient D_e.[88, 90, 100]

$$D_e = \frac{k_e}{6} C^o \delta^2 \qquad \textbf{Eq 12.}$$

Where k_e is the electron self-exchange rate constant, C^o is the concentration of the electroactive species, and δ is the distance between redox-active sites. The electron hopping behaviour exhibited in redox polymer films, as well as redox-active MOFs, then is quite similar to that of a freely-diffusing species in solution, in where charged molecules move away from the electrode. The changes in concentration of the electrochemically reduced unit throughout the film thus establishes a gradient that mimics that of a freely diffusing species (for example, from the electrode surface through the film) that obeys Fick's laws of diffusion.[101]

Counterions in MOF frameworks maintain electroneutrality and stabilise the reduced/oxidised linker sites within the MOF architecture; their absence halts electron hopping, causing the majority of redox-active linkers to become inaccessible.[85, 102, 103] Diffusion of ions from the solution-film interface provides the counterions necessary for the pore spaces of the MOF to maintain charge neutrality and to facilitate charge propagation.

Ion pairing[103, 104], rate of ion transport[103], and ion concentration[102] also affect charge hopping, as characterised by the diffusion coefficient D_e. The above equation only describes both charge and mass transport phenomena, which are strictly diffusional in nature and ignore other molecular interactions, such as ion-pairing, linker-linker interactions or field effects.[100, 105, 106] This idealised situation is highly unlikely under experimental conditions, and as a result, a more detailed picture must be considered for evaluating diffusion-like charge transport which considers these additional external factors.

One of the many reasons for understanding electroactive MOFs is to be able to utilise effective MOF materials for electrocatalysis. The necessity of both mass and charge transport requires counter ions in an electroactive film. In the case of electrocatalysis, the additional electrochemical reaction increases the level of complexity in the system. The added mass transport associated with the electrocatalytic reaction then introduces reaction-diffusion to the MOF system, along with the charge transport and counter ion transport considerations already present.[101, 107]

Transport processes considered for MOF-based electrocatalysts are more complex than the overall mass transport observed in solely redox-active MOF systems. This additional complexity makes it difficult to deduce kinetic information from catalytic reactions occurring within MOF materials. These three transport phenomena (charge transport originating from the electrode throughout the framework, substrate/ion diffusion originating from the film/solution interface, and reaction-diffusion within the MOF)[101, 107, 108] must all then be considered for any models in which accurate kinetic information is to be derived for MOF-based electrocatalysts.

A reaction-diffusion layer, δ_{rxn}, can be identified and is representative of the catalytically active portion of a MOF film (see Figure 2.2.). For example, in case electron hopping is slow throughout the film, the diffraction diffusion layer is close to the electrode/MOF interface. It can be assumed that the catalyst must be activated via charge transport from the electrode and substrate molecules must be able to diffuse into the reaction-diffusion layer via mass transport from the solution-film interface. Therefore, additional parameters must be accounted for when examining electrocatalytic MOF films.

Film thickness d_f must be considered, as the thickness of the film will determine whether the reaction-diffusion layer will occupy the entire film or will occupy a localised fraction of the film. In the case of thin films, sufficient charges may be supplied by electron hopping transport from the electrode and sufficient substrate provided by mass transport into the MOF film to drive the electrocatalytic reaction at all catalytic sites in the film. For MOF-based electrocatalytic materials, rational design to control physical material parameters, like film thickness, is required to access as many of the incorporated catalysts sites as possible in order to prepare the most efficient MOFs.

The rate of charge transport in electrocatalytic MOF materials , impact on whether reaction-diffusion layers will be present in a catalytic MOF. Whether electron hopping charge transport is confined to the thickness of the MOF film, or limited by the physical restriction of the film thickness can be examined using cyclic voltammetry by varying the scan rate (v).[86, 89, 101, 107, 109] In short, fast scan rates give rise to diffusional electro hopping charge transport

within the film without being restricted by the film boundary. Extending the experiment by applying slower scan rates, electron diffusion is extended into the film, ultimately reaching the film boundary. These two scenarios are termed as either semi-infinite or finite regimes.
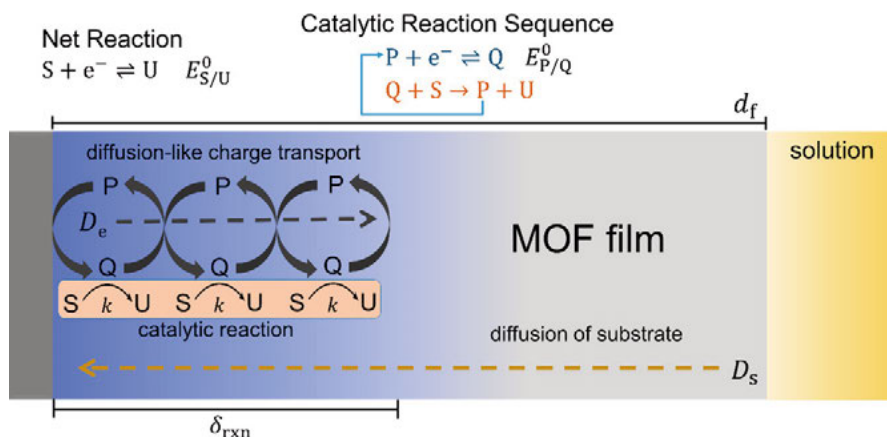
Figure 2.2. *One-electrode, one-step catalytic mechanism occurring in a molecular heterogenised MOF film electrode, where P and Q are the oxidised and reduced form of the catalyst linker, S is the substrate, κ is the second order rate constant for the catalytic reaction ($k_{cat} = k_S^\circ$), D_e is the charge transport diffusion coefficient, and the D_S is the intra-MOF substrate diffusion coefficient. Reprinted with permission from the Journal of American Chemical Society. B.A. Johnson et al. / J. Am. Chem. Soc. **2020**, 142, 28, 11941 – 11956.*

2.3 Characterisation and Analysis

Characterisation of ruthenium molecular complexes and metal-organic frameworks described in this work are carried out using a variety of methods. In the cases of molecular complexes, ^{1}H & ^{13}C nuclear magnetic resonance (NMR), electron paramagnetic resonance (EPR) LC-MS, HR-MS and MALDI-TOF, X-ray crystallography and elemental analysis were used. For MOF characterisations, physical material characterisation using powder X-ray diffraction (PXRD) was used to ascertain the crystallinity of samples. Brunauer-Emmett-Teller (BET) isotherms is used to measure both the specific surface area and porosity, and scanning electron microscopy (SEM) can be used to visually verify MOF morphology. FT-IR, SEM-EDX (energy dispersive x-ray), and elemental analysis (ICP-OES) are used to determine chemical composition of the MOFs made in this thesis.

The molecular catalysts were integrated into MOF structures via direct synthesis, co-synthesis and via post-synthetic exchange. Analysis of these MOFs

by ICP-OES, SEM/EDX and XPS are useful methods to confirm linker incorporation and are valuable in the quantification of the amount of linker incorporated.

2.4 Electrochemical Analysis

For greater understanding of electron transfer processes in electroactive MOFs and heterogeneous ruthenium coordination oligomers, analysis by cyclic voltammetry (CV), differential pulse voltammetry (DPV) and chronoamperometry were used. These techniques allow for the evaluation of mass and charge transport in catalytic materials.

In the majority of cyclic voltammetry experiments, a three-electrode set-up is employed using a working electrode (WE), counter electrode (CE) and reference electrode (RE).[110, 111] A known potential is then applied to the working electrode and swept linearly towards a second known potential. The potential is reversed and this process continues until the cycle is terminated. The current (i) passed through the working electrode is measured during this potential sweep, and plotted against the applied potential (E), to give rise to a cyclic voltammogram (CV).

The waves observed in the CV correspond to the reduction (potential scanned cathodically) or oxidation (potential scanned anodically) of the analyte at the electrode surface. Generally, a simple one-electron process is characterised by fast interfacial electron transfer. If the redox-active molecule, A, and its corresponding product B, according to:

$$A + e^- \rightleftharpoons B$$
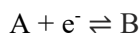
Are stable over the course of the experiment, the charge that is passed through the cell in the forward direction is the same as what is collected on the reverse. If A and B are immobilised on the surface, the charge is proportionatal to the surface concentration of the analyte, the charge is proportional to the surface concentration of the analyte. In other words, the amount of redox active analyte, in our case often a catalyst, can be determined by integrating the current of a wave in a CV.

$$\Gamma_A + \Gamma_B = \Gamma^o \qquad \textbf{Eq 13.}$$

$$E = E^o + \frac{RT}{F}\ln\left(\frac{\Gamma_A}{\Gamma_B}\right) \; or \; \Gamma_A = \Gamma_B \exp\left[\frac{F}{RT}(E - E^o)\right] \qquad \textbf{Eq 14.}$$

F = Faraday constant, T = absolute temperature, R = Ideal gas constant, E = electrode potential and E^s = standard potential of the A/B redox couple.

Therefore:

$$\Gamma_A = \frac{\Gamma_o}{1+\exp\left[-\frac{F}{RT}(E-E^o)\right]}, \qquad \Gamma_B = \frac{\Gamma_o}{1+\exp\left[\frac{F}{RT}(E-E^o)\right]} \qquad \text{Eq 15.}$$

The current, i, is simply obtained from the time (t) derivatives of these functions according to:

$$\frac{i}{FS} = -\frac{d\Gamma_A}{dt} = \frac{d\Gamma_B}{dt} \qquad \text{Eq 16.}$$

$$i = FS\Gamma^o \frac{Fv}{RT} \frac{\exp\left[\frac{F}{RT}(E-E^o)\right]}{1+\exp\left[\frac{F}{RT}(E-E^o)\right]} \qquad \text{Eq 17.}$$

Where v is the scan rate and S is the electrode surface area. The current varies with time and potential, which is shown in the above equation. In the case of redox-active, electrocatalytic MOFs and coordination oligomers, the analyte is generally a surface-immobilised material, therefore the concentration of electrochemically accessible material is constant over the course of a forward and reverse sweep in a CV experiment. The shape of the measured current response can be used to determine the chemical reversibility of redox-addressable MOF-immobilised species.

If the current response in the return sweep is different to that in the forward scan, the redox event in question may be reversible. Alternatively, scenarios involving additional mass or charge transport limitations that are outside the purview of single electron oxidation and reduction processes, may contribute to such behaviour.[112]

The quantities of species A & B at the surface are functions of the electrode potential. The previous derivation was made under the assumption that both species A & B are at equilibrium on the surface when the standard potential (E^o) of the redox process is applied. Assuming chemical reversibility, the redox event at equilibrium must obey the Nernst equation (eq 18):[110, 111]

$$E = E^o + \frac{RT}{F}\ln\left(\frac{[A]}{[B]}\right) \qquad \text{Eq 18.}$$

Where E is the applied electrochemical potential, R is the universal gas constant, T is the temperature, F is the Faraday constant and [A], [B] are the concentrations of the oxidised and reduced species respectively. The peak-to-peak separation of an electrochemically reversible redox pair should be

approximately ~57 mV at 25°C.[111, 113] For surface-immobilised species, no peak-to-peak separation should in principle be observed as the analyte can't physically diffuse from or towards the electrode surface.

In the case of porous materials such as MOFs, electron hopping can occur between electroactive sites in a diffusive manner. If this electron diffusion is slower than the timescale of the CV experiment, a "diffusional" wave can be expected. Conversely, if electron transport through the MOF is faster than the CV timescale, the finite diffusion regime is reached, and no peak-to-peak separation should be observed. [78, 114, 115]

This provides information on the total concentration of the electroactive linkers (C_P^o). Integration of the current in the CV at slow scan rates or measuring charge passed after total reduction or oxidation of the film will provide the electroactive surface concentration (Γ_P^o).

The thickness of the film (d_f) is sourced from independent measurement, where C_P^o can be calculated using $\Gamma_P^o = d_f C_P^o$. Total surface concentration is usually calculated via destructive methods such as inductively coupled plasma. CV will yield D_e under conditions where $\lambda_e > 1$. Plotting i_p vs $\sqrt{v}$ will give a straight line with a slope proportional to $\sqrt{D_e}$.

2.5 Differential Pulse Voltammetry

Differential Pulse Voltammetry (DPV) is a technique that involves applying amplitude potential pulses on a linear ramp potential. In DPV, a base potential is initially applied at the electrode so that there is no faradaic reaction, and then increased between pulses with equal increments.

The current is immediately measured before the pulse application and at the end of the pulse, and the difference between them is recorded, which reflects the pulse shape in DPV.[116] In DPV, the peak potential, E_p, can be approximately identified with $E_{1/2}$. With the irreversibility, E_p deviates from $E_{1/2}$ as the base of the peak widens and its height decreases.

The DPV graph is representative between applied potentials and measured currents, with species absorbed on the electrode being the easiest to observe.[116] While CV provides essential information such as reversibility and types of redox processes. DPV can be used for quantitative determinations due to its sensitivity and minimisation of capacitive current, such as detection of the concentration of a species at the electrode interface.[117]

2.6 Measuring Diffusion via Chronoamperometry

Chronoamperometry is a controlled potential experiment, where a known potential is applied to the working electrode and held at a constant potential for a set period of time. Over the course of the experiment, the current (i) is recorded as a function of time. These applied potentials can be chosen from an initial CV scan of a film before controlled potential experiments to focus on particular redox couples.

Potential step chronoamperometry under conditions where semi-infinite conditions hold in the film will give access to D_e by plotting i vs $t^{-1/2}$. In systems controlled by diffusion, the current response decays until no further change in current is observed, which indicates complete reduction/oxidation of all analyte species accessible in the diffusion layer near the electrode. This time-dependent current response can be related to the diffusion of the analyte by the Cottrell equation.

$$i(t) = \frac{nFS_A C_O^o \sqrt{D}}{\sqrt{\pi t}} \qquad \textbf{Eq 19.}$$

Where n is the number of electrons transferred, F = Faraday constant, S_A = surface area of the electrode, C_O^o = initial concentration of the analyte and D = diffusivity of the analyte. Charge transport in heterogeneous material in the semi-infinite regime is diffusive, which has been demonstrated for electroactive MOF materials.[77, 78, 80, 81, 85, 115, 118, 119] The Cottrell analysis is used to extract diffusion coefficients related to diffusive electron hopping (D_e) in the material.[101]

2.7 Foot of the Wave Analysis (FOWA)

Benchmarking of molecular catalysts were carried out using foot-of-the-wave (FOWA) analysis. Catalysts are experimentally studied, with the turn-over frequency (TOF) plotted as a function of overpotential (η). This TOF is a derivative of turn-over number (TON), where the catalyst is stable over time.[120] FOWA tends to be restricted to molecular systems which have a defined standard potential, rather than electrocatalytic reactions that are not clearly identified, such as solid state electrocatalysis.

The reaction scheme represented in equations 20 and 21, a reversible couple, P/Q. This P/Q couple is incorporated into equations 22 and 23, and are characterised by a standard potential E^o, E_{H_2O/O_2} represents the difference between the standard potential and the applied potential, η represents the overpotential, where i represents the current, Q_{Ru} represents the average charge of

the redox couple to transform the substrate P to Q and regenerate the catalyst, F represents the Faraday constant, R is the ideal gas constant and T represents the temperature.

$$het P \rightarrow het Q + e^- \qquad \textbf{Eq 20.}$$

$$het Q + H_2O \rightarrow het P + O_2 \qquad \textbf{Eq 21.}$$
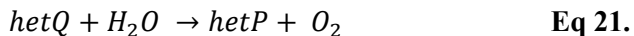
$$\frac{i}{Q_{Ru}} = \frac{k_{wna}}{1 + e^{\frac{F(E^O - E)}{RT}}} \qquad \textbf{Eq 22.}$$

Catalytic Tafel plots are used to benchmark and compare molecular water oxidation catalysts, which relates the TOF of the catalyst and the applied potential, with respect to the standard potential of the reaction.[120, 121] The catalytic Tafel plots were drawn using the equation outlined in equation 23, by plotting TOF as a function of overpotential (η) following, the rules for the hetero-WNA mechanisms[30]. Each Tafel plot reflects the distinctive features of the catalyst, which is the TOF_{max}. This apparent rate is shown in equation 24, which is where the curve reaches the plateau. The lowest value of potential where TOF = TOF_{max}, which demonstrates the relationship between TOF and overpotential, while providing a comprehensive evaluation of the performance of the catalyst as a function of overpotential.

$$TOF = \frac{k_{wna}}{1 + e^{\frac{F\left(E^O - E_{\frac{H2O}{O2}} - \eta\right)}{RT}}} \qquad \textbf{Eq 23.}$$

$$TOF_{max} = k_{wna} \qquad \textbf{Eq 24.}$$

3 Synthetic Strategies to Incorporate Ru-Terpyridyl Water Oxidation Catalysts into MOFs: Direct Synthesis vs. Post-Synthetic Approach (Paper I)

In chapters 3 and 4, we discuss strategies for the synthesis and incorporation of molecular ruthenium water oxidation complexes into UiO (Universitetet i Oslo) and NU-1000 (North-western University) MOFs. Three types of synthetic methodologies are explored, including direct incorporation during MOF synthesis with the Ru complex, either being the only linker or accompanied by a co-liker or incorporation by post-synthetic techniques. Structural and functional characterisation of the molecular catalysts and the frameworks are described. Two ruthenium complexes of the formula $[Ru^{II}(tda)(Py(PhCOOH)_2)_2]$ (tda = 2,2':6',2''-terpyridine-6,6''-dicarboxylic acid; $(PhCOOH)_2$ = 4,4'-(pyridine-3,5-diyl)dibenzoic acid) and $[Ru^{II}(tda)(PhCO_2H)_2]$ (tda = 2,2':6',2''-terpyridine-6,6''-dicarboxylic acid; $(PyCO_2H)_2$ = isonicotinic acid) were used in this chapter.

3.1 Introduction

In the context of the global energy and ecological challenges, artificial photosynthesis has caught the attention of both the scientific community and policy makers as a possible means of alternative energy storage.[7] Artificial photosynthetic devices involve water splitting by combining two half-reactions, water oxidation at the anode (Eq 1) to produce molecular oxygen and the corresponding reduction to produce hydrogen at the cathode (Eq 2).[122]

$$2H_2O \rightarrow O_2 + 4H^+ + 4e^- \qquad \textbf{Eq 1.}$$

$$4H^+ + 4e^- \rightarrow 2H_2 \qquad \textbf{Eq 2.}$$

Materials with high internal surface area that can potentially hold a large number of active sites per geometric surface area are desirable scaffolds for catalyst incorporation in applications relating to artificial photosynthesis.[123-125] Heterogenisation of molecular catalysts is required for integration into devices

for large-scale energy utilisation. MOFs provide a potential architecture for incorporation of molecular complexes for water splitting.[125] In recent years, many studies that apply this concept specifically to molecular water oxidation catalysts (WOCs) have been reported.[77, 79, 114, 118, 126-136]

Despite of these works, attempts to incorporate one of the most active Ru-based WOC to-date, [Ru^{II}(tda)(py)$_2$] (tda = 2,2':6',2''-terpyridine-6,6''-dicarboxylic acid, py = pyridine), into a MOF had been reported prior to this work. Related Ru-polypyridyl complexes incorporated into MOFs had been described though, two of which are also WOCs (Figure 3.1.).[126]

With the exception of one case where the Ru complex was post-synthetically grafted onto MOF linkers with appended pyridine groups,[114] most of these studies make use of carboxylate anchoring groups to attach the complex directly to the secondary building units (SBUs) of the target MOF. Such a strategy makes the complex an integral part of the framework without occupying the void of the MOF that provides for ion, substrate and product transport.
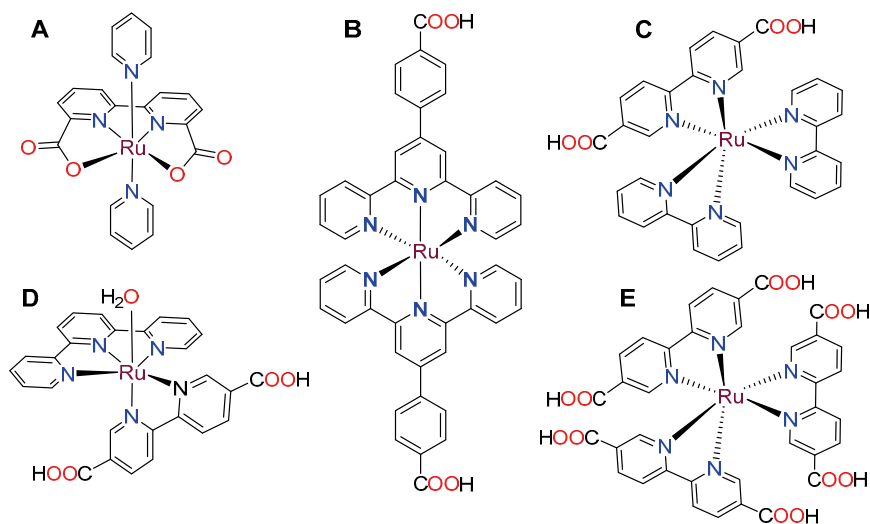
Figure 3.1. Ru-Polypyridyl complexes previously incorporated into MOFs. (A) Water oxidation catalyst Ru(bda)(Py)$_2$;[126] (B) photosensitizer Ru(cptpy)$_2$$^{2+}$, cptpy is 4'-(4-carboxyphenyl)-terpyridine;[137] (C) photosensitizer Ru(bpy)$_2$(dcbpy)$^{2+}$, bpy is 2,2'-bipyridine, dcbpy is 5,5'-dicarboxy-2,2'-bipyridine;[138-141] (D) water oxidation catalyst Ru(tpy)(dcbpy) (OH$_2$)$^{2+}$;[114, 118, 128] (E) Ru(dcbpy)$_3$$^{2+}$ as a chemiluminophore.[142]

3.2 The [Ru^{II}(tda)(py)$_2$] Catalyst and Linker Derivatives

Transition metal complexes provide an excellent platform for mechanistic studies based on a variety of spectroscopic and computational techniques. Based on the gained mechanistic understanding, their molecular structures, in particular their ligand structures, can synthetically be altered to optimise catalytic properties.[143, 144] A ruthenium-based metal complex featuring an equatorial terpyridyl dicarboxylate (tda) ligand and two axial pyridine (py) ligands developed by Llobet[29] was selected for the studies presented in this thesis (Figure 3.2.).
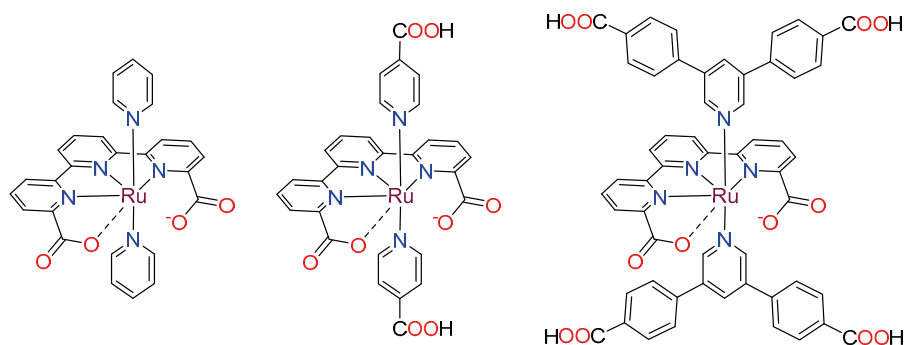

Figure 3.2. *Left, The original Ru(tda)(Py)$_2$ catalyst. Middle, the ditopic Ru(tda)(isonicotinic acid)$_2$ modification used for integration into a UiO MOF. Right, the tetratopic Ru(tda)(Py(PhCOOH)$_2$)$_2$ complex used for making a NU-1000 type mixed linker MOF.*

Upon application of an oxidising potential, [Ru^{II}(tda)([y)$_2$] converts to a Ru-aqua complex which is highly robust and active for catalytic water oxidation.[145-148] In fact, once the catalytically active Ru-aqua species is generated, the [Ru^{II}(OH$_2$)(tda)(py)$_2$] complex is counted among the most potent molecular water oxidation catalysts to-date. Its catalytic cycle, driven by step-wise oxidation of the Ru centre from +II to +V, involves multiple coordination rearrangements in and around the tda ligand, while the axial pyridine ligands stay permanently coordinated (Figure 3.3.).

In order to be incorporated into a MOF as a structural linker, the ruthenium water oxidation catalyst must be decorated with anchoring groups for SBU-ligation. Derivatives of [Ru^{II}(tda)(py)$_2$] should be particularly applicable MOF incorporation as they operate via a WNA mechanism, which does not require a bimolecular catalyst encounter as in the I2P radical coupling mechanisms. Synthetic manipulations of the equatorial tda ligand would likely disrupt the catalytic performance, so carboxylate anchoring groups were installed at the axial pyridine ligands, which are known to stay strongly bound to the Ru centre through the catalytic cycle.
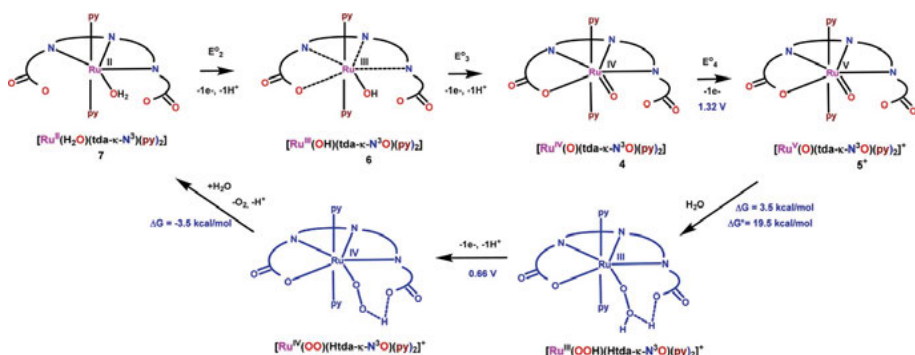
Figure 3.3. Proposed reactions involved in the water oxidation catalysis mechanism at pH 7.0 based on DFT calculations. Reprinted with permission from the Journal of American Chemical Society. R. Matheu et al. / J. Am. Chem. Soc. 2015, 137, 10786 − 10795.

For incorporation into a UiO-type MOF, a ditopic analogue with isonicotinic acid in the axial positions was synthesised. For incorporation into a NU-1000 type MOF, a tetratopic analogue is required, and $Py(PhCO_2H)_2$ ligands were prepared as axial ligands to the Ru complex. Both syntheses are described in more detail in the next section. Despite of the careful design described above, Ru-tda type complexes are potentially challenging to be integrated into a MOF for the following reasons:

1) The dihedral angle between the axial carboxylic groups is not fixed due to free rotation of the pyridyl ligands around the main axis of the complex, which may hinder MOF growth by obstructing pre-organisation of the anchoring groups.

2) The ruthenium centre is six-coordinate at low oxidation states and exhibits dynamic coordination behaviour, leaving one equatorial carboxylic acid groups uncoordinated. This dangling, carboxylate may potentially compete for SBU ligation and thereby disrupt ordered MOF growth.

3) The equatorial ligand is sterically demanding, which may introduce a significant steric stress that leads to highly defective or disordered materials.

3.3   Synthesis of $[Ru^{II}(tda)(pyR)_2]$

The tda ligand synthesis was optimised in order to remove any impurities, as described in previous reports, and to improve the scalability of the reactions. Commercially available terpyridine was oxidised using an existing protocol,[149] and the obtained N-oxides converted to the cyanides by the Reissert-

Henze reaction.[150] Final hydrolysis of the cyanides concluded the synthesis of the ligand (Figure 3.4.).
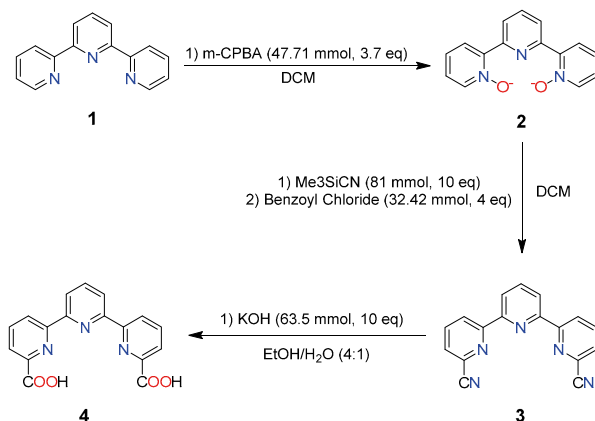
Figure 3.4. *Synthetic scheme for the synthesis of equatorial ligand [2,2':6',2''-terpyridine]-6,6''-dicarboxylic acid.*

The synthesis of the Py(PhCO$_2$H)$_2$ ligand was synthesised based on existing literature.[151] In short, the ligand was synthesized by a Suzuki cross coupling between 3,5-dibromopyridine and (4-(methoxycarbonyl)phenyl)boronic acid followed by saponification of the resulting methyl ester to afford the free carboxylate groups (Figure 3.5.).
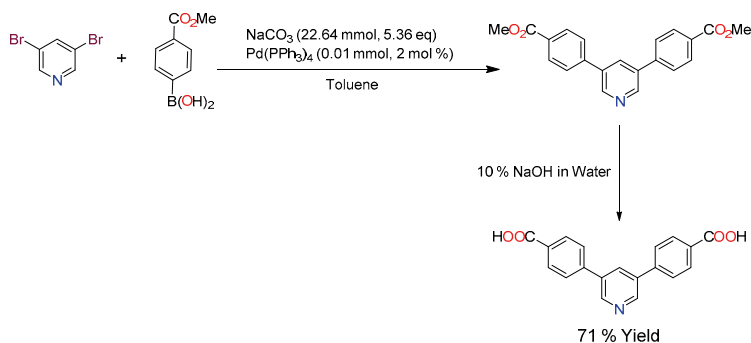
Figure 3.5. *Synthetic scheme for the synthesis of axial ligand 4,4'-(pyridine-3,5-diyl)dibenzoic acid.*

The 4,4',4'',4'''-(pyrene-1,3,6,8-tetrayl)tetrabenzoic acid used in paper II was synthesized according to adapted literature procedure[72].

The precursor complex Ru(tda)(dmso)(H$_2$O) was prepared from RuCl$_2$(dmso)$_4$ using a procedure from the literature,[29] and used for the coordinating of either the monotopic isonicotinic acid or the ditopic Py(PhCOOH)$_2$

ligands at the axial positions. The purity of the final products was confirmed by NMR spectroscopy and cyclic voltammetry.

Figure 3.6. *Synthetic scheme for the synthesis of 4,4',4'',4'''-(Pyrene-1,3,6,8-tetrayl)tetra-benzoic acid.*

Figure 3.7. *Synthetic scheme for the synthesis of Ru(tda)(PyCO₂H)₂ and Ru(tda)(Py(PhCOOH)₂).*

49

3.4 Synthetic Strategies for the Incorporation of Molecular Catalysts into MOFs

Three different methodologies were envisaged for the synthesis of UiO-type or NU-1000 MOFs with $[Ru^{II}(tda)(py)_2]$ metalo-linkers.
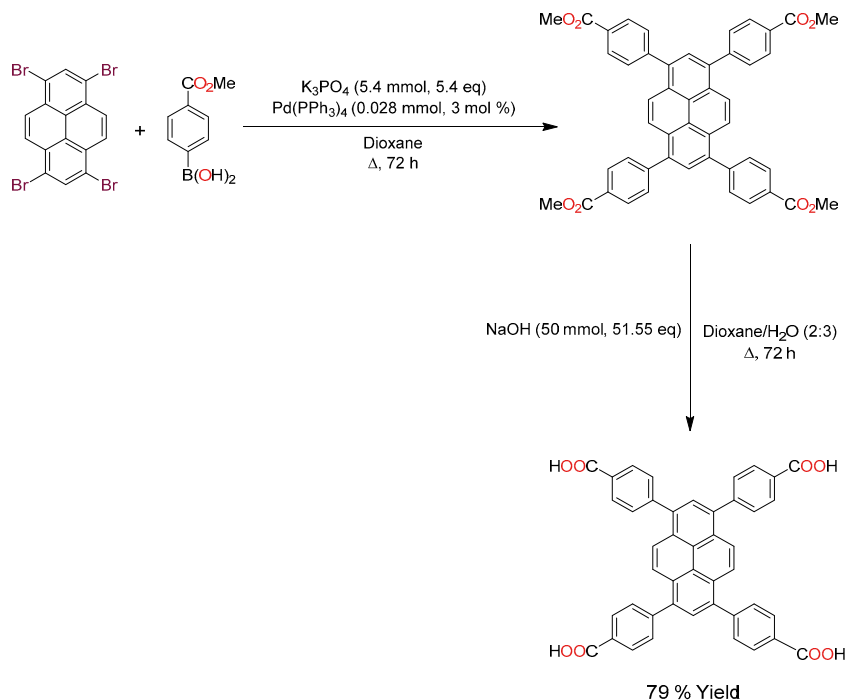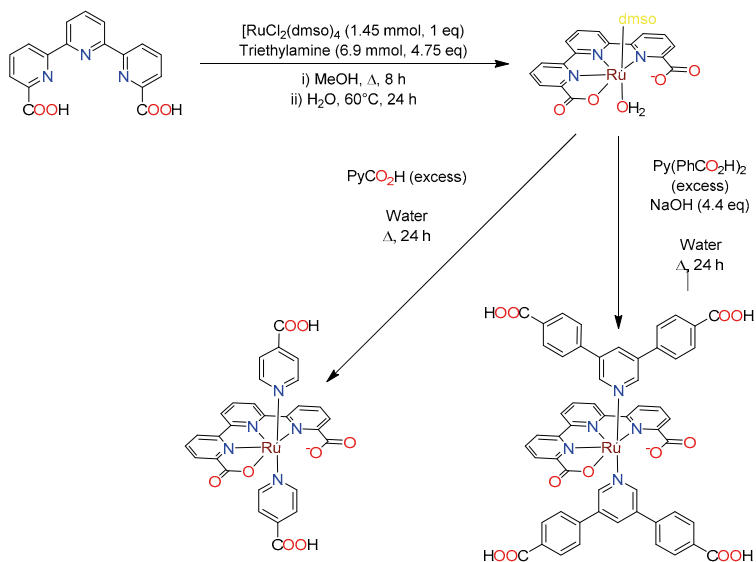
1) Direct solvothermal synthesis using $[Ru^{II}(tda)(PyCO_2H)_2]$ and $[Ru^{II}(tda)(PyCO_2H)_2]$ and as the sole linker. This is the most straightforward approach which, in theory, should result in MOFs with the highest possible catalyst loading. In these materials, the distance between redox active Ru centres is a short as possible, which is favourable for fast redox hopping charge transport.

2) Mixed-linker solvothermal synthesis where a sterically less demanding and inert co-linker is used in conjunction with another linker (in this case, a molecular water oxidation complex). This strategy may resolve problems arising from the sheer steric bulk of the Ru metallo-linker, and space out the catalytically active linkers.

3) An indirect approach where the metallo-linkers is post-synthetically introduced into a pristine parent MOF with linkers of matching length. This strategy avoids subjecting the molecular catalysts to the harsh solvothermal synthesis conditions that are often needed for MOF synthesis. This is particularly valuable for linkers which are temperature and solvent sensitive.

The direct approach has been previously used for porphyrin- or phthalocyanine-based catalyst linkers.[59, 77, 79, 127, 130] While co-synthesis strategies have also been reported with ruthenium molecular complexes for the synthesis of UiO-67 type and $Co^{(II)}$-MOFs [118, 128, 129]

These papers outline strategies to use co-linker strategies and indirect strategies of incorporation of a molecular complex for water oxidation inside MOFs.

1. Direct solvothermal synthesis
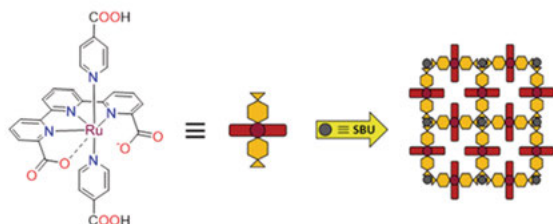
2. Direct co-synthesis
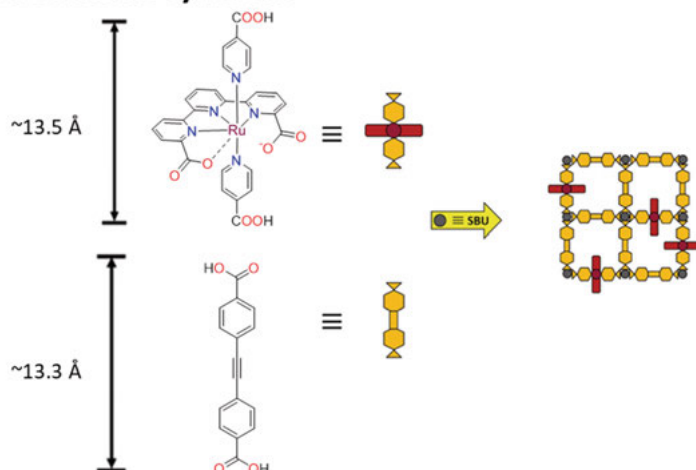
3. Indirect preparation through post-synthetic modification
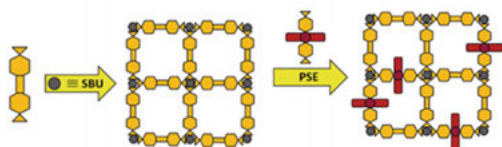
Figure 3.8. *Strategies of making MOFs with catalytic Ru(tda)(PyCO2H)2 linker. Reprinted with permission from the Royal Society of Chemistry. T. Liseev et al / Dalton Trans., **2020**, 49, 13753 - 13759.*

3.5 UiO-Type Topology Prepared via Post Synthetic Modification

3.5.1 Direct Solvothermal Synthesis and Co-Synthesis

DMF is a common choice for solvothermal synthesis of UiO-type MOFs, but DMF (and amines that may arise from DMF decomposition) may compete for coordination to the ruthenium centre. To reduce this probability,

dimethylacetamide (DMA) was used as the solvent for the MOF synthesis, being a bulkier analogue to DMF.

Therefore, $[Ru^{II}(tda)(PyCO_2H)_2]$ was mixed with $ZrOCl_2(H_2O)_8$ in a 1:1 molar ratio in DMA (38 μmol/3 mL), and a tenfold excess of mediator (either formic acid, acetic acid or benzoic acid) was added. The mixture was sonicated for 1 h, sealed in a vial and incubated at temperatures between 80°C and 120°C for two days. Despite a large number of attempts, the material that was obtained from the direct synthesis attempts, after washing and drying was found to be mostly amorphous by PXRD analysis (**1**) (Figure 3.9.)

Direct co-synthesis was then subsequently explored, using inert linkers to space out the complex to achieve the desire MOF lattice. Ethynedibenzoic acid (edba) was chosen as the co-linker due to its matching length with the $[Ru^{II}(tda)(PyCO_2H)_2]$ linker (13.3 Å and 13.5 Å, respectively), as well as its structural rigidity.
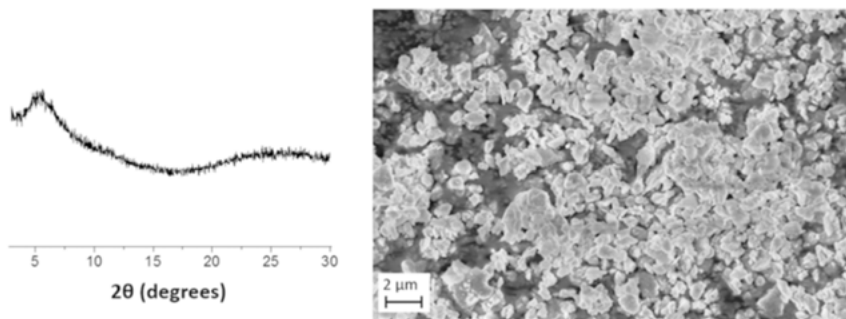
Figure 3.9. *PXRD pattern (left) and SEM micrograph (right) of material **1** demonstrating its amorphous nature. Reprinted with permission from the Royal Society of Chemistry. T. Liseev et al / Dalton Trans., **2020**, 49, 13753 - 13759.*

The solvothermal synthesis conditions that were tested were analogous to those employed above, with the addition of the extra edba linker. Different molar ratios of $[Ru^{II}(tda)(PyCO_2H)_2]$: edba were tested (1:1, 1:4 and 1:8), but unfortunately, none of these attempts with the co-linker were successful and only amorphous materials (**2**) were obtained (Figure 3.10.).

From a synthetic viewpoint, both the direct and co-synthesis approaches using the diatropic $[Ru^{II}(tda)(PyCOOH)_2]$, resulted in the formation of amorphous material, which indicates that the steric bulk of the metallo-linker is not the deciding factor that gives rise to the inability of the material to crystallize into a regular lattice. Instead, the conformational flexibility of the $[Ru^{II}(tda)(PyCO_2H)_2]$ complex itself may not be compatible with ordered MOF growth under direct solvothermal synthesis conditions.

In addition, the $[Ru^{II}(tda)(PyCO_2H)_2]$ linker may also fail to form a MOF due to potential ambiguity in SBU-coordinating sites within the Ru linker. There is an indication that the SBU-coordination occurs via the axial carboxylates and through the equatorial carboxylate groups, which in low Ru oxidation states are not coordinating the ruthenium centre.
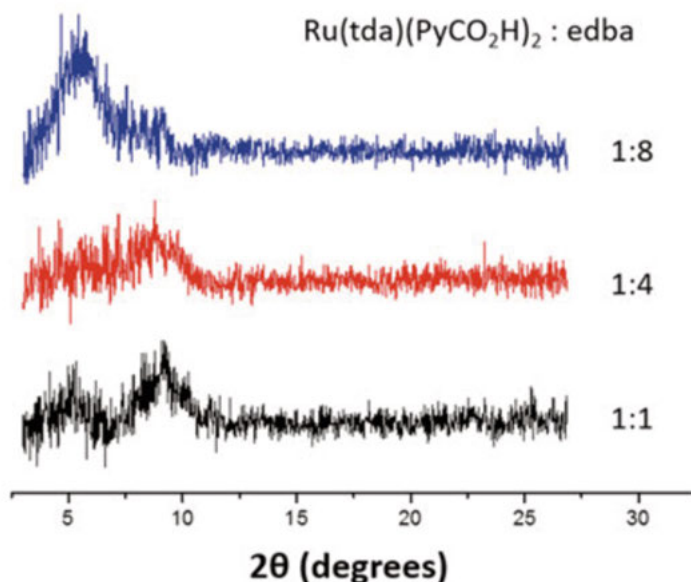
Figure 3.10. *PXRD patterns of the products of direct synthesis with varying ratios of co-linkers, all showing an amorphous phase. Reprinted with permission from the Royal Society of Chemistry. T. Liseev et al / Dalton Trans.,* **2020,** *49, 13753 - 13759.*

In order to circumvent the ambiguity of the binding modes during solvothermal synthesis, an indirect approach for the incorporation of the catalyst was chosen and the framework was constructed prior to catalyst incorporation. Hence, the edba and $ZrOCl_2(H_2O)_8$ were mixed in DMA (38 μmol/3 mL), in a 1:1 molar ratio, with a 10 equivalent molar excess of formic acid (modulator). The mixture was sonicated for 1 h, sealed in a vial and incubated in an oven at 135 °C for 2 days (materials **3** & **4**). The post-synthetic exchange (PSE) was carried out by suspending 10 mg of MOF to 3 mM of $[Ru^{II}(tda)(PyCO_2H)_2]$ in 3 mL of methanol, incubated on a shaker overnight at room temperature, and the obtained MOF was subsequently washed with EtOH (**5** & **6**).

3.5.2   Structural Characterisation of MOFs

Upon examination with XRD, the direct synthesis, **1**, and co-synthesis attempts, **2**, showed no formation of crystalline material, as described above.

For the post-synthetic introduction of the Ru metallo-linker, the pristine parent UiO-type MOF was prepared with the size matched edba linker first. Examination of different batches of the ebda-MOF by SEM showed two different morphologies, one forming an octahedral MOF, **3**, and the other forming the interlaced MOF, **4**, (Figure 3.11.). An analogous, interlaced MOF morphology has been observed previously for UiO-66.[153, 154] In the present case, one morphology tends to dominate the entire batch, but both materials exhibit identical PXRD patterns, although the pattern of the octahedral morphology is generally characterised by sharper reflections.

Both morphologies result from the same preparation protocol, but through examination of all reaction parameters revealed that the morphology is decided by small difference in the Zr : edba that is used in the solvothermal synthesis. It was found that a small, excess of SBU leads to the interlaced morphology. The reason for the initial somewhat random reaction outcomes lies in the fact that $ZrOCl_2(H_2O)_8$ is highly hygroscopic in nature, which complicates precise control in the weighing process.

Both octahedral MOF **3** & interlaced MOF **4,** were subjected to post-synthetic linker exchange (PSE) to assess the impact that the morphology has on the incorporation yield of the metallo-linker, and whether missing linker defects are filled,[155] This provided the powder diffraction patterns for MOFs **5** & **6**, where all major peaks remain intact and their positions conserved, which demonstrates overall retention of MOF structure under the PSE conditions (Figure 3.12.).
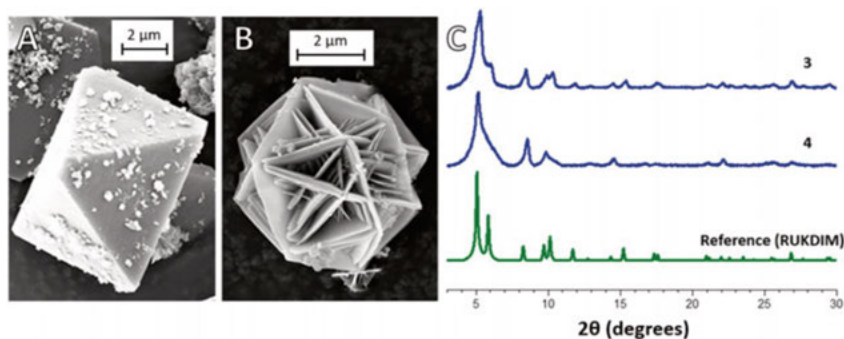
Figure 3.11. *Characterisation of edba-MOF. SEM micrographs of (A) octahedral crystal morphology of material 3. (B) interlaced crystal morphology of material 4. (C) PXRD patterns of octahedral material 3 and interlaced material 4 in comparison to the published pattern. Reprinted with permission from the Royal Society of Chemistry. T. Liseev et al / Dalton Trans., 2020, 49, 13753 - 13759.*
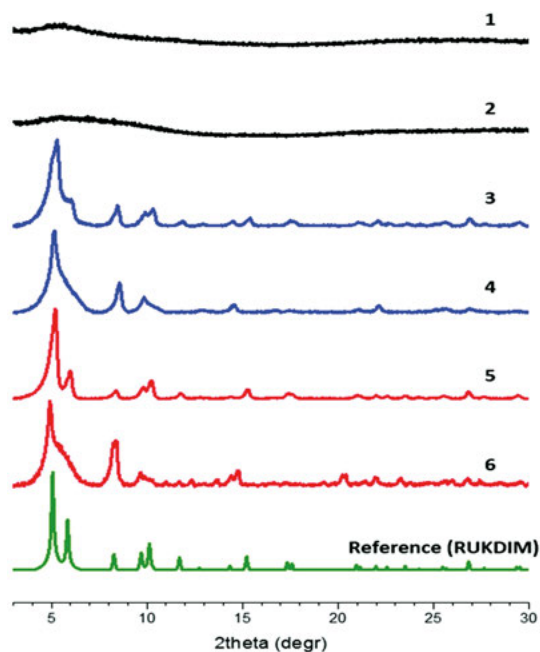
Figure 3.12. *PXRD patterns of amorphous materials **1** (from solvothermal synthesis) and **2** (from mixed-linker solvothermal synthesis), edba-MOF **3** and **4** and **5** and **6** (with post-synthetically introduced Ru linker), in comparison with a literature reference pattern. The patterns are grouped by colours: amorphous materials (black), pristine edba-MOFs (blue), Ru-edba MOFs (red), reference pattern (green, CSD identifier RUKDIM). Reprinted with permission from the Royal Society of Chemistry. T. Liseev et al / Dalton Trans., **2020**, 49, 13753 - 13759.*

Nitrogen adsorption and desorption isotherms were recorded to assess total internal surface area of both of the parent MOFs, **3** & **4**, and how it changes with incorporation of the Ru metallo-linker. The BET surface area for **3** was determined to be 1300 m^2 g^{-1}, while that of **4** is only 390 m^2 g^{-1}, with the disparity in surface area due to the larger abundance of missing linker defects in **4**. The hysteresis in the isotherm of **4** indicates the presence of mesopores, as the result of the high number of defects.
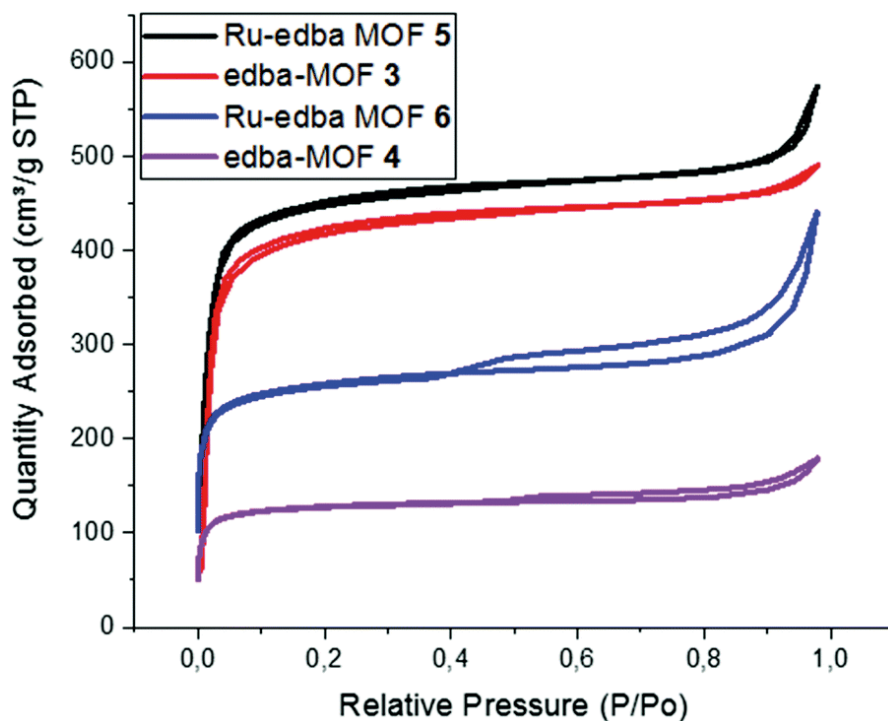
Figure 3.13. *N_2 sorption isotherms of edba-MOF **3** to **6**. The octahedral edba-MOF **3** and Ru-edba-MOF **5** show overall higher adsorption profile. The interlaced edba-MOF **4** shows a hysteresis indicative of mesopores. For both morphologies, incorporation of the Ru(tda)(PyCO$_2$H) linker increases internal surface area. Reprinted with permission from the Royal Society of Chemistry. T. Liseev et al / Dalton Trans., **2020**, 49, 13753 - 13759.*

The literature value reported for the same edba MOF (BUT-30[156]), 3941 m^2 g^{-1}, surpasses that of the material obtained by our synthetic method by a factor of 2 in case of MOF **3** and factor of 10 for MOF **4**, which is consistent with less missing-linker defects in BUT-30. There is a number of reports correlating internal surface area of MOFs to the amount of defects, some of which indicate that more defects lead to higher BET surface areas,[157] while others show the opposite, i.e. more defects give rise to lower surface areas.[158]

A notable report from Wang et al. demonstrates how the BET surface area in UiO-66 grows with increasing defects up to a threshold amount, but then begins to drop.[159] It appears that the amount of missing-linker defects in the MOF is above this threshold. This conclusion is corroborated by the fact that the BET surface areas for both morphologies increase upon incorporation of the Ru (tda) linkers, with **5** and **6** exhibiting a surface area of 1390 m^2 g^{-1} and 800 m^2 g^{-1}, respectively. This finding also indicates that the major mechanism of incorporation is probably replacement of the modulator and solvent molecules at the nodes rather than the exchange of edba struts.

3.6 Cyclic Voltammetry

All measurements were performed in pH 7.0 phosphate buffer (0.1 M), using an Ag/AgCl reference electrode, a GC counter electrode, and a scan rate $v = 0.1$ V/s, unless stated otherwise. The homogeneous $[Ru^{II}(tda)(PyCOOH)_2]$ complex was measured to obtain its characteristic redox features for reference purposes. The CV of the molecular reference complex features two well-separated reversible waves that correspond to $Ru^{(III/II)}$ and $Ru^{(IV/III)}$ redox transitions. If the complex is successfully incorporated into a MOF, we expect these features to be qualitatively conserved.
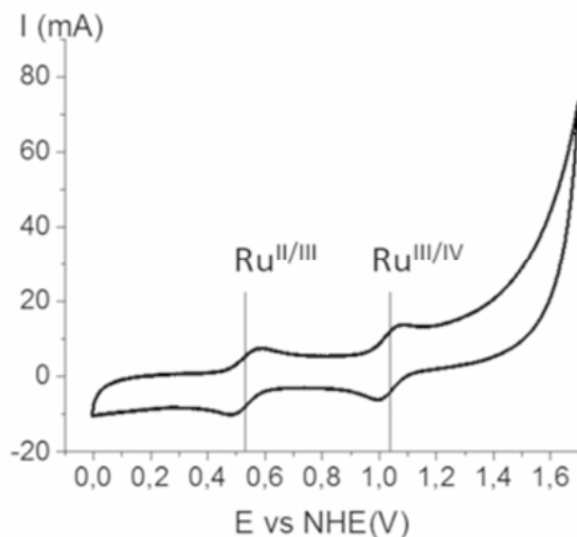
Figure 3.14. *Cyclic voltammogram of homogeneous Ru(tda)(ina)₂ complex in 0.1 M pH 7.0 phosphate buffer. Reprinted with permission from the Royal Society of Chemistry. T. Liseev et al / Dalton Trans.,* **2020***, 49, 13753 - 13759.*

For their electrochemical characterisation, materials 1-6 (amorphous or MOF) were separately suspension of multi-walled carbon nanotubes and drop casted onto glassy carbon electrodes, followed by air drying. The direct and co-synthesis materials **1** and **2** exhibited CV's with multiple redox couples, which indicates the presence of at least two different Ru species. In contrast, CVs of the Ru-edba-MOFs **5** and **6** displayed two simple oxidation waves at identical potentials as those of the $Ru^{(III)}/ Ru^{(II)}$ and $Ru^{(IV)}/Ru^{(III)}$ redox couples in the homogenous $[Ru^{II}(tda)(PyCOOH)_2]$ reference.

When the overall crystallinity of the MOF is pre-determined by the pristine MOF **3** and **4**, incorporation of the Ru-linker seems to proceed in the envisaged fashion through the axial iso-nicotinic acid groups, and is not disturbed by the dangling carboxylates at the tda ligand. While the above work established a viable synthetic pathway for the immobilisation of the Ru metallolinker in a MOF, the obtained materials 5 and 6 fell short in showing electrocatalytic water oxidation activity. This behaviour of the MOF-confined catalyst is in contrast to that of the catalyst linker in homogeneous phase. The exact reason for the lack of activity when immobilised in the MOF is unclear at present.
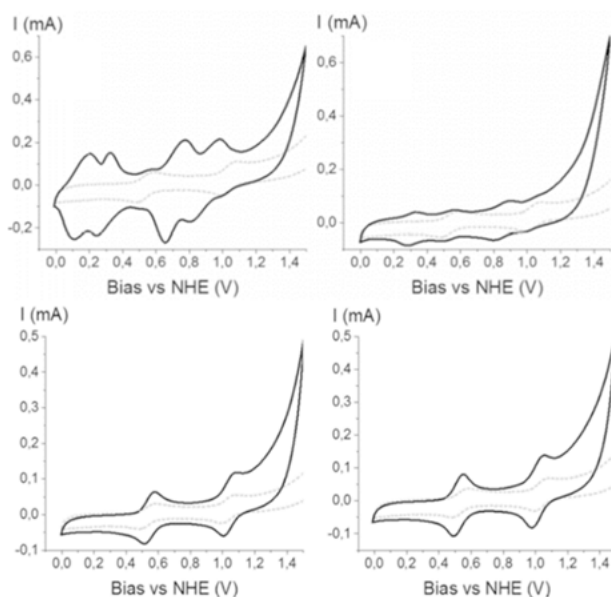
Figure 3.15. *Top left, Cyclic voltammograms of **1**, product of direct solvothermal synthesis. Top right, **2**, product of the co-synthesis with edba. Bottom left, octahedral Ru-edba-MOF **5**. Bottom right, interlaced Ru-edba-MOF **6**. Grey dotted lines represent the reference CV of the homogeneous complex for comparison. Reprinted with permission from the Royal Society of Chemistry. T. Liseev et al / Dalton Trans., **2020**, 49, 13753 - 13759.*

4 Electrocatalytic Water Oxidation from a Mixed Linker MOF Based on NU-1000 with an Integrated Ruthenium-Based Metallo-Linker (Paper II)

4.1 Introduction

In a follow-up study to the one in chapter 3, a tetratopic version of the $[Ru^{II}(tda)(py)_2]$ complex bearing $Py(PhCOOH)_2$ (4,4'-(pyridine-3,5-diyl)dibenzoic acid) ligands at the axial positions, was explored for its incorporation into NU-1000 type MOF structures. The native linker of that MOF is H_4TBAPy (1,3,6,8-pyrenetetrayl)tetrakisbenzoic acid), which is similar to the tetratopic $[Ru^{II}(tda)(Py(PhCOOH)_2)_2]$ complex in terms of geometry and dimensions, both of which are factors that should enable facile linker incorporation.

From a thermodynamic viewpoint, the use of TBAPy as a co-linker to the $[Ru^{II}(tda)(Py(PhCOOH)_2)_2]$ is promising as the formal potential for TBAPy oxidation in NU-1000 has been reported as 1.1 V and 1.4 V *vs.* Ag/AgCl in CH_2Cl_2[160] and CH_3CN[102], respectively. For the purposes of this thesis, $[Ru^{II}(tda)(Py(PhCOOH)_2)_2]$ will be abbreviated as **I**.

TBAPy-based oxidations in NU-1000 are sufficiently anodic to not interfere with the $Ru^{(III/II)}$ and $Ru^{(IV/III)}$ couples of the $[Ru^{II}(tda)(py)_2]$-based linker which are expected to be cathodic of 1.0 V. At such potentials, the native NU-1000 framework is expected to behave as an inert matrix.[85, 102, 161]

The situation can however be expected to change at potentials at which water oxidation occurs, typically at onset potentials just beyond 1.0 V vs. NHE. At these potentials, TBAPy oxidation in NU-1000 can be expected. Thus, the TBAPy linkers may provide a hole transport pathway to efficiently deliver oxidizing equivalents to **I**. In an ideal scenario, the pyrene linkers may provide a hole transport pathway also to catalyst linkers that are remote from the MOF/electrolyte interface, i.e. in the core of the MO crystals, giving rise to efficient use of catalyst linkers and high current densities. The co-synthesis approach involving the Ru-tda and the TBAPy linker, are the focus of paper II.

4.2 Metallo-Linker Synthesis and Characterisation

The synthetic sequence to $[Ru^{II}(tda)(Py(PhCOOH)_2)_2]$ is outlined below in Figure 4.1. The $Py(PhCOOH)_2)$ ligand that provides the coordination bonds to the SBUs was prepared via a Pd-mediated Suzuki cross coupling reaction between 3,5-dibromopyridine and (4-(methoxycarbonyl)phenyl)boronic acid in refluxing dioxane/water (11:1). The obtained methyl ester was saponified by refluxing in an aqueous sodium hydroxide solution to afford the unprotected ligand in 71 % yield over both steps (Figure 4.1).

The target metallo-linker was assembled by heating two equivalents of the ligand $Py(PhCOOH)_2$ with $[Ru^{II}(tda-k-N^3O)(dmso)(OH_2)]$ in water with a small quantity of NaOH to reflux for one day. $[Ru^{II}(tda)(Py(PhCOOH)_2)_2]$ (**I**) was obtained in an isolated yield of 34 % (Figure 4.1). Single crystals of **I** could be obtained by slow diffusion of diethyl ether into a solution of the complex in a DMSO/DMF mixture. Structure elucidation by single crystal X-ray diffraction revealed an octahedral geometry and the expected coordination environment around the ruthenium centre, where tda^{2-} coordinates the Ru centre in a $\kappa-N^3O^1$ manner, similar to previous examples of this type of complexes in the literature (Figure 4.2.).[162]
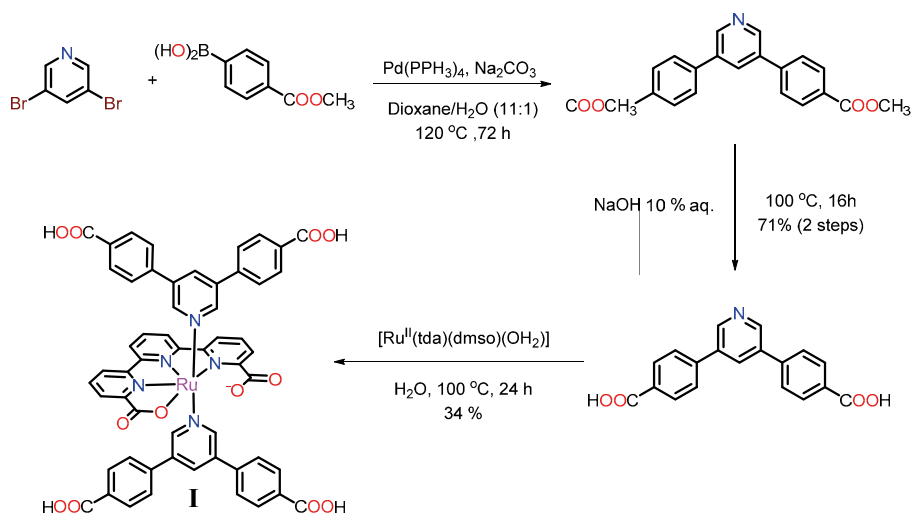
Figure 4.1. *Synthetic scheme for the synthesis of complex **I**.*
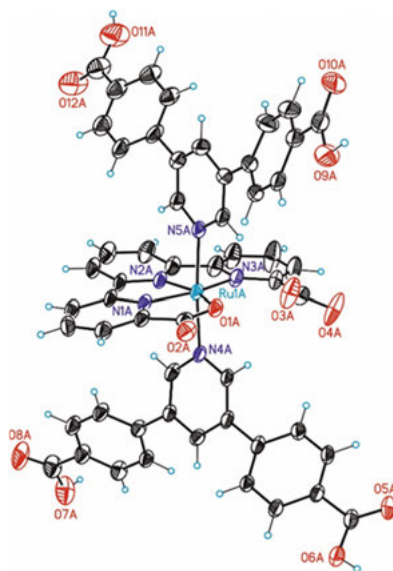
Figure 4.2. *X-ray crystal structure of **I**.*

4.3   Mixed Linker MOF Synthesis and Characterisation

Initial attempts to produce a crystalline material by direct solvothermal synthesis using **I** as the sole linker were not successful, despite the testing of a broad range of different conditions. Considering the geometric similarities between **I** and the pyrene-based H₄TBAPy linker in NU-1000, the possibility to dope NU-1000 with complex **I** during the solvothermal synthesis was explored.

Using the optimised conditions for phase-pure NU-1000 preparation,[163] the H₄TBAPy linker was complemented by **I** in the solvothermal synthesis. In total, seven materials were prepared by increasing the proportions of the metallo-linker in increments of 5 % from 0 to 30 % relative to the ZrOCl$_2$ precursor. NU-1000 synthesis in the absence of any Ru dopant confirmed the reproducibility of the synthetic procedure in our hands, and provided a material to which all Ru-doped materials were compared to.

The amount of Ru doping was quantified by ICP-OES analysis of samples that had been digested in concentrated H$_2$O$_2$/HNO$_3$. While the amount of Ru present in the mixed linker MOFs increased with increasing proportions of the metallo-linker in the solvothermal syntheses, a linear correlation could not be established. The mixed-linker MOF materials can be grouped into two categories, those that have a low Ru content, ≤ 1.5 %, and those with a higher content of ≥4 % relative to Zr. A transition between these two groups is

observed when the proportion of **I** exceeds 15 mol % relative to $ZrOCl_2$ in the solvothermal syntheses (Table 1)

Table 1. *Comparison between the ratios of [Ru^{II}(tda)(Py(PhCOOH)_2)_2] (**I**) and ZrOCl_2 that were used in the solvothermal syntheses (in mol%) and the actual incorporation of the mixed linker MOFs. Conditions: ZrOCl_2.8H_2O, 35 mol% H_4TBAPy, benzoic acid, DMF, 100°C, 3 d. Reprinted with permission from the Royal Society of Chemistry. A. Howe et al / Mater. Adv.,* ***2022****, 3, 4227 - 4234.*

I **used in solvothermal synthesis** **in mol% relative to ZrOCl₂**	**I** **in final mixed linker MOF** **in mol% relative to Zr,** **as determined by ICP-OES**
5	< 0.1
10	0.6
15	1.6
20	4.8
25	4.1
30	5.7

4.4 Structural Characterisation of Mixed Linkers MOFs

All mixed-linker solvothermal syntheses produced crystalline materials, as visible by their powder X-ray diffraction patterns (Figure 4.3). The reflections of the PXRD are largely located in similar positions as those found in NU-1000,[164] with each sample displaying three clearly visible reflections at $2\theta =$ 5.2°, 7.5° and 10.4°.

Upon increasing proportions of the Ru linker in the solvothermal syntheses, a gradual decrease in the intensities of the PXRD reflections can be observed, which can be assigned to decreased crystallinity of the samples. In fact, gradually decreasing crystallinity is consistent with further experiments in which the Ru linker content was as high as 75 to 100% relative to $ZrOCl_2$, and that do not produce any crystalline material. The SEM images of the material show the average crystal size decreasing down from ~4 μm down to sub-micrometer dimensions with increasing levels of Ru doping.
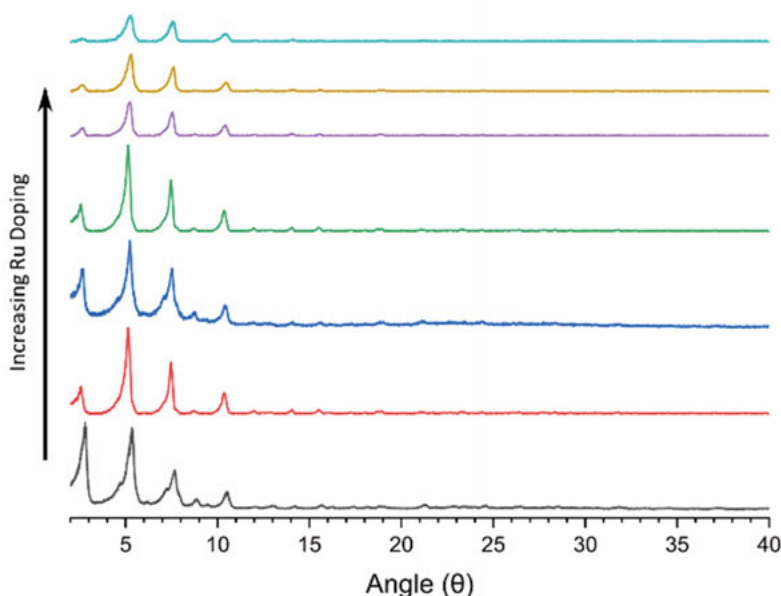
Figure 4.3. *Powder X-Ray Diffraction (PXRD) patterns of the mixed linker MOFs. NU-1000 (black trace) and mixed-linker NU-1000-Ru with increasing proportions (from 5 to 30 %) of* **I** *as indicated by the arrow. Reprinted with permission from the Royal Society of Chemistry. A. Howe et al / Mater. Adv.,* ***2022,*** *3, 4227 - 4234.*

Inspection of the scanning electron micrographs of the mixed linker MOFs show that the preparations with low Ru content yielded rod-shaped crystals similar in morphology and size to NU-1000. Increasing Ru contents lead to a significant smoothening of the crystal contours, and a decrease in crystal size (Figure 4.4.). In the most extreme case, particle morphology deviates significantly from hexagonal rods as in case of NU-1000, and are better described as almost spherical. Similar to what was observed with the PXRD. Also, SEM analysis showed that increasing ruthenium loadings show a decrease in crystallinity, with reactions loadings greater than 75 mol % resulting in amorphous material being produced.

The presence of complex **I** in the mixed linker MOFs was evidenced by FTIR spectroscopy which showed peaks that are assigned to the metallo-linker. Transitions at 1697 cm^{-1}, 1097 cm^{-1} (C-O stretch), 865 cm^{-1}, 784 cm^{-1} and 717 cm^{-1} correspond to those found in the FTIR spectrum of the homogenous linker. Additionally, Ru doping was also examined by energy-dispersive X-ray spectroscopy (EDX), which further confirmed the presence of ruthenium throughout the materials.
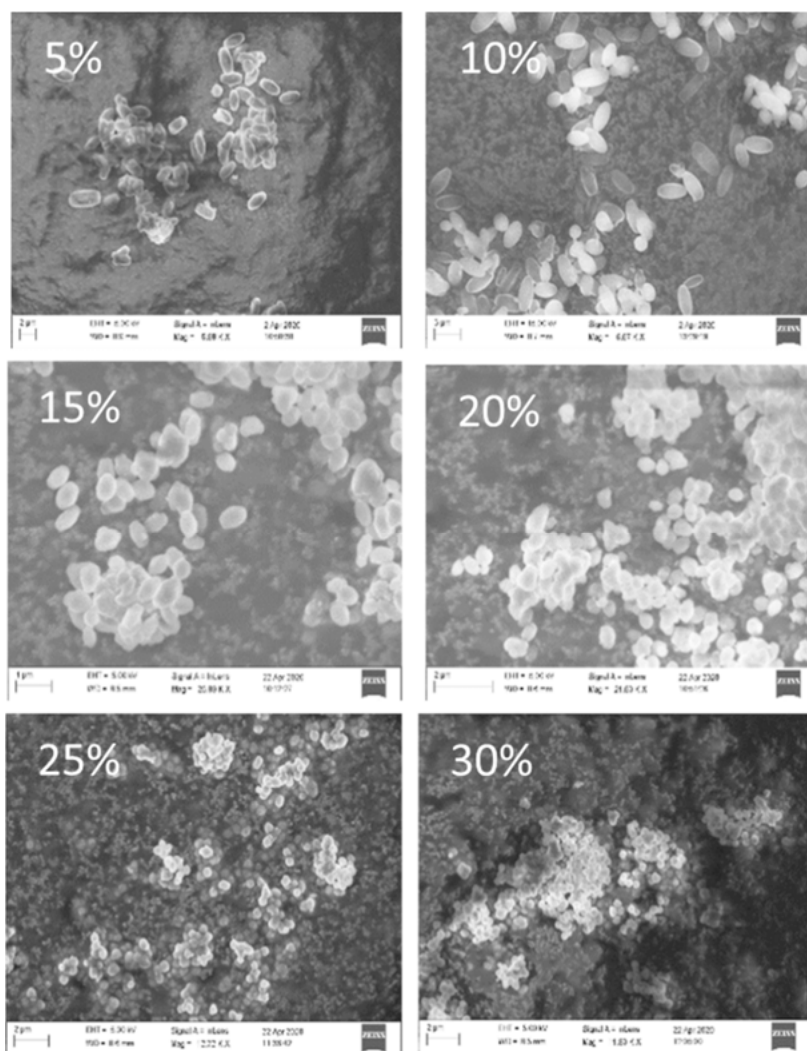
Figure 4.4. *Scanning electron micrographs of the obtained mixed linker MOF materials: from top left to bottom right are shown the MOFs obtained from solvothermal synthesis where the content of **I** was systematically increased from 5 to 30 mol% (in steps of 5%) relative to the used ZrOCl₂. Reprinted with permission from the Royal Society of Chemistry. A. Howe et al / Mater. Adv., **2022**, 3, 4227 - 4234.*

The fact that the ratio between the different linkers in the solvothermal synthesis is not directly mirrored in their abundance in the mixed linker MOF has ample precedence in the literature. The phenomenon is usually ascribed to a situation where different linkers have different propensities to form MOFs, for example, as a result of different pK_a values of coordinating carboxylates.[165]

However, in such cases, a linear correlation between linker proportion in the synthesis and their presence in the MOF is still observed. In the present case,

the co-incorporation of the **I** and H$_4$TBAPy linkers seems to be disturbed by additional factors. One such factor may be the poor solubility of **I** under the solvothermal conditions, or its higher degree of rotational freedom around the axial N-Ru-N vector.

4.5 Electrochemistry and Water Oxidation Properties

Being a new member of the Ru(tda) family of water oxidation catalysts, the electrochemical behaviour of **I** in water was investigated using a glassy carbon disk as working electrode, a platinum mesh counter electrode and Ag/AgCl (3 M NaCl) as a reference electrode. Unless otherwise stated, all CVs are reported under these conditions and the potentials are converted to NHE by adding 0.2 V to the measured potential. Initial cyclic voltammograms (CVs) of aqueous solutions of complex **I** in 0.1 M sodium phosphate buffer (pH 7) gave inconclusive results due to the hydrophobicity of the complex and its associated low solubility.

Thus, complex **I** was suspended with multi-walled carbon nanotubes (MWCNTs) in THF, and subsequently drop-casted onto glassy carbon disk electrodes. The CV of **I** at pH = 7 shows two reversible waves at $E_{1/2} = 0.61$ V and $E_{1/2} = 1.09$ V that are assigned to the Ru$^{(III/II)}$ and Ru$^{(IV/III)}$ couple, respectively (Figure 4.5, black trace).

As for all complexes of the Ru(tda) family, also complex **I** is a pre-catalyst that needs to be activated under oxidizing conditions to reveal its full catalytic potential. This oxidative activation converts the complex to a Ru$^{(IV)}$ state and establishes the indispensable Ru-OH$_2$ unit.[29] Full activation of surface-immobilised **I** was achieved by controlled potential electrolysis (CPE) at 1.4 V in a pH 12 phosphate buffer solution (0.1 M) for a period of 40 minutes. As a result, a shift of the redox waves associated with the Ru$^{(III/II)}$ and Ru$^{(IV/III)}$ couples to $E_{1/2} = 0.52$ V and $E_{1/2} = 0.70$ V is observed, respectively, followed by a large catalytic current associated with electrocatalytic oxidation of water to dioxygen at an onset potential of around 1.19 V (Figure 4.5, red trace). The lower currents of the Ru$^{(III/II)}$ and Ru$^{(IV/III)}$ waves after activation are presumably due to partial leaching of the complex from the electrode, which becomes more soluble in water after deprotonation of carboxylic acid functionalities during the activation step at pH 12.
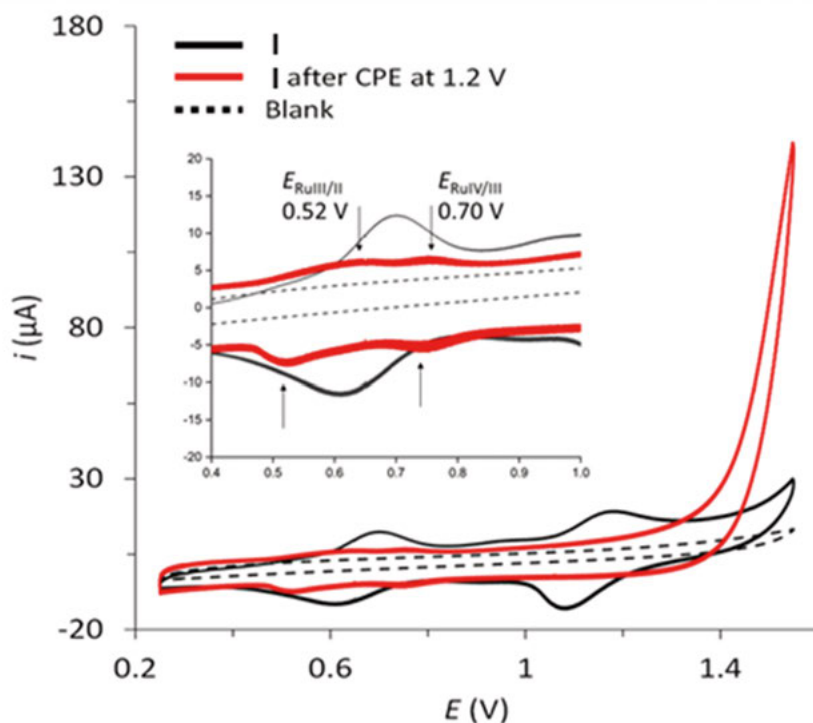
*Figure 4.5. Cyclic voltammogram of **I** immobilised with MWCNTs on a glassy carbon electrode prior to (black trace) and after (red trace) the activation procedure (controlled potential electrolysis at 1.2 V). Background glassy carbon electrode (black dotted trace). 0.1 M phosphate buffer electrolyte; pH = 7; v = 100 mV/s. Inset shows a zoom into the oxidation waves observed after catalyst activation. Reprinted with permission from the Royal Society of Chemistry. A. Howe et al / Mater. Adv., **2022**, 3, 4227 - 4234.*

With NU-1000 and mixed linker MOF materials in hand, focus was directed towards their electrocatalytic water oxidation activity. Similar to the measurements of the homogenous **I**, the MOFs were suspended and sonicated in THF, mixed with a separately prepared suspension of MWCNTs, and drop-casted onto glassy carbon working electrodes (see Figure 4.6.).

Multiple CV scans of NU-1000 was carried out at pH 7 in a phosphate buffer (0.1 M). The first CV scan (in blue) shows an anodic feature in the range of 1.0-1.4 V that is assigned to the oxidation of the TBAPy linker. This cannot be directly compared to other literature as other electrochemical analysis were performed in organic solvent.

In the aqueous phosphate buffer used, this oxidation is electrochemically irreversible, and the corresponding cathodic feature in the reverse scan of the CV is largely absent. Consequently, consecutive CV cycles show a continuous

decrease of the TBAPy oxidation and new waves appear in the range of -0.2 to 0.3 V. The appearance of these features is assigned to TBAPy-derived products that are formed in the electrochemically irreversible oxidation of the linkers.
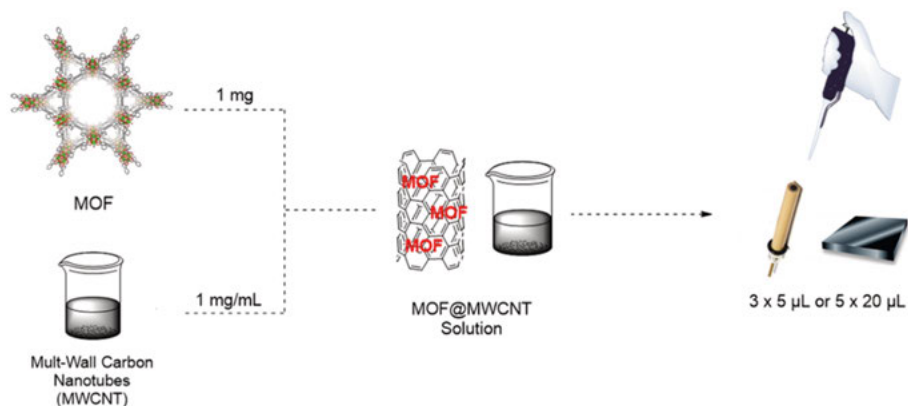
Figure 4.6. *Preparation of MOF electrode via drop casting. Reprinted with permission from the Royal Society of Chemistry. A. Howe et al / Mater. Adv., **2022**, 3, 4227 - 4234.*

The CV of the mixed linker MOF with the highest content of **I** (5.7 %), NU-1000-Ru$_{high}$, is shown in (Figure 4.7. A) together with that of NU-1000 (Figure 4.7. B). For NU-1000-Ru$_{high}$, an additional anodic wave can be observed at $E_{p,a}$ = 0.8 V that is absent in the parent MOF. Consequently, this wave is assigned to the incorporated Ru linker. Finally, the 20th CV scan for both NU-1000 and NU-1000-Ru$_{high}$ are compared to each other to observe the redox potentials of the complex in the mixed linker MOF (Figure 4.7. C).

While the CVs of both materials show the TBAPy-derived product linkers at potentials more negative than 0.3 V, the 20th CV scan of NU-1000-Ru$_{high}$ shows the evolution of additional waves at $E_{1/2}$ = 0.55 and 0.71 V. At the same time, the anodic feature at $E_{p,a}$ = 0.8 V is absent. The new waves are typical for activated forms of Ru(tda) complexes,[29] and are a further demonstration for the successful incorporation of the Ru-linker into NU-1000 material.

The currents for the Ru-based oxidations at the glassy carbon electrode are relatively low, as the number of Ru-linkers that are in close contact to the MWCNT is small, and Ru-to-Ru electron hopping charge transport can be expected to be very slow due to the low incorporation yield of **I** and resulting large spatial separation.[166] The TBAPy linkers are not conducting at potentials below 1.0 V either,[167] thus do not provide hole transport pathways at potentials of, for example, the Ru$^{(III/II)}$ couple.[168]
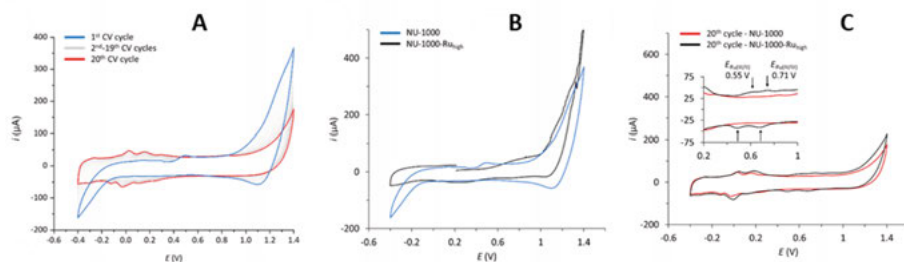
Figure 4.7. *Cyclic voltammetry of MOFs immobilised together with MWCNTs on glassy carbon working electrodes (0.1 M phosphate buffer electrolyte; pH = 7; ν = 100 mV/s.). A: Multiple scans of NU-1000. Initial cycle of NU-1000 (black trace), cycles 2 – 19 (grey trace) and final cycle of NU-1000 (red trace). B: Initial cycles of NU-1000 (black trace), and NU-1000-Ru$_{high}$ (blue trace). C: 20th CV scans of NU-1000 and NU-1000-Ru$_{high}$; inset shows a zoom into the Ru-based oxidations of NU-1000-Ru$_{high}$. Reprinted with permission from the Royal Society of Chemistry. A. Howe et al / Mater. Adv.,* **2022***, 3, 4227 - 4234.*

This situation however changes at more positive potentials at which TBAPy oxidation occurs and hole hopping transport throughout the whole crystalline material is enabled. Every oxidized TBAPy linker is a sufficiently strong oxidant to drive the oxidation of the Ru linkers through a mediated process. In other words, while the direct oxidation of **I** in CV experiments may be limited to near-surface site, potentially all Ru-linkers can be oxidized via the TBAPy moieties at higher applied potentials. Consequently, the Ru$^{(III/II)}$ and Ru$^{(IV/III)}$ oxidations may only feature as very small waves in the CVs of NU-1000-Ru$_{high}$, but will nevertheless occur in a TBAPy-mediated process at more positive applied potentials.

With the possibility to engage a large proportion of the metallo-linkers in catalysis, CPE experiments were conducted with NU-1000-Ru$_{high}$ to evaluate its capacity to catalyse electrochemical water oxidation. NU-1000-Ru$_{high}$ was used as the working electrode in a gas-tight two-compartment electrochemical cell that was coupled to a Clark-type electrode to measure oxygen evolution. Oxygen evolution as a function of time during at an applied potential of 1.30 V. After 80 minutes of CPE, NU-1000-Ru$_{high}$ (black trace) shows the generation of 1.94 μmols of O$_2$ (Figure 4.8).

With a total charge of 2.006 C having passed through the cell, a Faradaic efficiency (FE) of 37% can be calculated. The low FE is most likely due to TBAPy oxidations that occur at the applied potential as described above and clearly observed in the repetitive CVs (Figure 4.7.). A control experiment with parent NU-1000 generates a negligible amount of oxygen, manifesting the role of the Ru metallo-linker as water oxidation catalyst.

As Ru linkers in the interior of the MOF crystals can only be oxidized in a TBAPy-mediated mechanism, an independent determination of electroactive Ru sites in NU-1000-Ru$_{high}$ is not possible. Assuming that catalysis occurs only at the near-surface Ru sites that also give rise to the CV response in Figure 4.6. C, a TON of 44600 can be calculated. It is however important to note that this number should only be seen as an upper limit, as most likely also Ru linkers in the interior of the MOF crystals contribute to catalysis, which would give rise to significantly lower TONs.
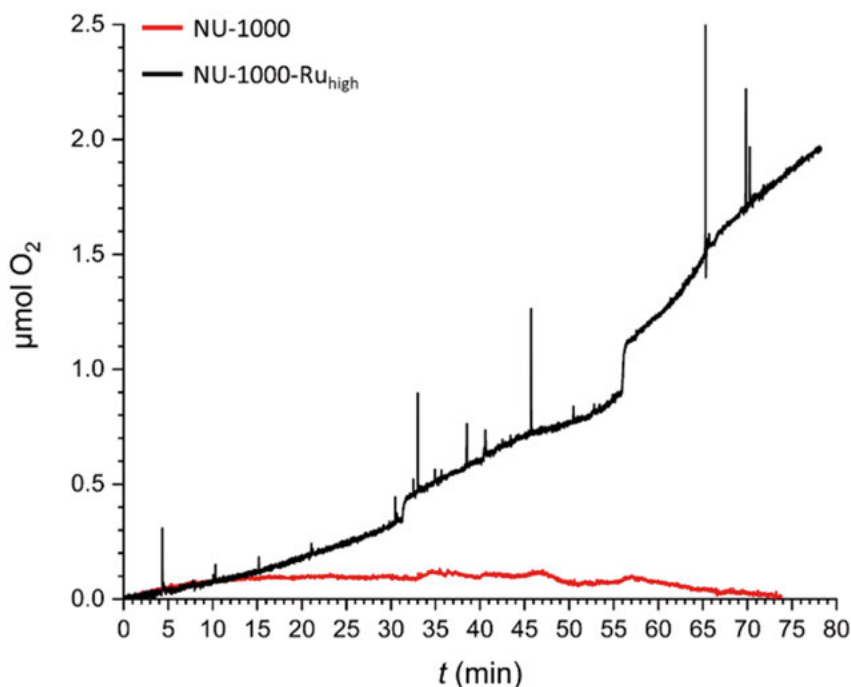
Figure 4.8 *Controlled potential electrolysis (CPE) coupled to oxygen evolution measurement of NU-1000 (red) and NU-1000-Ru$_{high}$ (black). Oxygen evolution vs time traces were recorded at an applied potential of 1.3 V vs. NHE in a 0.1 M phosphate buffer (pH 7), monitored with a gas phase Clark electrode. A Faradaic efficiency of 37 % was calculated at 80 minutes for NU-1000-Ru$_{high}$. Reprinted with permission from the Royal Society of Chemistry. A. Howe et al / Mater. Adv., **2022**, 3, 4227 - 4234.*

4.6 Conclusions & Outlook from Papers I and II.

Chapters 3 and 4 contain the results of our attempts to incorporate to incorporate water oxidation catalysts of the $[Ru^{II}(tda)(py)_2]$ family into UiO-66 and NU-1000 type metal-organic frameworks.

Three synthetic approaches for the incorporation of a catalytic metallo linker were considered, namely the direct synthesis, co-synthesis with linkers of similar size and geometry. As the project aimed at the preparation of UiO-type MOFs, the diatropic $[Ru^{II}(tda)(ina)_2]$ linker was used, while for the NU-1000-type, the tetratopic $[Ru^{II}(tda)(Py(PhCOOH)_2)_2]$ linker was used.

For the UiO-type MOF work in paper I, direct methods yielded amorphous materials, that most likely result from SBU ligation by the equatorial tda carboxylate in a random fashion. Mixed linker MOF synthesis with the ditopic $[Ru^{II}(tda)(ina)_2]$ and edba, also produced amorphous materials. The Ru linker could however be introduced into the MOF, via a post-synthetic approach.

Interestingly, this MOF can be prepared in two distinct morphologies, controlled by small variations in the linker : SBU ratio during the synthesis. Despite of having found viable synthetic strategies for MOF incorporation. The Ru complex did not display electrocatalytic water oxidation activity in this instance.

Subsequently, efforts to introduce $[Ru^{II}(tda)(Py(PhCOOH)_2)_2]$ into NU-1000 were carried out, as outlined in paper II. This too initially also focused on direct solvothermal methods. When using the Ru complex as the sole linker, the solvothermal synthesis resulted in amorphous materials, mirroring the outcome for the ditopic $[Ru^{II}(tda)(ina)_2]$ attempts described in paper I. However, in contrast to the co-synthesis strategies outlined in paper I, combining tetratopic $[Ru^{II}(tda)(Py(PhCOOH)_2)_2]$ with the tetratropic H$_4$TBAPy pyrene-based co-linker in solvothermal syntheses produced a series of crystalline materials with variated Ru loading.

Attempts to enhance the incorporation yield by increasing the $[Ru^{II}(tda)(py(PhCOOH)_2)_2]$ content during the synthesis resulted in MOFs of smaller crystal size and poorer quality, with Ru ratios above a certain threshold producing only amorphous materials. Cyclic voltammograms of the NU-1000-Ru MOFs exhibited no characteristic Ru(tda)-based features, which indicates that the density of the Ru centres is below the percolation threshold for redox hopping – a phenomenon with precedent in the literature.[86, 118, 168] Overall, chapters 3 and 4 describes two successfully solved synthetic problems for the immobilisation of $[Ru^{II}(tda)(py)_2]$ derivatives into UiO and NU-1000 type topologies.

For the future development of this project, it has to be ensured that catalyst activation by bulk electrolysis of the MOF can be conducted. Preliminary experiments show that this is challenging. A promising approach could be established in the Ru-doped NU-1000 though, in which pyrenes can be oxidised at high electrochemical potential. The oxidised pyrene linkers providing sufficient driving force for the oxidation of the $[Ru^{II}(tda)(Py(PhCOOH)_2)_2]$ linkers, despite their low abundance in the material which leads to very slow Ru-to-Ru hole transport. This mediated hole transport to all catalyst through the pyrene linker is an elegant mechanism. Which may permit catalyst activation of all Ru catalysts for water oxidation, event those that are remote from the MOF surface.

5 Synthesis of a Metal-Organic Framework Formed from Molecular Ruthenium-based Water Oxidation Catalyst as the Sole Linker Unit (Paper III)

In this chapter, a new zirconium-based MOF is prepared from the ruthenium complex $[Ru^{II}(bda)(py)_2]$ (bda = 2,2-bipyridine-6,6-dicarboxylic acid, $Py(PhCOOH)_2$ = (4,4'-(pyridine-3,5-diyl)dibenzoic acid)) as the only linker unit. Structural and functional characterisation of the complex, the MOF in its bulk form and as a surface-mounted metal-organic framework (SURMOF) was carried out. The electrochemical properties and charge transport characteristics of these materials are assessed. The work in this chapter is the first example of a molecular ruthenium complex being successfully incorporated into a MOF as a sole integral linker unit.

5.1 Introduction

As discussed in the previous two chapters, carboxylates at the equatorial tda ligand of the Ru metallo-linker that are not permanently coordinated to the Ru cation may disturb solvothermal MOF growth. To counteract this potential problem, a Ru-based water oxidation catalyst linker based on 2,2-bipyridine-6,6-dicarboxylic acid (bda) was envisaged as metallo linker. For MOF incorporation, anchoring groups for SBU coordination had to be installed, and axial ligands similar to the ones in chapter 4 were chosen for this purpose.

Solvothermal synthesis of MOFs that exclusively consist of water oxidation catalysts as metallo linkers is desirable due to higher loadings of catalytic sites that could give rise to high current densities in electrochemical experiments. With the catalysts being integral to the linker, the void in the MOF structure is available for ion, substrate and product transport.[169] Reports of direct synthesis of electrocatalytic MOFs have been limited to porphyrins as for example in PCN-222,[170] and other planer frameworks. Herein, we report the creation a MOF that is built entirely from the octahedral $[Ru^{II}(2,2'$-bipyridine-6,6'-dicarboxylato)(4,4'-(pyridine-3,5-diyl)dibenzoic acid)_2]$ (abbreviated as **II**) which acts as the sole linker moiety in the framework.

5.2 Preparation of the Metallo-linkers

The metallo-linker was prepared from 2,2-bipyridine-6,6-dicarboxylic acid and Ru(dmso)$_4$Cl$_2$ in the presence of Et$_3$N, followed by the addition of the axial ligand. Progress of the reaction was monitored by cyclic voltammetry and the complex purified by multiple washing and extraction steps. Pure [Ru^{III}(2,2′-bipyridine-6,6′-dicarboxylato)(4,4'-(pyridine-3,5-diyl)dibenzoic acid)$_2$] (**II**) was obtained in 32 % yield (Figure 5.1.).
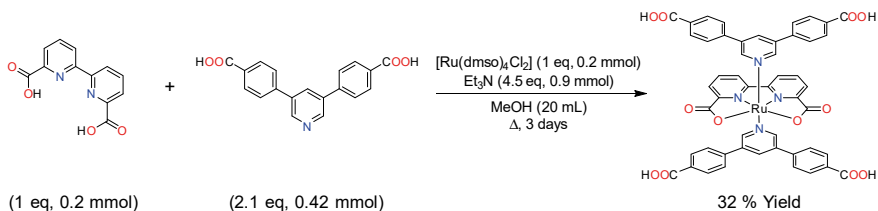
Figure 5.1. *Synthetic scheme for the preperation of [Ru^{II}(bda)(Py(PhCOOH)$_2$)] (**II**).*

The ^{1}H NMR spectrum of **II** was recorded in conjunction with a reducing agent to reduce the paramagnetic Ru$^{(III)}$ centre into the diamagnetic Ru$^{(II)}$ species that is observable in the NMR spectroscopy. The ^{1}H NMR spectrum of **II** in Figure 5.2. shows the expected peaks in the aromatic region that arise from the equatorial bda and the axial pyridine-derived ligands.
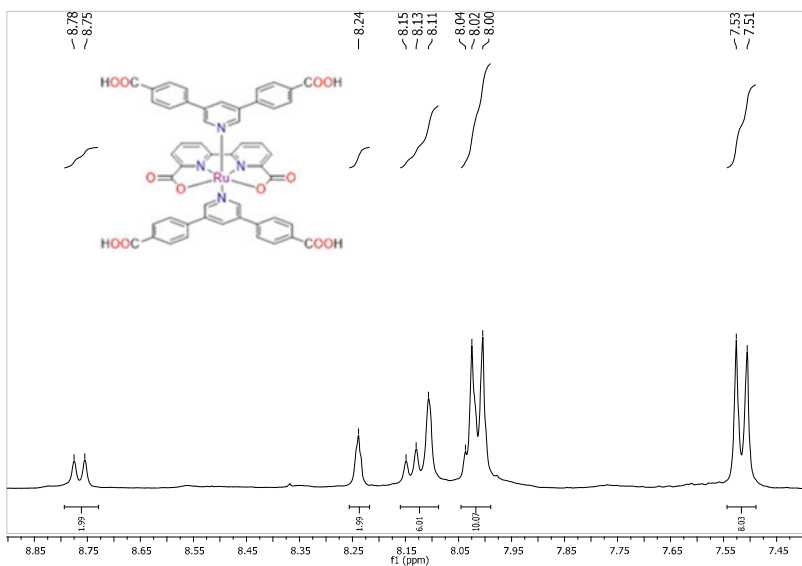
Figure 5.2. *^{1}H NMR spectrum of **II** in MeOD with 20 µL of triethylamine and 20 mg of sodium ascorbate (400 MHz, MeOD).*

5.3 Electrochemical Characterisation of the Metallo-linker

Cyclic voltammetry (CV), differential pulse voltammetry (DPV) and chrono-amperometry (CPE) measurements of the linker were performed in a single compartment cell. The electrochemical behaviour of the linker was studied under aqueous conditions as the reactivity and performance of the Ru-bda family of water oxidation catalysts can be highly sensitive to minor changes in solvent composition.[171]

Complex **II** was first investigated in 0.1 M TFA solution to which trifluoro-ethanol (TFE) was added to improve solubility of the complex. As seen in Figure 5.3., the CV of **II** shows redox waves for the $Ru^{(III/II)}$, $Ru^{(IV/III)}$ and $Ru^{(V/IV)}$ couples at 0.77 V, 1.09 V, and 1.3 V, respectively, which is in a similar range to values already reported in the literature.

Metallo-linker **II** lacks stability in aqueous solution and exposure of solutions of the complex to air overnight results in a dramatic colour change from red to green. A possible explanation for this phenomena is that the complex oxidises in the presence of air and forms a Ru–O–Ru–O–Ru metal-oxide-chain motif, which has been observed in previous studies.[172]
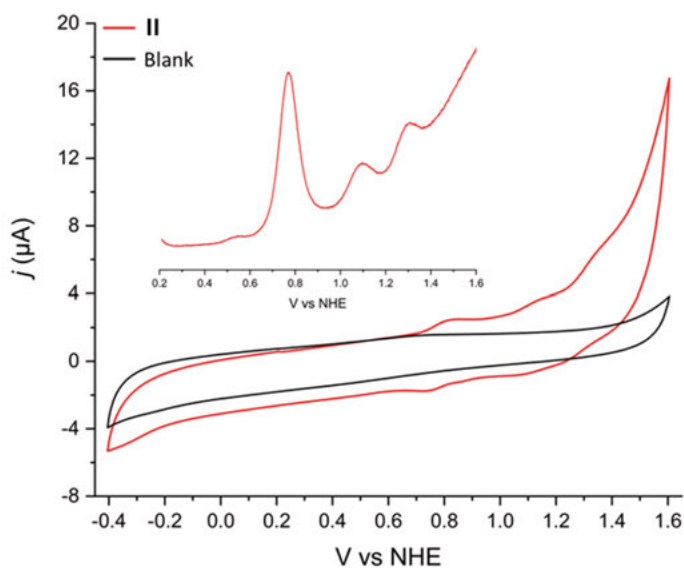
Figure 5.3. *CV of **II** (in red) and background CV (in black) in 0.1 M in 0.1 M trifluoroacetic acid in the presence of TFE (100 mV/s-1). Insert shows the DPV under identical conditions.*

The electrochemical properties of **II** were further investigated in acidic, neutral and basic aqueous solutions. In aqueous phosphate buffer solutions at pH 7.0 (Figure 5.4.), the redox potentials are shifted and only two redox couples can be observed at 0.67 V and 1.1 V that are assigned to the Ru$^{(III/II)}$ and Ru$^{(IV/III)}$ couple, respectively. Following these waves, the catalytic onset and associated rapid increase in current density is observed. The increase in current density at the water oxidation potential is pH dependent, and increases with increasing OH$^-$ concentrations. At acidic pH values, the current increase is diminished.[173]
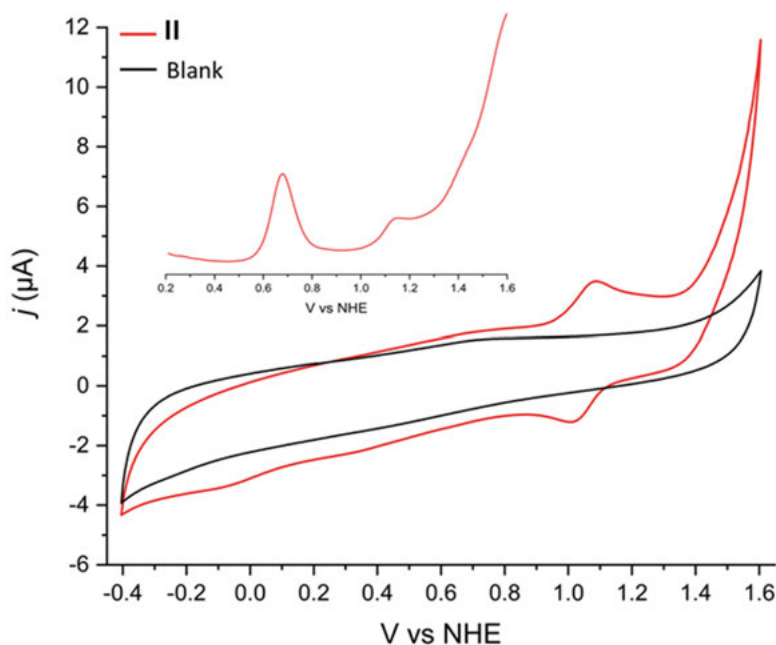
Figure 5.4. CV and DPV of **II** in 0.1 M pH 7 phosphate buffer solution. Black trace (1 mM of Ru(bda)(Py(PhCOOH)$_2$)) and blank glassy carbon electrode (red trace). (v = 100 mV/s).

5.4 Target MOF Preparation in Bulk

Complex **II** was used as a metallo-linker together with the SBU precursor ZrOCl$_2$.8H$_2$O in a solvothermal syntheses to form a new MOF (**III**). Different synthesis conditions were screened (amount and type of modulator, reaction time and temperature), some of which are summarized in Table 2.
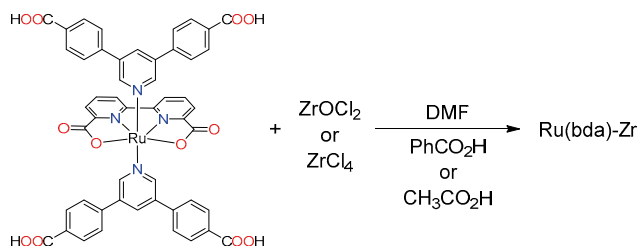
*Table 2. Synthesis conditions for the synthesis of MOF **III***

Ru(bda)	ZrOCl$_2$	ZrCl$_4$	PhCO$_2$H	CH$_3$CO$_2$H	V DMF	Temp.	Time
20 mg	13 mg	-	750 mg	-	7.0 mL	80 °C	5 days
20 mg	-	9.4 mg	750 mg	-	7.0 mL	80 °C	5 days
20 mg	-	9.4 mg	1.0 g	-	7.0 mL	80 °C	5 days
20 mg	13 mg	-	-	525 µL	7.0 mL	65 °C	5 days
20 mg	13 mg	-	-	700 µL	7.0 mL	65 °C	5 days
20 mg	13 mg	-	-	525 µL	7.0 mL	80 °C	5 days

.The bulk powder MOFs that were obtained from the different solvothermal syntheses were characterized by powder x-ray diffraction (PXRD, Figure 5.5.). With benzoic acid as modulator (72 eq), three clearly visible reflections are visible in the PXRD at 2θ = 5°, 7.1° and 10°. Unless stated otherwise, it is this material that has been used in the subsequent sections. In an effort to improve the crystal quality of **III**, other modulators were tested, including experiments with 150 equivalents of acetic acid and formic acid.

The sample synthesised with acetic acid as a modulator showed multiple reflections at 2θ = 5.25°, 7.05°, 8.58°, 9.01°, 9.18°, 9.38°, 9.65°, 10.34°, 11.30°, 13.47°, 13.88°. A different pattern of reflections emerged at 2θ = 6.97°, 8.19°, 8.62°, 8.97°, 9.48°, 9.93°, 10.32°, 13.92° when formic acid was used as

modulator, pointing towards the formation of MOFs with different topologies. Unfortunately, despite of many attempts, crystals of sufficient size and crystallinity for structure determination by X-ray crystallography could not be obtained. Instead, materials of the highest crystallinity are currently being investigated by electron diffraction for further characterisation.

The obtained materials were further evaluated by SEM, which shows octahedral crystals which are approximately 375 nm in length (see Figure 5.6.). Furthermore, EDX of the crystals show an even distribution of the complex throughout the crystals (See ESI). ICP-OES of six different batches of MOF gave rather similar Ru : Zr atomic ratio of 0.42±0.05 (see ESI). This ratio is in between the expected ratios of a 12-coordinate Zr_6-cluster SBU MOF such as UiO-66 and an 8-coordinated Zr_6-cluster SBU MOF such as NU-1000. The latter, consisting also of tetratopic linker units (see section 4), exhibits a linker : Zr ratio of 0.33.
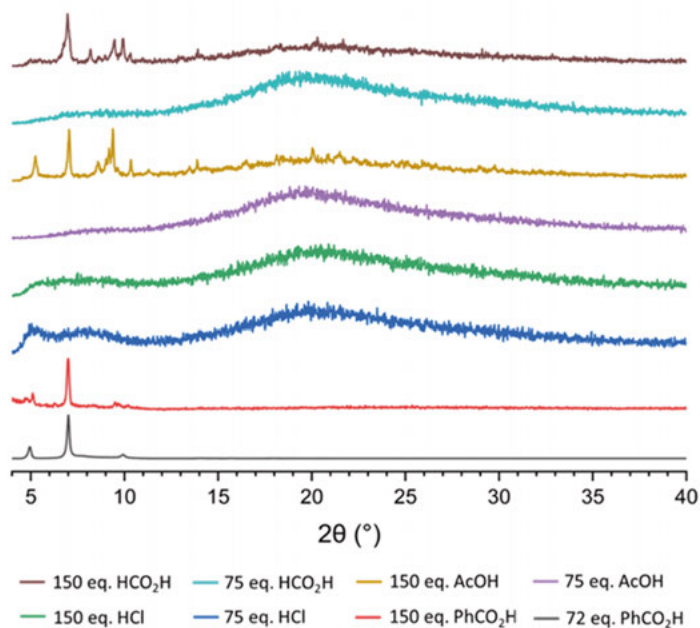
Figure 5.5. *Powder X-Ray Diffraction (PXRD) of **III**, synthesised using different modulators. 72 eq PhCO₂H (black trace), 150 eq PhCO₂H (red trace), 75 eq HCl (blue trace), 150 eq HCl (green trace), 75 eq AcOH (purple trace), 150 eq AcOH (tan trace), 75 eq HCO₂H (turquoise trace) and 150 eq HCO₂H (brown trace).*
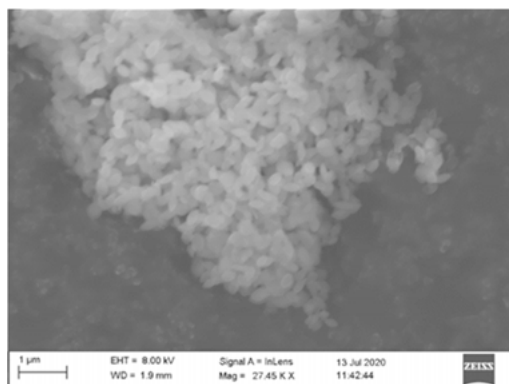
Figure 5.6. *Scanning Electron Microscope (SEM) images of **III**. The SEM image show oval particles which have an average size of approximately 375 nm.*

The absorption isotherm of **III** synthesised with 72 equivalents of benzoic acid is shown in Figure 5.7., and exhibits a normal type II isotherm behaviour. The Brunauer-Emmett-Teller (BET) surface area, showed a low surface area of 33.6 cm^3/g. This may be a result of limited crystallinity of the sample, but also due to collapse of the MOF structure during the washing stages.
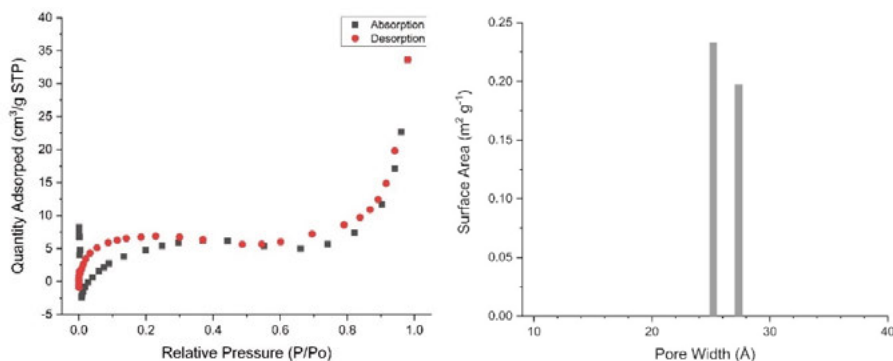
Figure 5.7. *Left, isotherm plot of **III**. Obtained from 34.6 mg of material. Adsorptive N$_2$ isotherm was recorded at 77 K. Prior to measurement, materials were activated under dynamic vacuum (1 × 10^{-4} Pa) at 80°C for 18 hours. Right, Incremental surface area vs pore size plot of **III** obtained from 34.6 mg of material.*

5.5 Electrochemical Analysis of MOF **III**

III was suspended with MWCNT and drop-casted onto glassy carbon electrodes for electrochemical characterization. CVs of immobilised **III** in 0.1 M pH 7 phosphate buffer (phbs) revealed redox processes at 0.62 V and 0.77 V which are assigned to the Ru$^{(III/II)}$ and Ru$^{(IV/III)}$ couples, respectively (Figure

5.8.). These values are cathodically shifted compared to those of the homogenous linker (0.67 V and 1.1 V) at the same pH, presumably a result of the different micro-environment around the linker when incorporated in the MOF. Multiple scan experiments lead to an anodic shift of the oxidation potentials to 0.67 V (Ru$^{(III/II)}$) and 0.84 V (Ru$^{(IV/III)}$), thus closer to those of the homogeneous linker. While such effects do not have precedence in the literature, the shift may be due to pH changes in proximity of the catalyst linker or changes at non-permanently occupied coordination sites at the SBU. The peak-to-peak separation of the waves is also increased at the higher scans, indicative of slow interfacial electron transfer or kinetically limited electron transport in the MOF crystals.
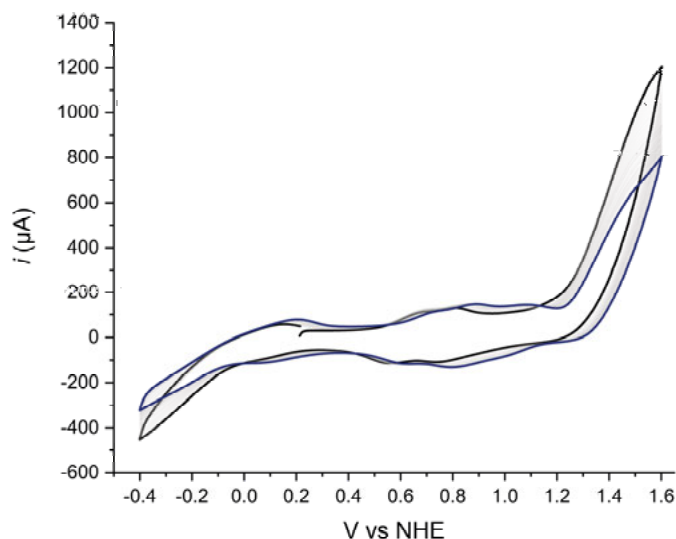
Figure 5.8. *CV of* ***III****, drop casted with multi-wall carbon nanotubes (MWCT) on a GC electrode (0.071 cm^2), conducted in 0.1 M pH 7 phbs as a supporting electrolyte in water. Initial scan (black trace), scans 2 – 49 (grey trace) 50th scan (blue scan).*

5.6 SURMOF Growth

In order to increase the structural stability of the MOF substrate interface, to obtain more coherent films, and to increase interfacial charge transfer kinetics, **III** was grown as a surface-mounted metal-organic framework (SURMOF). The preparation of such SURMOFs usually involve exposing a flat solid substrate, such as FTO, ITO, or gold to a solution of MOF precursors, followed by solvothermal synthesis to form a film on the surface of the substrate. Alternatively, the can be performed in a step-by-step fashion and carried out sequentially by exposing the substrate to dilute-solutions of metal salt (for SBU formation) and linkers in an alternating fashion, normally with washing steps

in between. This procedure allows the film to be built one layer at a time, allowing the film thickness to be controlled by the number of growth cycles. This growth method is otherwise known as liquid-phase epitaxy.[174, 175]

Another methodology to grow oriented SURMOFs is the vapour assisted conversion (VAC). This method is based on the conversion of a droplet of a MOF precursors solution into a crystalline film by exposure to a vapour of specific composition at moderate temperatures. Using this method, the thickness of the MOF film can be controlled via the droplet volume on the surface of substrate (Figure 5.9.).[176]
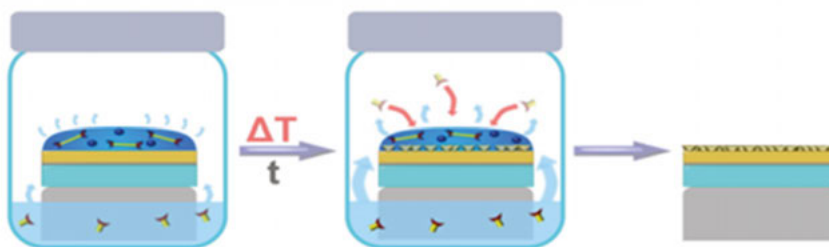
Figure 5.9. *Schematic representation of the vapor-assisted conversion process for the fabrication of oriented MOF films of controlled thickness. This image was adapted from an image reprinted with permission from the Journal of the American Chemical Society. E. Virmani et al / J. Am. Chem. Soc. **2018**, 140, 4812 − 4819.*

5.6.1 Characterisation of SURMOF on Au

While the solvothermal growth of **III** on FTO and ITO substrates was not successful, **III** could be grown on a bare gold surface (**III**@Au) by VAC.[176] Using this method, continuous films with high coverage were obtained. The VAC MOF synthesis was tested using different temperatures and film formation times, all of which provided excellent surface coverage, with the reaction time not affecting the overall quality of the film to any significant degree.

The results of changing the conditions for **III**@Au formation were examined using XRD and SEM. In all VAC examples, a prominent peak can be observed in the PXRD at $2\theta = 3.3°$, with the PXRD pattern of the Au substrate being suppressed in all instances. Curiously, reflection at 3.3° is not observed in the PXRDs of any of the bulk materials, the reason for which is still under investigation. One explanation could be that MOF III is grown in a specific orientation that gives rise to the observed reflection at 3.3° and disfavours the reflections observed for the randomly orientated power of the bulk material (Figure 5.10.).

Analysis of the **III**@Au plates by SEM revealed films with good coverage and an average film thickness of around 150-170 nm (Figure 5.11). Cross-section imaging of the film shows crystals that each possess an octahedral morphology measuring approximately 250 to 260 nm in length. Energy dispersive X-ray spectroscopy (EDX) of the thin film yielded a Zr^6:Ru ratio of 2:3. The atomic concentration of the sample also shows that the Zr^6:Ru ratio on the surface of the films to be (Zr/Ru): 698.477 : 1139.714, resulting in a (Zr/Ru) 0.38 : 0.62 ratio in the bulk sample. When comparing the XPS of the different SURMOF films on the gold substrates, they display an identical XPS spectra, with Zr : Ru ratios of 0.38 : 0.62, which indicates that there is little variation in surface composition of the film, regardless whether the MOF synthesis was done in bulk or on a surface. (see ESI paper **III**).

The stability of **III**@Au upon an applied oxidative potential, and its electrochemical properties were assessed by CV in aqueous 0.5 M KNO_3 solution as supporting electrolyte. A 30-scan experiment showed only a minor decrease in current density, suggesting a stable construct (see Figure 5.12. right). Further experiments in phbs electrolyte solutions at different pH values confirmed this initial observation, and the films appeared stable at pH 6, 7 and 8, without signs of delamination.
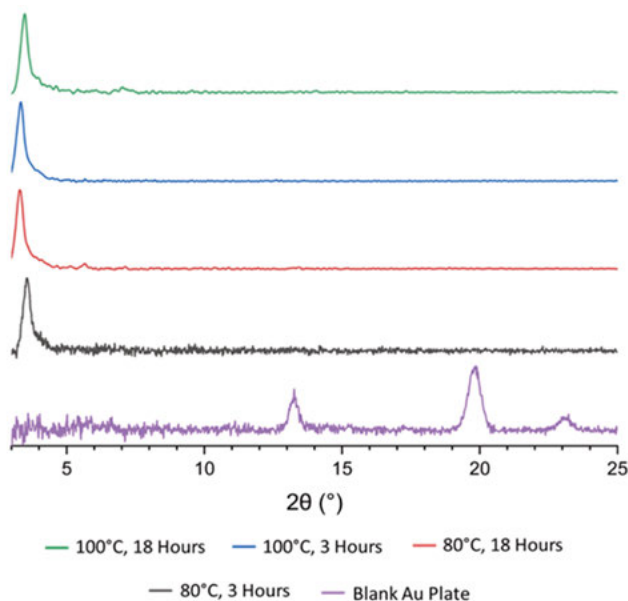
*Figure 5.10. XRD of **III**@Au, (2θ) from different VAC preparations: 80°C for 3 hours (black trace), 80°C for 18 hours (red trace), 100°C for 3 hours (blue trace) and 100°C for 18 hours (green trace). All materials exhibit a major diffraction at 3.3 (2θ) and a minor one at 5.7 (2θ) in the red and green traces. Blank Au substrate (purple) exhibits reflections at 13.3, 19.9 and 23.2 (2θ). The gold substrate is not visible on the MOF films due to complete coverage of the substrate.*
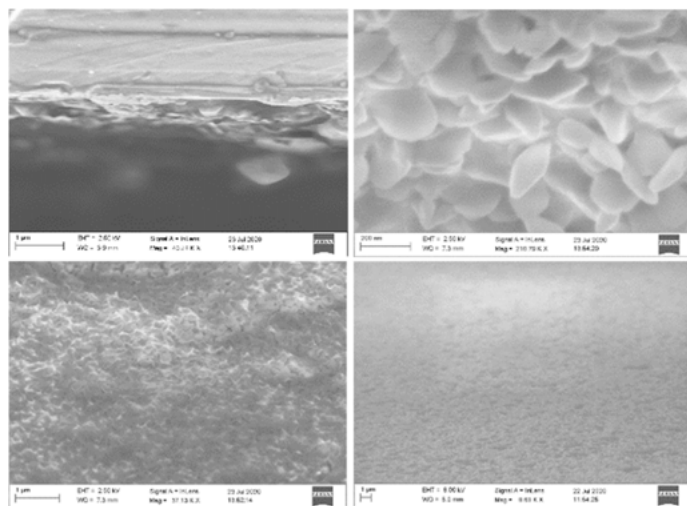
Figure 5.11. *SEM images of **III**@Au, with film thicknesses of around 150 – 170 nm. Each sample had complete surface coverage on the film, with each particle being approximately 250 – 260 nm in length.*

The CVs showed a Ru$^{(IV/III)}$ couple at a formal E$_{1/2}$ of 1.09 V, albeit with a large peak-to-peak separation for this redox couple of 443 mV. A blank gold electrode showed redox couples at E$_{1/2}$ = 0.57 V and E$_{1/2}$ = 1.14 V, which demonstrates that these MOF films are distinct from the electrochemical redox couples produced by the gold substrate (see Figure 5.12. left). As the Zr$^{(IV)}$ centres have a d$_0$ electron configuration and are redox-inactive, the Faradaic response in the CV's can only be attributed to the redox active linker complex.

The integrity of the film as well as the topology of the MOF is maintained during the CV experiments, as evidenced by unchanged PXRD patterns before and after CV cycling. SEM images taken after CV measurement also show that the integrity of the MOF film remains largely intact under these conditions, which demonstrates the robust nature of these films as the MOF is strongly adhered to the surface. Replacing the **III**@Au working electrode with a glassy carbon electrode gives rise to CVs without any Faradaic features.

This rinse test further confirms the stability of the MOF, and the absence of catalyst leaching into the electrolyte. In order to have a direct comparison between other Ru-bda type of complexes in the literature, the electrochemical characterisation was repeated in 0.1 M TFA solution. A small initial loss of current is observed, but no catalytic wave is observed under these conditions (Figure 5.13).
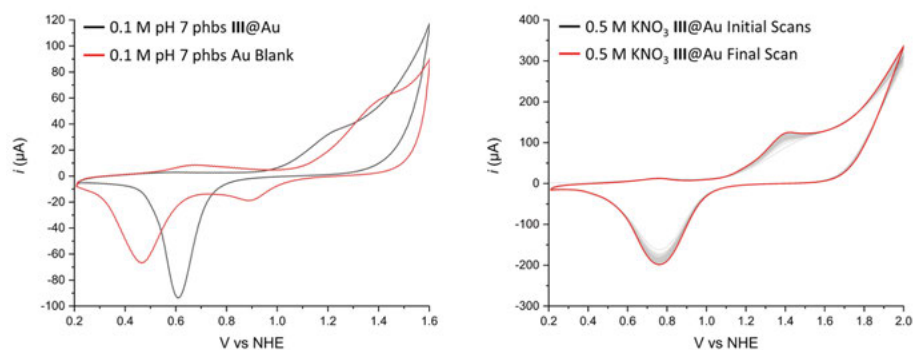
Figure 5.12. *Left, CV comparison between **III**@Au vs blank Au bolt. Right, Stability testing of the **III**@Au conducted in 0.5 M pH 7 phbs as a supporting electrolyte in water. The films were evaluated over 30 scans in a single compartment, three-electrode setup. 0.5cm² the **III**@Au working electrode, GC counter electrode and Ag/AgCl reference.*

These initial scans show a $Ru^{(III/II)}$ and a $Ru^{(IV/III)}$ couple at 1.13 V and 1.28 V, respectively, with peak-to-peak separation of 453 mV and 339 mV respectively. These values are significantly shifted compared to those of the homogeneous complex, which has redox couples of $Ru^{(III/II)} = 0.79$ V and $Ru^{(IV/III)} = 1.1$ V under these conditions. Again, we ascribe these variations to altered environments around the catalysts linker in the MOF compared to the situation in solution phase. CVs at various scan rates show that the anodic response and the cathodic response is proportional to the square root of the scan rate (see ESI of paper **III**). SEM images taken after CV measurement show that the integrity of the MOF film remains largely intact, also when the CVs are conducted in 0.1 M TFA solution, with only small amounts of weakly bound particles detached from the surface.
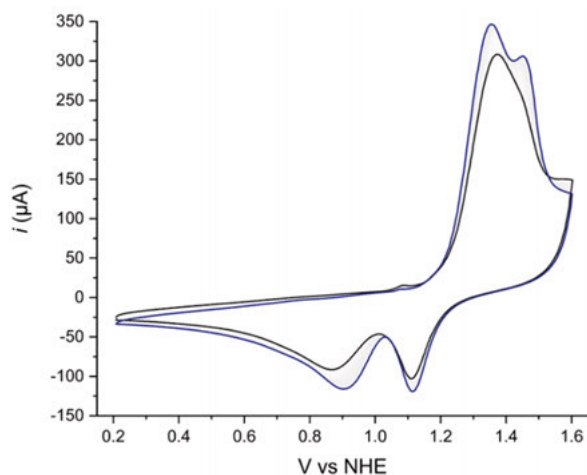
Figure 5.13. *CVs of **III**@Au thin-film (30 scans) in 0.1 M trifluoroacetic acid at 100 mV/s⁻¹.*

5.7 Diazonium Grafted SURMOF

To exclude the possibility of gold interfering in the water oxidation, **III** was also grown on glassy carbon (GC) electrodes. As the direct growth of the framework on the bare glassy carbon substrate was not possible, a grafting procedure was explored first to functionalize the surface of the GC electrodes with phenylcarboxylates. The latter were envisaged to act as nucleation points for MOF growth. The carboxylates were introduced by a diazonium grafting strategy, using (4-carboxyphenyl)diazonium tetrafluoro borate as the starting material. Upon applied cathodic potentials, the diazonium salt is reduced and forms phenyl radical species which then react with the GC substrate to form a covalent bond (see Figure 5.14).

Two CV scans were run from -0.4 V to -1.3 V, resulting in a broad cathodic wave centred around -1.06 V during the first cycle. Following multiple washing steps, the carboxylate-functionalized electrodes were used for the MOF synthesis, using the VAC method. The resulting MOF film was analysed by SEM and PXRD which confirmed the presence of the MOF film on the GC surface. The SEM shows particles of around 450 - 460 nm on the surface of a GC plate (Figure 5.15.). While the particles are thus somewhat larger than those in the **III**@Au samples, the PXRD exhibits a reflection around 3.29 – 3.64, which is comparable to that observed in the **III**@Au (Figure 5.16). The PXRD of **III**@GC is however rather broad, the reason for which is currently unclear. As expected, the blank GC electrode gives a featureless XRD, proving that the observed reflection arises from the presence of the MOF.
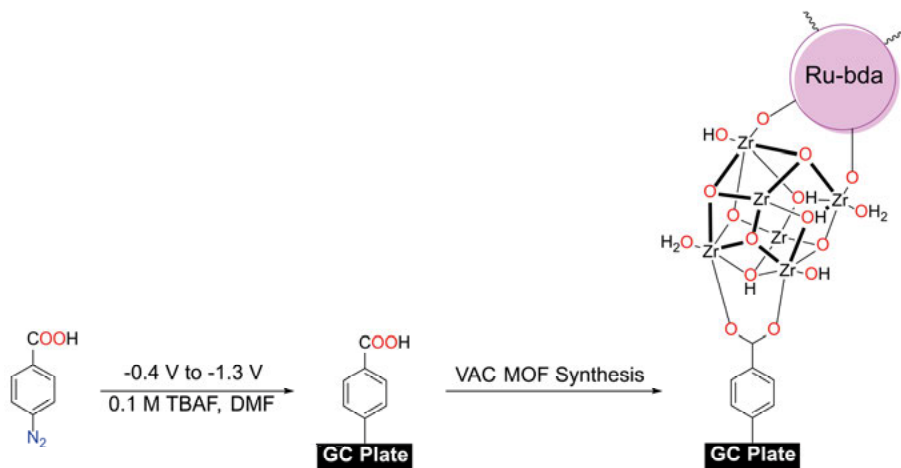
Figure 5.14. *Scheme for the fabrication of diazonium modified glassy carbon electrode.*
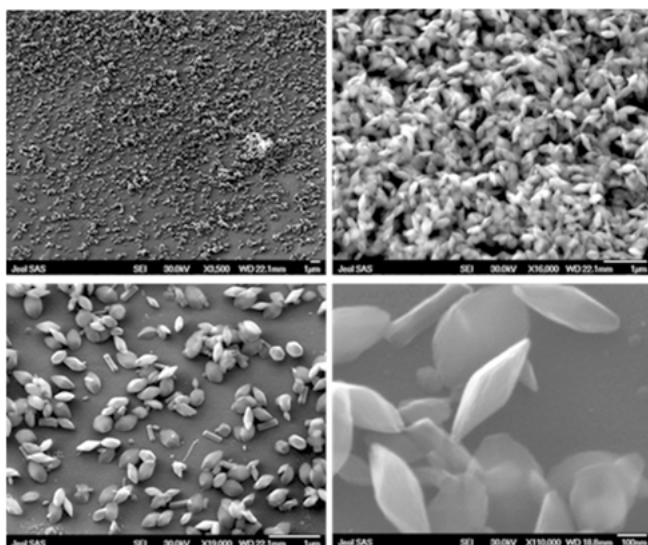
*Figure 5.15. Representative SEM images of **III** on the surface of a GC plate, with a particle size of 450 - 460 nm.*
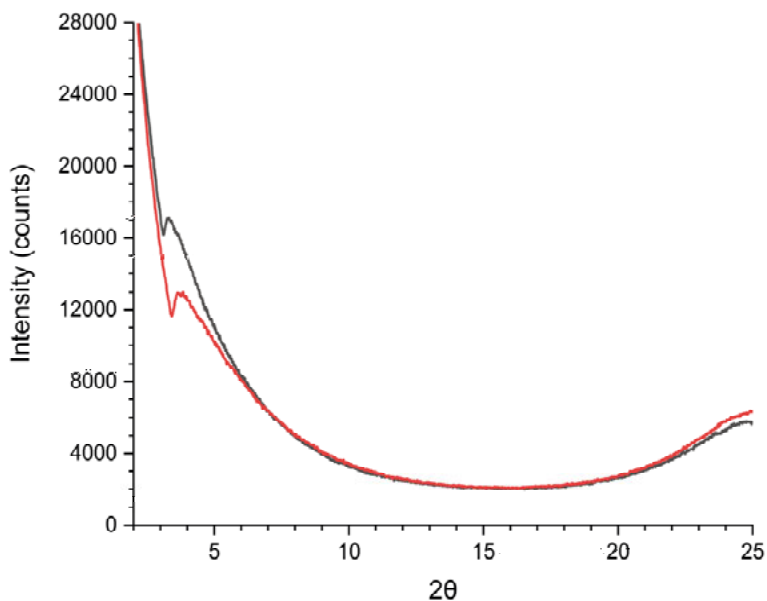
*Figure 5.16. Powder X-Ray diffraction (PXRD) of **III@GC**, grown via vapour assisted conversion (VAC) method on a benzoic acid functionalised GC substrate. diazonium grafting of benzoic acid on the surface of glassy carbon at a 2000 mV/s[-1] (2 scans) (black trace). **III@GC** 2000 mV/s[-1] (1.5 scan) thin film formation carried out at 100°C for three hours (red trace).*

The **III**@GC electrode were examined by CV in a 0.1 M phosphate buffer solution at a scan range of -0.2 V to 1.6 V at 100 mV/s[-1]. Upon increased

number of scans, a gradual increase in current density at the water oxidizing potential can be observed, which can only be attributed to the MOF film on the surface. (Figure. 5.17.).

Unfortunately, clearly discernible waves that could be attributed to the Ru metallo-linker could not be observed at this scan rate. Increasing the scan rates up to 1000 mV/s resulted in the appearance of two waves, albeit hardly visible. The potentials of these two waves at 0.47 V and 0.69 V were assigned to the $Ru^{(III/II)}$ and $Ru^{(IV/III)}$ couples. The fact that these waves are more apparent at faster scan rates can be due to generally slow electron transport through the framework that gives rise to the effect that Faradaic processes are "smeared out" during the timescale of slow scan CV experiments.
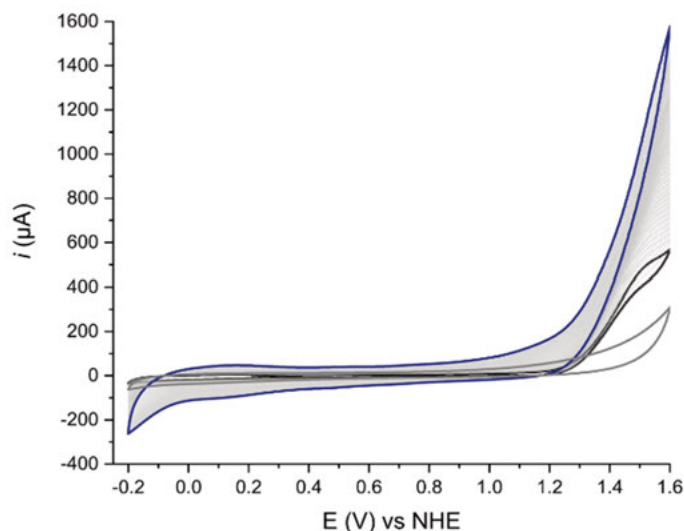
Figure 5.17. *CVs of **III**@GC: 50 scans at 0.1 M phbs at 100 mV/s⁻¹. Initial scan (black trace), scans 2 to 49 (light grey), 50ᵗʰ scan (blue trace).*

The capacity of **III**@GC as catalysts material for the electrochemical water oxidation reaction was evaluated in a CPE experiment in a gas-tight two com-partment electrochemical cell. A Clarke-type electrode was placed into the working compartment in order to measure the generation of oxygen and cal-culate the Faradaic efficiency of the **III**@GC.

During the CPE, a potential of 1.45 V was applied for 46' minutes, while ox-ygen detection was continued for an additional 21 minutes to capture any ad-ditional oxygen in solution. After 67' minutes the generation of 0.178 μmols of O_2, can be detected. The total charge that was passed through the cell was passed is 0.1864 C, which gives rise to a Faradaic efficiency of 37% (Figure 5.18.). The low current density of around 0.14 mA/cm^{-2} under bulk electroly-sis conditions demonstrates that the conductivity of the electrode is poor,

presumably due to the diazonium grafted layer also being insulating at the applied anodic potential.
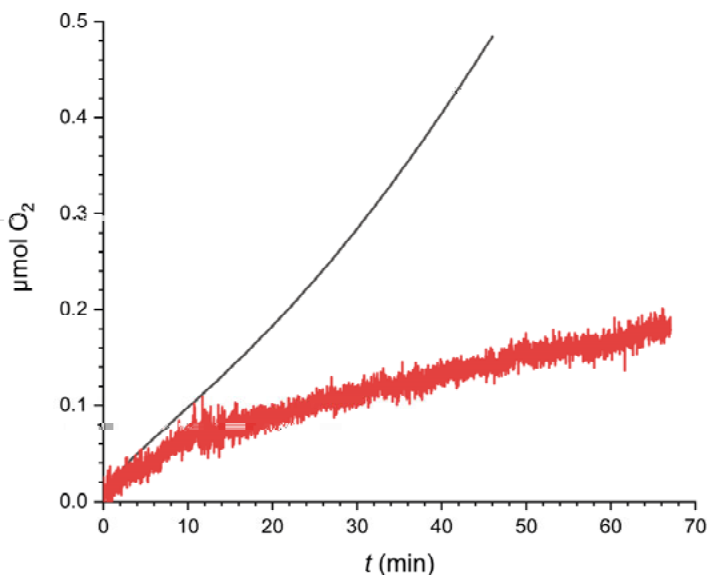
Figure 5.18. *Oxygen evolution vs time of **III**@GC, monitored with a gas phase Clark electrode. Red line corresponds to the O₂ measured from **III**@GC. Black line corresponds to the theoretical level of O₂ measured from the CPE. A Faradaic efficiency value of 37 % was calculated at 67 minutes for **III**@GC in 0.1 M phbs.*

5.8   Water Oxidation Studies of Ru-bda MOF

The performances of the homogeneous Ru complex **II** and its bulk MOF derivative **III** as water oxidation catalysts were examined in experiments with chemical oxidants. Oxygen evolution was followed by either gas chromatography or via an oxygen sensitive Clarke electrode. The durability of **II** and **III** as catalyst material was evaluated by repeated additions of 50 µL aliquots of 0.05 M cerium ammonium nitrate (CAN) solutions in 0.5 M HNO₃. In the case of **III**, each addition resulted in a marked increase in oxygen production, as detected by the Clark electrode.

The behaviour of MOF **III** in the Clark electrode is characterised by a rise in the oxygen concentration, followed by a decrease in the oxygen concentration in solution. There are a number of possible explanations for this phenomenon, but one possibility is that reactions occur at the electrode, which consume oxygen. One possibility that was explored was the oxidation of other ligands that lead to the production of carbon dioxide, but sampling of the headspace via

gas chromatography showed the absence of carbon dioxide. Therefore, other reactions must be taking place to account for the falling oxygen concentration in solution, such as the formation of peroxide, which wouldn't be detected by the Clark electrode. With the subsequent additions of CAN, another effect can be observed. This is represented by the increased gradient of loss of the oxygen concentration in solution, an effect typical of oxygen saturation in solution that results in bubble formation.

In contrast, the free linker **II** exhibits much poorer water oxidation activity (Figure 5.19). In particular, complex **II** catalyses water oxidation only after addition of the first aliquot of CAN, and seems to have largely decomposed thereafter. The experiments on the homogeneous complex **II** are important for two reasons. First, the lack of O_2 evolution after the second addition to **II** shows that CAN addition alone does not trigger O_2 evolution, and that any O_2 that is detected is obtained by a process catalysed either by **II** or **III**. Second, the reference experiments on **II** shows that MOF incorporation of the linker greatly stabilises the structural integrity of the catalyst, giving rise to considerably higher overall TONs as compared on the homogeneous reference.
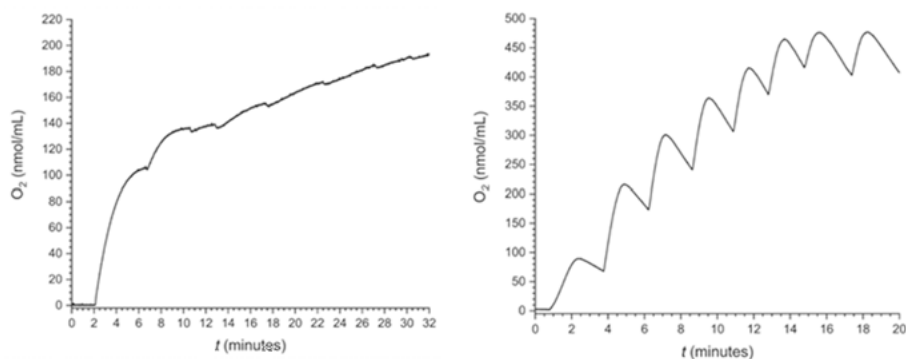
Figure 5.19. *Chemical oxidation, 50 µL of CAN (0.05 M), multiple additions. Left,* **II**. *Right,* **III**. *electrode.*

5.9 Conclusions

MOF **III** was created using linker moieties that consist entirely of [Ru^{II}(2,2′-bipyridine-6,6′-dicarboxylato)(4,4'-(pyridine-3,5-diyl)dibenzoic acid)$_2$] (**II**). While the framework exhibits a high degree of stability and exhibits no sign of degradation upon application of a high constant potential, the PXRD of the crystals in bulk doesn't provide much structural information. During the washing and drying stages, many of the smaller cavities inside the framework seem to collapse, resulting in loss of crystallinity and surface area which limits the

structural information that can be provided. Materials of the highest crystallinity are currently under investigation by electron diffraction techniques.

Somewhat unexpectedly, complex **II** does not seem to be an active water oxidation catalyst in its own right under the acidic conditions that these types of catalysts usually are tested in. One potential explanation for this lack of activity may be that the rather bulky axial ligands on complex **II** prevent the formation of the dimeric species which is the prerequisite for water oxidation by a radical coupling mechanism. Additionally, dissociation of axial ligands or the inability to engage in stabilising stacking interactions may be further factors that impart the kinetics of water oxidation catalysed by **II**. The hydrophobicity of the axial pyridine ligands does not stabilize a pre-reactive catalyst dimer which is known to improve catalytic water oxidation activity.[177]

When considering **III**, the metallo-linkers are immobilised and structurally isolated, thus unable to form a $[Ru^{IV}–\dot{O}\cdots\dot{O}–Ru^{IV}]$ seven-coordinate $Ru^{(IV)}$ dimer that is required for the canonical I2P radical coupling pathway.[25, 178] consequently, water oxidation in this case will proceeed by a water nucleophillic attack mechanism, which has precedence for the Ru-bda family of complexes under certain conditions.[179]

A notable example of a Ru-bda type of complex that operates by a water nucleophillic attack is one that is incorporated in a supramolecular macrocycle.[180] In this case, the macrocycle creates a cooperative effect between the individual Ru-bda centres and vicinal water molecules by facilitating proton abstraction of the latter.[181, 182] Another example of a Ru-bda type of complex that engages in water nucleophilic attack is in a supramolcular coordination oligomer that anchors on multiwall carbon nanotubes through CH-π interactions.[62]

In summary, even though the electrochemical water oxidation experiments on bulk MOF **III** and its different SURMOF versions were not impressive, the chemical oxidation experiments with CAN were encouraging. Compared to the homogenous **II**, MOF incorporation led to a substantial inprovement of the structural stability of the catalyst. As a consequence, multiple CAN addition cycles could be performed, and catalysis persisted for a considerable amount of time, compared to the situation in the homogenous linker where decomposition had already occurred after the first CAN addition.

6 Carbanion Ruthenium Complexes for Water Oxidation (Paper IV)

In this chapter, we present a cyclometalated carbanion ruthenium coordination oligomer based on a pentadentate ligand platform $[Ru^{III}(dpa)(py)_2]$ (dpa = ((5-methyl-1,3-phenylene)bis(pyridine-6,2-diyl))bis(phosphonic acid); (py = 4,4'-bipyridine). The complex and the corresponding coordination oligomer was synthesised and fully characterised. This molecular system was specifically designed to utilise an octahedral coordination environment around the Ru centre, with dangling phosphonate groups to modulate its electrochemical properties and second coordination sphere effects. In-depth electrochemical studies of both the complex and coordination oligomer show significant stability at high applied potentials and over a wide pH range. Most importantly, oligomeric molecular catalysts are easily anchored on graphitic surfaces, generating powerful and robust molecular anodic hybrid materials for electrocatalytic water oxidation.

6.1 Introduction

The Flexible Adaptative Multidentate Equatorial (FAME) ligand H_2tda^-, which was developed by Llobet, is utilised in the best performing WOCs known to date. The FAME ligand allows fast catalytic rates as it can adapt to the electronic demands of the multiple oxidation states of Ru, and exert beneficial hydrogen bonding interactions.[29, 183]

While previous works on water oxidation catalysts focused on carboxylate containing FAME ligands, current focus has been extended to previously unexplored phosphonates. These are of interest as the phosphonate group contains three O atoms in a tetrahedral geometry, one of which being coordinated to a metal, while the remaining oxygen atoms may be protonated or deprotonated, depending on the pH. The phosphonate group can potentially act as a proton shuttle, moving protons in and out of the catalytic site, potentially lowering activation barriers in PCET processes, particularly the O-O rate determining step.[184-187]

Building upon the success of the FAME ligand used in the Ru-tda family of water oxidation complexes, the carboxylate groups were replaced with phosphonates to synthesise 2,2′:6′,2″-terpyridine-6,6″-diphosphonic acid (H$_4$tPa), which were used to produce a new water oxidation complex. The diphosphonate ligand possesses the flexibility to coordinate and decoordinate from the metal centre, to influence second coordination sphere effects, and to promote remote PCET processes.[187] This strategy of substituting carboxylate groups with phosphonates does improve the kinetic and catalytic properties. However, it does not significantly reduce the potential of the Ru$^{(V)}$=O formation, the species responsible to trigger the water oxidation reaction.

An alternative strategy to overcome the high kinetic barrier is through the introduction of higher electron density at the equatorial ligand to lower the oxidation potentials of the complex. This reasoning motivates the study of carbanion ruthenium complexes for water oxidation, as it was postulated that complexes that contain a negatively charged ligands stabilise higher oxidation states due to strong σ-bond donation through the metal-carbon bond. Such complexes were previously synthesised and studied by Vereshchuk.[188]

The electrochemical analysis of these carbanion complexes showed a cathodic shift of the redox potentials up to 0.73 V upon coordination of the π-extended carbanionic donor sets as compared to the related [Ru^{II}(tda)(py)$_2$] and [Ru^{II}(H$_2$tPa)(py)$_2$] complexes. The replacement of one pyridine in the terpyridine by a phenyl group promotes the formation of a stable cyclometalated ring and renders the resulting ruthenium complexes inert and stable, but at the expense that it hinders the formation of the highly oxidised state Ru$^{(V)}$=O state. Despite the unsuccessful attempt at obtaining water oxidation catalysts using the [Ru^{III}(Xpda)(py)$_2$] motif factors that influence the electronic properties of the complexes such as pK_a and redox potentials were uncovered. Most importantly, the idea to decrease the overpotential for catalysis by cyclometallation persisted.

Another interesting possibility to lower the activation barriers and to stabilise intermediates, is to use supramolecular interactions, which has been reported for the [Ru^{II}(tda)(py)$_2$] family of complexes.[61] One pertinent example is the case of Ru-tda type coordination oligomers, other neighbouring oligomer strands interact through hydrogen bonding with water molecules. As a result the strength of interactions between the intramolecular carboxylate coordination and the Ru–aqua formation that is responsible for the activity of the complex is altered. These strategies were applied in this work, and allowed an otherwise stable, and inert ruthenium complex to be integrated into a coordination oligomer which could be activated for molecular water oxidation catalysis.

6.2 Synthesis

The FAME ligand was synthesised in a five-step process, starting from 2-bro-mopyridine, which undergoes a lithium-halogen exchange and transmeta-lation with tributyltin chloride to form the Stille reagent 2-(tribu-tylstannyl)pyridine. The latter compound undergoes a Stille cross-coupling with 3,5-dibromotoluene to yield 2,2'-(5-methyl-1,3-phenylene)dipyridine. An N-oxidation strategy is used to carry out a Michaelis-Arbuzov reaction, in order to synthesise the phosphine diethylester, followed by removal of the es-ter using bromotrimethyl silane to yield ((5-methyl-1,3-phenylene)bis(pyri-dine-6,2-diyl))bis(phosphonic acid), which is used as the equatorial ligand (Figure 6.1.).
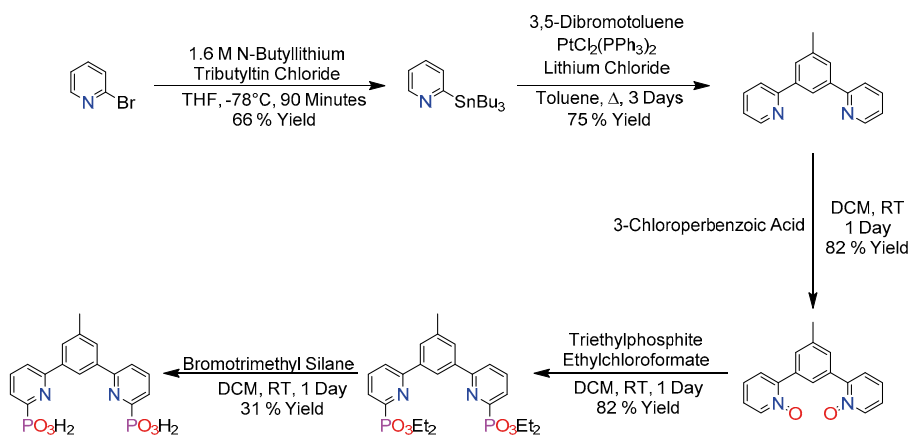
Figure 6.1. *Reaction scheme for the synthesis of the equatorial ligand ((5-methyl-1,3-phe-nylene)bis(pyridine-6,2-diyl))bis(phosphonic acid).*

With the equatorial ligand in hand, the Ru complex was prepared in a stepwise procedure by first coordinating the 1,3-phenylene-bis(pyridine-6,2-diyl)bisphosphonic acid to the $Ru(dmso)_4Cl_2$ precursor. Following the coordi-nation of the equatorial ligand, a large excess of 4,4-bipryidine (10 equiva-lents) was added, und the resulting solution heated to reflux for three days. After solvent removal and several washing steps $Ru(dpa)(4,4'$-bipyridine$)_2$, abbreviated as **IV**, was obtained as a red solid in 27 % yield (see Figure 6.2.).
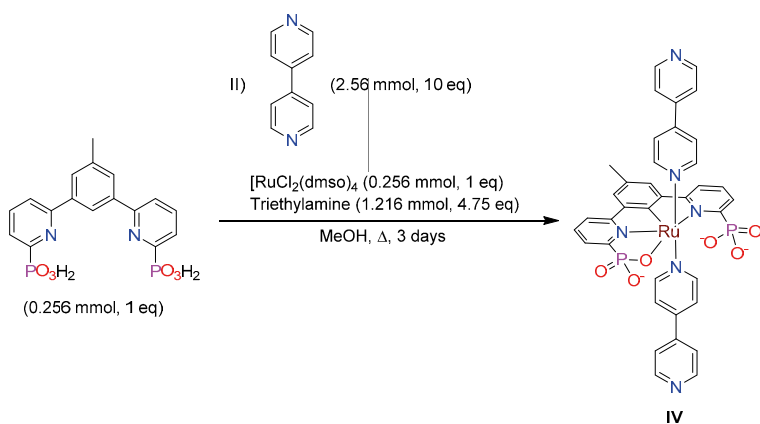
Figure 6.2. *Scheme for the synthesis of [Ru^{III}((5-Methyl-1,3-Phenylene)Bis(Pyridine-6,2-Diyl))Bis(Phosphonic Acid)(4,4'-Biprydine)_2] (**IV**).*

Formation of the coordination oligomer can be controlled by changing the solvent conditions and the ratio between 4,4'-bipyridine and [Ru^{III}(dpa)(4,4'-bipyridine)_2], which precipitates from the reaction mixture during refluxing 5 days. The oligomer, hereafter abbreviated as **n**, was collected and purified via washing with DCM and DCM/MeOH (see Figure 6.3.).
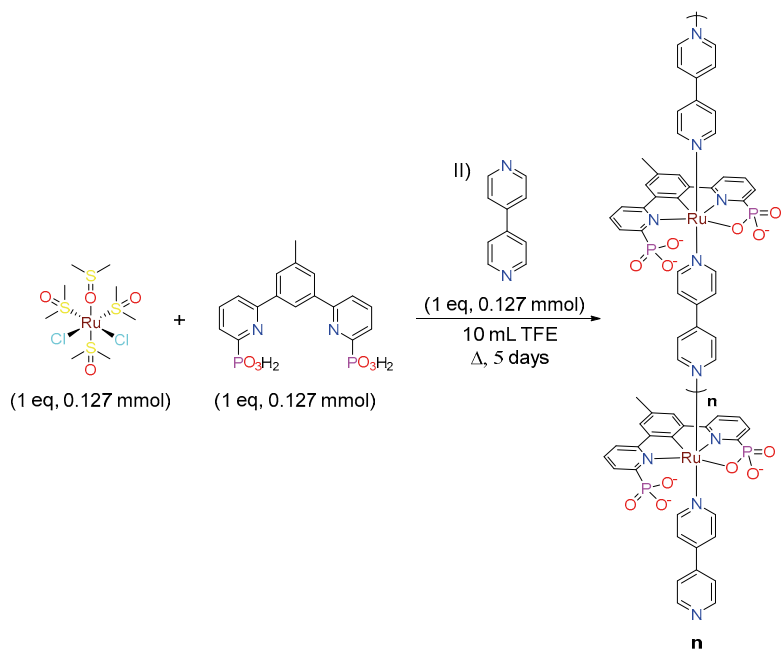
Figure 6.3. *Scheme for the synthesis of [Ru^{III}((5-Methyl-1,3-Phenylene)Bis(Pyridine-6,2-Diyl))Bis(Phosphonic Acid)(4,4'-Biprydine)_2]_n (**n**).*

Solutions of oligomer **n** in TFA are dark yellow, and exhibit a strong affinity for graphitic surfaces. Introducing this solution to a suspension containing MWCNT in THF at room temperature, leads to a decolourisation of the solution after a short period of time, indicating absorption of **n** onto the MWCNT and formation of a molecular hybrid material **n@MWCNT** (see Figure 6.4.). Suspensions of **n@MWCNT** can be drop-casted on the surface of a GC electrode for electrochemical characterisation.
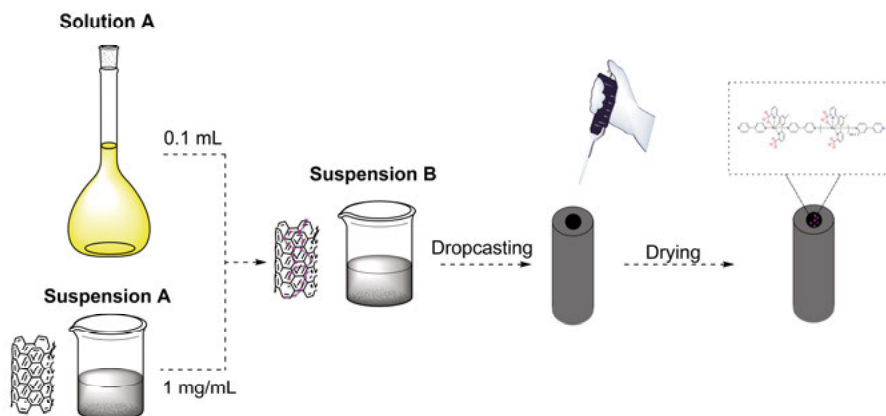
Figure 6.4. *Schematic diagram for the preparation of **n@MWCNT** electrode.*

6.3 Characterisation of Monomer and Oligomer

It's important to highlight that **IV** was isolated in the $Ru^{(III)}$ oxidation state, as confirmed by NMR spectroscopy. The addition of an excess amount of sodium ascorbate as a reducing agent, typically used to reduce $Ru^{(III)}$ species to their $Ru^{(II)}$ derivatives, did not improve the NMR response. This can be explained by the relatively low reduction potential of sodium ascorbate, in analogy to an observation by Vereshchuk et al on $[Ru^{III}(Xpda)(py)_2]$ type complexes.[188] The same paramagnetic nature of the complex was observed in the oligomeric **n**, making the molecular complex and the coordination oligomer impossible to characterize by NMR spectroscopy.

Complex **IV** could however be characterised by HR-MS, which showed a mass of m/z = 816.0594, which corresponds to the calculated molecular mass of the desired complex (Figure 6.5.).
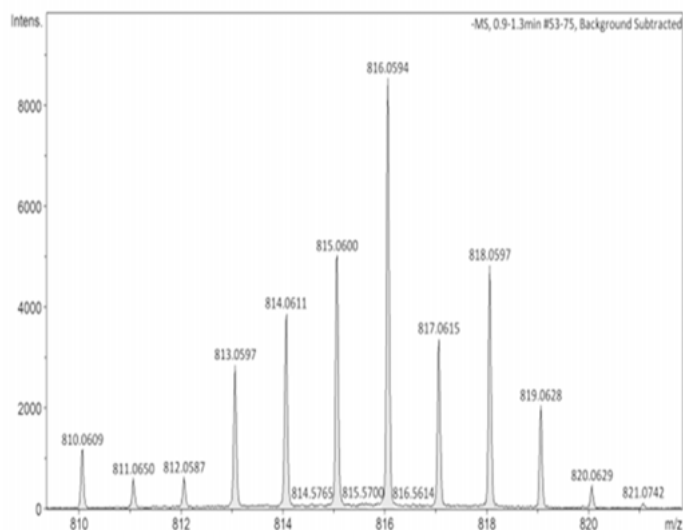
Figure 6.5. *Accurate mass of (IV).*

Monomeric complex **IV** and oligomer **n** were characterised and compared using electron paramagnetic resonance (EPR) spectroscopy (see Figure 6.6). Solutions of **IV** and **n** in TFE exhibited features between 2500-4000 G. The monomer species shows three features at 2680, 2953 and 3029 G, along with hyperfine features visible at 3279 – 3400 G. The EPR-spectrum of **IV** can be simulated with two overlapping EPR-signals.

The first signal (Ru[1]) was simulated with g-values of 2.494, 2.24, and 1.735 and using an anisotropic H-strain of 500, 370, and 900 MHz to simulate the observed line-broadening. The second signal (Ru[2]) was simulated with g-values of 2.268, 2.183, and 1.93 and using an isotropic H-strain of 160 MHz for the line-broadening. This finding is a consequence of the dynamic equilibrium of the equatorial ligand, which is observable at low temperatures.

UV-VIS spectra of **IV** and **n** are very similar, as expected, and show intense absorption bands between 270 nm – 440 nm. These absorptions are assigned to π-π* transitions on the ligand, and less intense MLCT transitions in the visible region (Figure 6.7). The increased absorption around 400 nm is attributed to the higher degree of conjugation in the oligomer **n**.
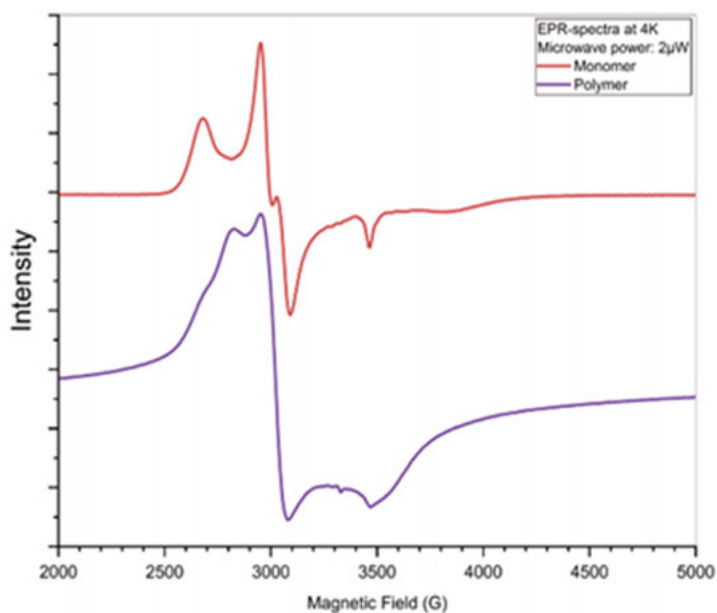
Figure 6.6. *EPR spectrum of a solution of **IV** (red trace) and **n** (purple trace) in pure TFE.*
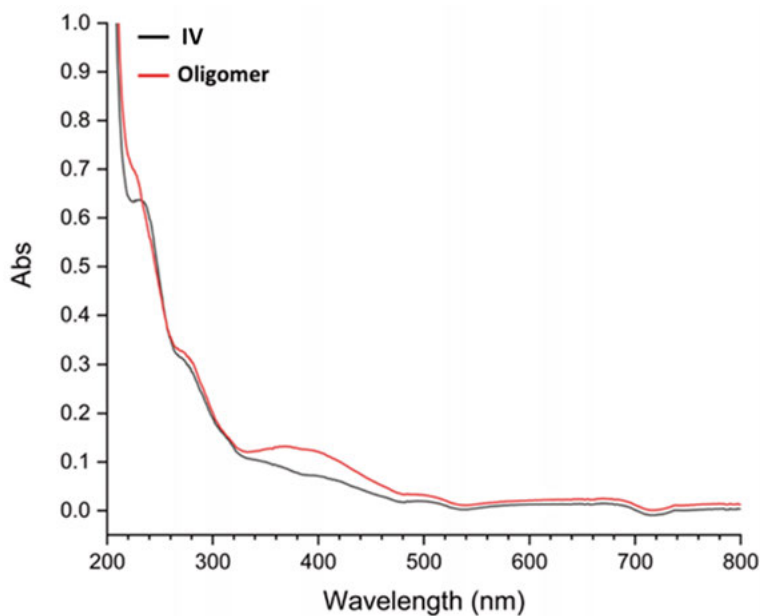
Figure 6.7. *UV-VIS absorption spectrum of a solution of **IV** and **n** in pure TFE.*

Scanning electron microscopy (SEM) and energy dispersive X-ray spectroscopy (EDX) was used to observe the morphology of oligomer **n** and the distribution of elements inside of the particles (see Figure 6.8).
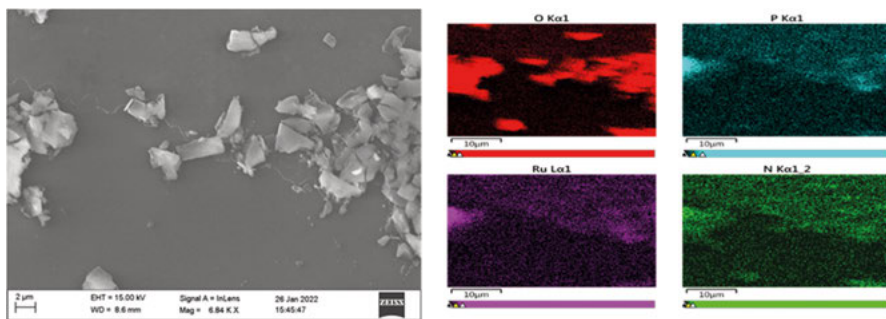
Figure 6.8. *SEM and EDX of oligomer (**n**).*

X-ray absorption near edge (XANES) and extended X-ray absorption fine structure (EXAFS) spectroscopy was used to characterise the electronic and structural properties of the oligomer (Figure 6.9 and Table 3 and 4). Half-edge energies obtained from XANES were consistent with the oxidation state assignments, and the parameters obtained by EXAFS. A list of the bond distances extracted from EXAFS analysis and obtained within the first coordination shell is shown in Table 3.

Analysis of the EXAFS spectra of the bulk powder of **n**, which possesses an oxidation state +3 could be fitted with 2 Ru-N/C distances at 1.90 Å and 4 Ru-N/O distances at 2.07 Å. The pre-activated oligomer **n** on the MWCNT also contained 100 % Ru$^{(III)}$ species on the surface, with 2 Ru-N/C distances at 1.89 Å and 4 Ru-N/O distances at 2.11 Å. The activated oligomer (**n'(H$_2$O)**, see below) exhibited two oxidation states, determined to be 62.5 % Ru$^{(III)}$ and 37.5 % Ru$^{(IV)}$, with 2 Ru-N/C distances at 1.95 Å and 4 Ru-N/O distances at 2.11 Å.

XAS spectroscopy showed the absence of any traces of RuO$_2$ after activation. This can be monitored by the absence of RuO$_2$ EXAFS spectral features. This is significant since it clearly demonstrates the molecular nature of the catalyst in heterogeneous phase, in sharp contrast with many instances where the original molecular catalyst is transformed to the corresponding metal oxide that ends up being the active catalyst.
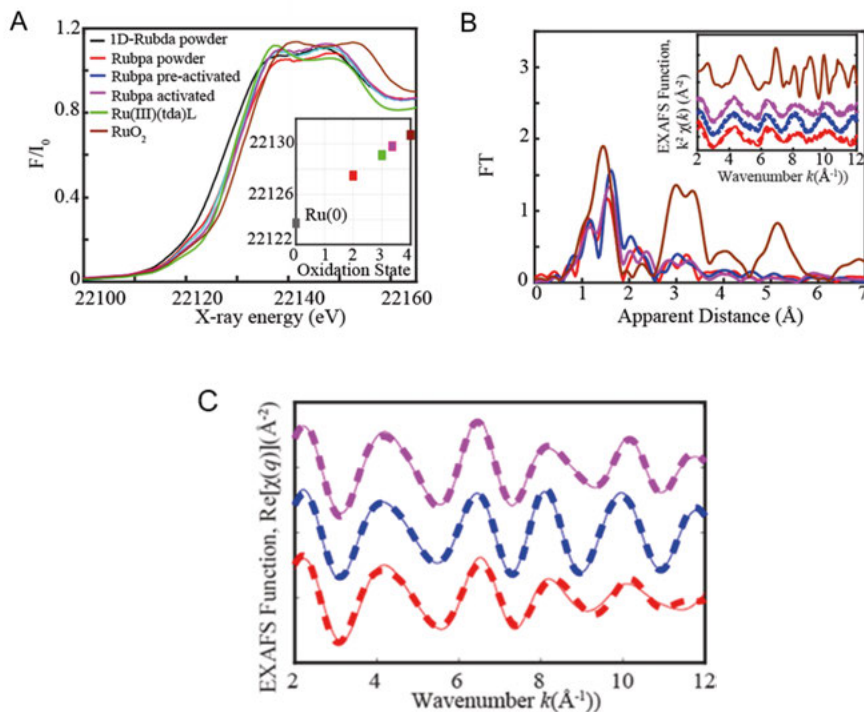
Figure 6.9. *A, Normalized Ru K-edge XANES for Rubda-1D complex from [62](**black**), **n** bulk powder (**red**), **n@MWCNT** (**blue**), **n'(H_2O)@MWCNT** (**magenta**), together with Ru^{III}tda reference complex from [31] (**green**) and RuO_2 (**brown**). **Inset.** Plot of half peak k-edge energy vs. oxidation state. **B**. Fourier transform of k^2-weighted) of n bulk powder (**red**), **n@MWCNT** (**blue**), **n'(H_2O)@MWCNT** (**magenta**) and RuO_2 (**brown**). **C**, Back Fourier transformed experimental (solid lines) and fitted (dashed lines) $k_2[\chi(k)]$ of Ru complexes together with RuO_2(brown). Experimental spectra were calculated for k values of 2-12 $Å^{-1}$.*

Table 3. *Summary of bond distances (Å).*

Sample	Bond distances (Å)
Rubpa solid (**n**)	**Ru-N/C,2: 1.90**
	Ru-N/O,4: 2.07
Ru(dpa) pre-activated on MWCNT (**n@MWCNT**)	**Ru-N/C,2: 1.89**
	Ru-N/O,4: 2.11
Ru(dpa) activated on MWCNT	**Ru-N/C,2: 1.95**
(**n'(H_2O)@MWCNT**)	**Ru-N/O: 2.11**

98

Table 4. *Comparison of XANES energies for all Ru complexes.*

Sample	Energy at Normalized Fluorescence 0.6 (eV)	Percentage Presence of Ru(II),Ru(III) and Ru(IV)	Oxidation State
Ru(0)	22123.7	-	**0**
Ru[III](tda)L from Matheu et al.[31]	22129.1	**100 % Ru(III)**	**3**
RuO_2	22130.7	**100 % Ru(IV)**	**4**
1D-Ru(bda) powder from[62]	22127.5	**100 % Ru(II)**	**2**
Ru(dpa) powder (**n**)	22129.1	**100 % Ru(III)**	**3**
Ru(dpa) pre-activated on MWCNT (**n@MWCNT**)	22129.1	**100 % Ru(III)**	**3**
Ru(dpa) activated on MWCNT (**n'(H_2O)@MWCNT**)	22129.7	**62.5 Ru(III) + 37.5 % Ru (IV)**	**3.38**

AFM micrographs in Figure 6.10 show the coordination oligomer **n** stacked on the surface of MWCNT, with the overall length of the oligomer being determined to 27.1 – 28 nm. The oligomers appear as thin rod-like shapes on the surface of the multi-wall carbon nanotubes. XPS is used to confirm the presence of **n** on the surface of the multi-wall carbon nanotubes, as the nitrogen, oxygen and phosphorus spectra are diagnostic for the coordination oligomer.
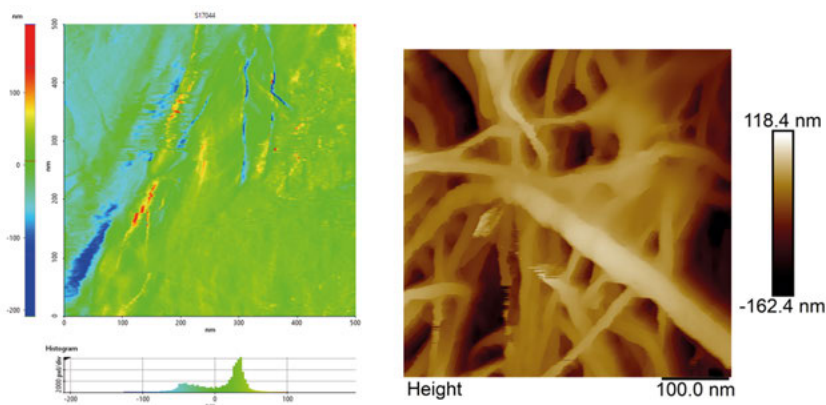
Figure 6.10. *AFM of coordination oligomer stacked on the surface of multi-wall carbon nanotubes.*

6.4 Electrochemical Properties of IV

The CV of **IV** features a reversible redox couple at $E_{1/2} = 0.08$ V, assigned to the $Ru^{(III/II)}$ couple, followed by a highly irreversible process with an anodic peak potential of 0.44 V that is assigned to the $Ru^{(IV/III)}$ couple (Figure 6.11, left.). Successive scans of up to 1.6 V show no water oxidation or transformation into the active catalyst (see Figure 6.11, right). Furthermore, the second redox couple of **IV** exhibited scan rate dependency, in which the returning wave of the $Ru^{(IV/III)}$ would disappear at high scan rates.

Interestingly, even after applying a constant potential of 1.35 V for 18 hours at pH 7 promoted an observable change in the CV. From these studies, it can be concluded that **IV** is a highly stable species, but unfortunately inert as a catalyst when subjected to rigorous oxidative conditions.
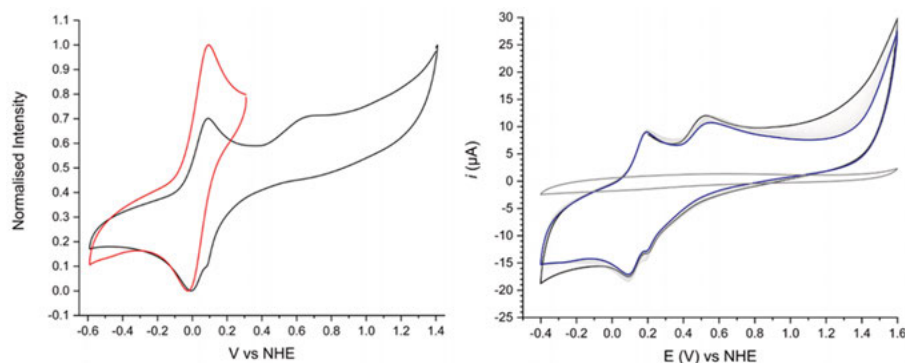
Figure 6.11. *Left, CV of **IV** conducted at pH 7 in 0.1 M phosphate buffer solution. Scan range of up to 1.4 V (black trace), Scan range of up to 0. 25 V (red trace). Right, CV at a potential of -0.4 – 1.6 V at 100 mV/s⁻¹. Blank GC electrode (grey trace), Initial scan (black trace), 50th scan (blue trace).*

6.5 Coordination Oligomer Electrochemistry

The procedure described in Figure 6.4 allows the species on the surface of a glassy carbon electrode to be readily investigated using electrochemical techniques. The CV of **n@MWCNT@GC** featured two reversible waves at $E_{1/2} = 0.07$ V and 0.44 V that were assigned to the $Ru^{(III/II)}$ and $Ru^{(IV/III)}$ couples, respectively. Especially the reversibility of the second oxidation is different from the initial electrochemical behaviour of the homogenous complex **IV**.

6.5.1 Surface-Promoted Transformation of Coordination Oligomer

The surface-promoted transformation of **n@MWCNT@GC** was analysed using 50 repetitive CV scans. At a potential range between -0.4 V and 1.4 V (100 mV/s in 0.1 M pH 7 phbs), no transformation of **n@MWCNT@GC** was observed. Upon extending the potential range to 1.6 V (Figure 6.12.), each successive scan gives rise to an increased current response of the catalytic wave at $E_{onset} = 1.19$ V. At the same time, the intensity of the initial redox couples decreased, while new redox processes emerged. This is a clear indication that the initial species is being transformed into a new catalytically active species, which is designated as **n'(H₂O)@MWCNT** hereafter.
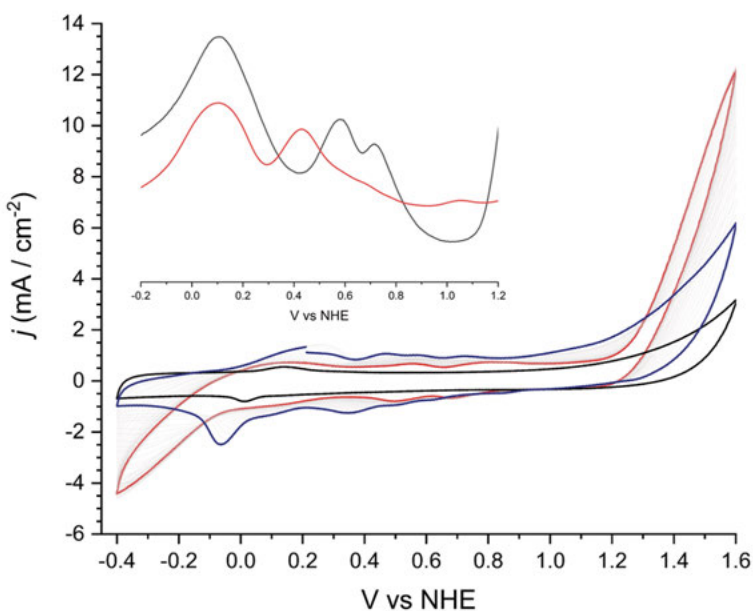
Figure 6.12. *CV of **n@MWCNT** conducted in pH 7 in 0.1 M phosphate buffer solution. Blank GC electrode (black trace), **n@MWCNT** initial scan (blue trace), **n'(H₂O)@MWCNT** species generated after 50ᵗʰ scan of CV experiment (red trace). Insert: DPV of coordination polymer before and after 50 CV cycle. Initial electrode (red trace) and activated electrode (black trace).*

After 50 successive CV scans, the initial species and the new species can both be observed. The new set of redox processes can be observed at $E_{1/2} = 0.53$ V (60 mV, $Ru^{(III/II)}$) and $E_{1/2} = 0.74$ V (116 mV, $Ru^{(IV/III)}$). The changes between the initial and activated electrode are clearly observed in the DPV (Figure 6.12). The redox potentials of the couples for the initial species **n@MWCNT@GC** and the catalytically active species **n'(H₂O)@MWCNT**

were analysed as a function of pH (between 2-10), and Pourbaix diagrams of the activated electrodes were constructed (Figure 6.13.).

The redox couples associated with the initial electrode and the "activated" electrode are pH-dependent, which is expected due to the presence of the dangling phosphonate groups, which can protonate and deprotonate, depending on the pH. In addition, water that is coordinated to the Ru centre can be deprotonated, especially when going to higher oxidation states. In aqueous solution, oxidation states of II – V are accessible over a narrow potential range. The species lines were drawn according to the Nernst equation with slopes of -59 and -126 mV/pH unit.
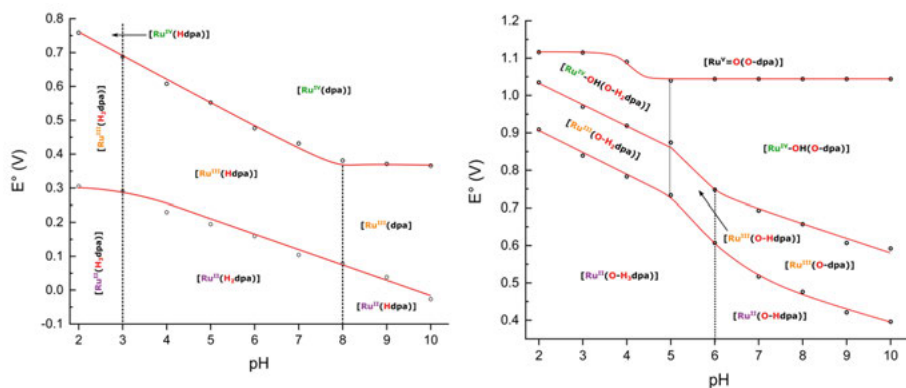
Figure 6.13. *Pourbaix diagram of oligomer **(n)**. The redox potentials are plotted as a function of pH; the oxidation state is indicated as well as the degree of protonation of the aqua species. The dashed vertical lines indicate the pKa of the species involved. Left, **n@MWCNT@GC** electrode prior to activation. Right, **n'(H₂O)@MWCNT@GC** activated electrode.*

A mechanism for activation of the pre-catalyst and a catalytic cycle is proposed in Figures 6.14. and Figure 6.15, respectively. Examination of the Pourbaix diagram reveals the presence of one aqua species, consistent with the situation in other ruthenium catalysts with sequential PCET steps.[29] However, the mechanistic proposal for the transformation of the pre-catalyst to the active Ru-aqua complex was markedly different, and could not be proposed in analogy to those of the Ru-tda family. Instead, an irreversible, permanent and high energy transformation of the initial species has to be invoked. This is because the simple addition of water onto a $Ru^{(IV)}$ species, as observed in the Ru-tda type molecular complexes, was inconsistent with what is observed in the Pourbaix diagram of the active catalyst.

Therefore, an activation mechanism and a catalytic cycle are proposed in analogy to the work by Vereshchuk et al[187] on $[Ru^{II}(H_4tPa)(Py)_2]$. The latter complex contains a terpyridine-based equatorial ligand, but is otherwise structurally identical, in particular in terms of the phosphonate groups that can

102

coordinate to the Ru centre. As shown in Figure 6.14, $[Ru^{II}(H_2dpa\text{-}\kappa\text{-}N^2C)(py)_2]$, **1**, is converted to $[Ru^{III}(Hdpa\text{-}\kappa\text{-}N^2C)(py)_2]$, **2**, via a PCET at an applied potential of 0.1 V, followed by another PCET step at 0.43 V to form $[Ru^{IV}(dpa\text{-}\kappa\text{-}N^2C)(py)_2]$, **3**. At higher potential, a transformation on the equatorial ligand must occur to start the catalytic cycle. Higher electron density on the complex due to the presence of the carbanion allows dissociation of a pyridine and a phosphonate groups, followed by addition of water, protonation of phosphonate and loss of proton, to form intermediate $[Ru^{IV}(O\text{-}Hdpa\text{-}\kappa\text{-}NC)(py)_2]$, **4**, followed by a PCET to form $[Ru^{V}(O\text{-}dpa\text{-}\kappa\text{-}NC)(py)_2]$ **5**. A permanent transformation of the catalyst is proposed in analogy to the work by Vereshchuk et al.[187] When decoordinated, the pyridine ligand can rotate to expose its 3-position to the high-valent $Ru^{(V)}$-oxo species which can easily oxidise the pyridine ring to form $[Ru^{II}(O\text{-}dpa\text{-}\kappa\text{-}NC)(py)_2]$, **6**.

In Figure 6.15, a proposition of the catalytic cycle is presented. It starts with the addition of water onto species **6**, followed by a PCET step to form the Ru-aqua species $[Ru^{IV}\text{-}OH(O\text{-}dpa\text{-}\kappa\text{-}NC)(py)_2]$, **7**, followed by a further PCET step to form $[Ru^{V}=O(O\text{-}dpa\text{-}\kappa\text{-}NC)(py)_2]$, **8**. The Ru-hydroperoxyl species is formed by a nucleophilic attack of water onto the $Ru^{(V)}$-oxo state to create the O-O bond and protonation of the phosphonate, leading to $[Ru^{III}\text{-}O\text{-}OH(O\text{-}Hdpa\text{-}\kappa\text{-}NC)(py)_2]$, **9**. Finally, the catalytic cycle is completed via a final PCET step to give intermediate $[Ru^{IV}\text{-}O\text{-}O(O\text{-}Hdpa\text{-}\kappa\text{-}NC)(py)_2]$ **10**, loss of oxygen $[Ru^{II}(O\text{-}Hdpa\text{-}\kappa\text{-}NC)(py)_2]$, **11**, followed by a final PCET step to regenerate $[Ru^{II}(O\text{-}dpa\text{-}\kappa\text{-}NC)(py)_2]$, **6**.
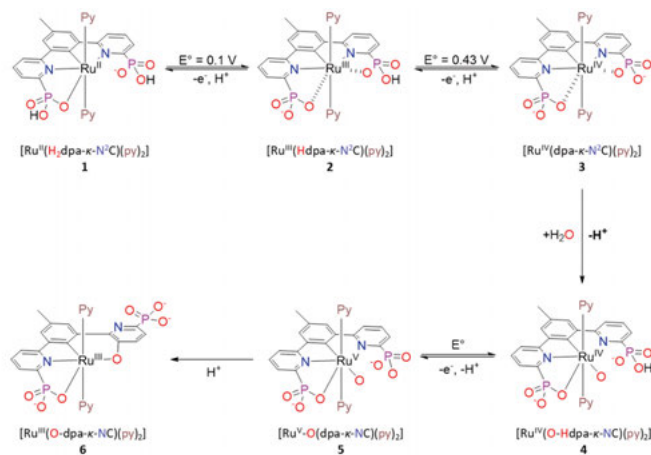
Figure 6.14. *Activation of the electrode by the electrochemical conversion of* ***n@MWCNT@GC*** *to* ***n'(H₂O)@MWCNT@GC*** *via ligand oxidation and coordination of aqua ligands on the ruthenium complexes.*
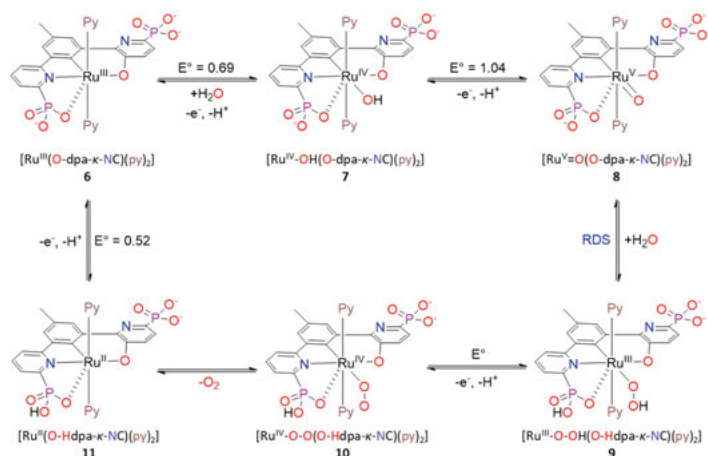
Figure 6.15. *Proposed catalytic cycle of* ***n'(H₂O)@MWCNT@GC***.

6.5.2 Performance of **n'(H₂O)@MWCNT** as a Molecular Water Oxidation Anode

The electrocatalytic performance of **n'(H2O)@MWCNT** electrodes was kinetically characterised using foot-of-the-wave analysis (FOWA) of the active species (after 50 CV cycles), giving a TOF_{max} value of 3000 s^{-1} (see Figure 6.16).

The electroactive surface coverage of the pre-activated oligomer on a vitreous GC plate (0.5 cm^2) was determined from the integrated current response to be $\Gamma_{Initial}$ = 6.21 nmol/cm^2. During CV 50 cycles, the initial species has completely converted to the new catalytically active species, with the surface concentration of the new species having a surface coverage of Γ_{Scans} = 5.33 nmol/cm^2. This number is very similar to the one of the pre-activated state, pointing towards little loss of material from the electrode during the activation step. In both cases, the active surface coverage was calculated using equations 3 and 4. The active species on the surface of the electrode subsequently reaches current densities in the range of 5.23 mA/cm^2 at an applied potential of 1.4 V in 1 M pH 7 phbs for 3200 seconds.
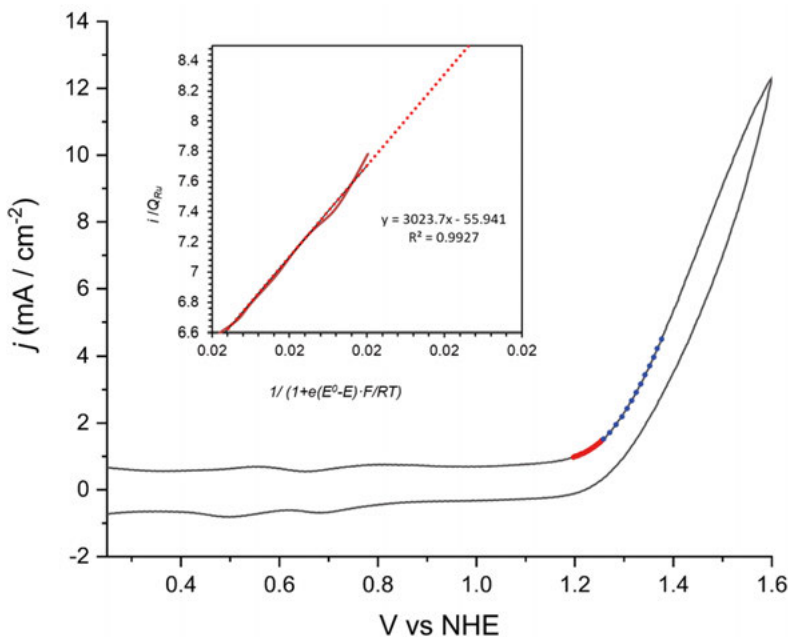
Figure 6.16. *CV scan of the activated electrode at 100 mV/s⁻¹. Inset: Foot of the wave analysis (FOWA) of* ***n'(H₂O)@MWCNT@GC****. S = 0.071 cm² I = 0.1 M pH = 7*

$$\frac{i}{Q_{Ru}} = \frac{k_{WNA}}{1+\exp(\frac{F(E-E^O)}{RT})} \qquad \textbf{Eq. 1}$$

$$TOF = \frac{k_{wna}}{1+e^{\left(\frac{F\left(E^O - E_{\frac{H_2O}{O_2}} - \eta\right)}{RT}\right)}} \qquad \textbf{Eq. 2}$$

$$\Gamma \ (mol \cdot cm^{-2}) = \frac{Q_{av}}{n^{e-} \cdot S \cdot F} \qquad \textbf{Eq. 3}$$

$$Q_{av} = \frac{Q_{ap \ Ru^{III/II}} + Q_{cp \ Ru^{II/III}}}{2} \qquad \textbf{Eq. 4}$$

Equations 5 and 6 give rise to a TOF of 2.16×10^3 s⁻¹ and a TON of 6.92×10^6.[189]

$$TOF = \left(\frac{\frac{i}{S}}{(\Gamma \times F \times n)}\right) \times FE = 2161.09 \ s^{-1} \qquad \textbf{Eq. 5}$$

$$TON = TOF \times t = 6.92 \times 10^6 \qquad \textbf{Eq. 6}$$

where, i = current (0.002615 A), S = surface area of the electrode (0.5 cm^2), Γ = surface coverage of catalyst (5.33 nmol/cm^2), F = Faraday constant (96485 s*A/mol), n = number of electrons (4e$^-$), t = time carrying out bulk electrolysis (3200 s) and FE = faradaic efficiency of water oxidation (0.85). The surface coverage, as depicted in Figure 6.17. was also calculated.

$$S_{12@GC} \; = \; \frac{\Gamma \cdot S \cdot N_A \cdot S_{coverage}}{n_{Ru'}} \qquad\qquad \textbf{Eq. 7}$$

$$Coverage \; (\%)_{n@GC} \; = \; \frac{S_{coverage@GC}}{S} x \; 100 = \; 73.2 \; \% \qquad \textbf{Eq. 8}$$

Γ = 5.33 x 10^{-9} mol cm^{-2} is calculated according to Equations 3 and 4 (See Figure 6.18). The surface coverage (S$_{coverage}$) is calculated using formula 7, where N_A is the Avogadro's number (6.023 x 10^{23}) n_{Ru} is the number of Ru units per oligomer. The number of monomeric units in the oligomer was estimated from the chain length determined by AFM (L = 27.1 nm) and the known Ru-Ru and 4,4'-bipyridine bond distances of other coordination oligomers reported in the literature. The values that were used for calculating the number of monomer units were Ru-Ru distances of 1.14 nm and a 4,4'-bipyridine length of 0.92 nm.

This analysis gave a rough estimate of 23 monomers for each strand of oligomer (1.14 nm × 23)+ 0.92 nm = 27.14 nm). With this estimate, the surface area of the oligomer was calculated with the approximate rectangle generated by, S_{12} = [(1.14 x 10^{-9} x 23) x 1 x 10^{-9}] = 26.22 nm^2 or 2.622 x 10^{-17} m^2. This implies a surface of 3.66 x 10^{-5} m^2 (Size of n is approx. 23 units long, or 2.622 x 10^{-17} m^2/molecule) or 0.366 cm^2. Since the surface of the GC electrode is 0.5 cm^2 this analysis gives a surface coverage of 73%, based on the geometric surface area of the electrode. This number should however not be confused with a surface coverage of the MWCNTs, which give rise to a considerably higher internal surface area which will greatly dilute the surface coverage.
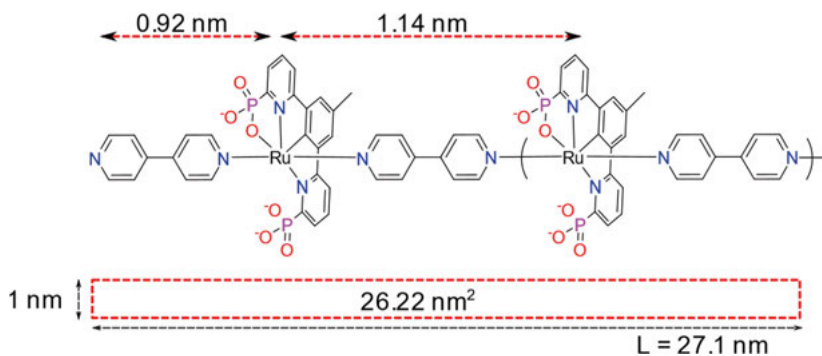
Figure 6.17. *Drawing of **n** with key metric parameters.*
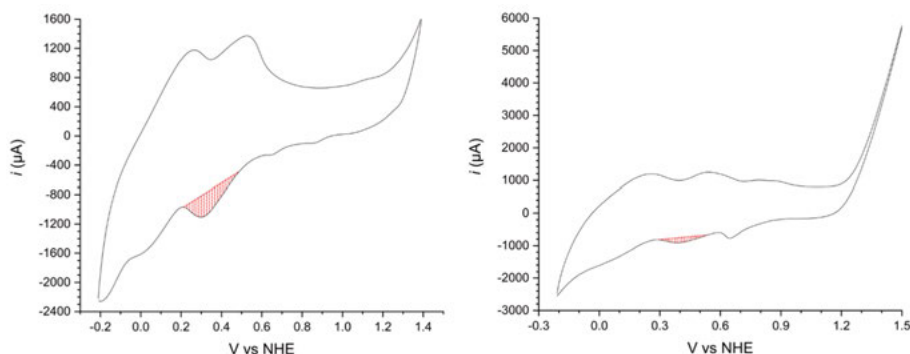
Figure 6.18. *CV of **n@MWCNT@GC** which gives rise to an initial active surface concentration of 6.21 nmol/cm^2, and **n'(H$_2$O)@MWCNT@GC** which gave a surface concentration of 5.33 nmol/cm^2. Highlighted regions show the areas employed for calculating the charge (Q).*

6.5.3 Oxygen Evolution of **n'(H₂O)@MWCNT**

The current observed during controlled potential electrolysis was stable over 3200 seconds, and an evaluation of the anode by CV during electrolysis showed the absence of any new features that could be attributed to any new redox active species. The Faradaic efficiency of the oxygen evolution in the CPE experiment was evaluated with a Clarke-type electrode placed into the headspace of the anode compartment.

$$Faradaic\ Efficiency\ (FE) = \frac{\mu mol\ O_2}{\left(\frac{Q}{F\ x\ n^{e-}}\right)}\ x\ 100 \qquad \textbf{Eq. 9}$$

As shown in Figure 6.19., applying a constant potential of 1.4 V to the anode results in oxygen evolution. Over the timescale of 53 minutes, total oxygen concentration increases linearly, further supporting the notion that **n'(H₂O)@MWCNT** is a durable catalyst. After electrolysis, a total of 18.451 µmols of O_2 were detected, while the total charge passed through the cell was 8.37 C. Together, these two values give a Faradaic efficiency of 85%.
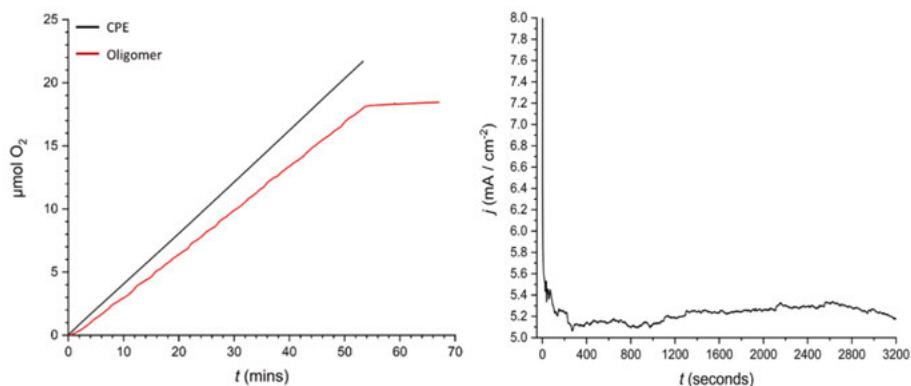
Figure 6.19. *Left, CPE coupled to oxygen evolution measurement of* **n(H₂O)@MWCNT@GC**. *(1.4 V vs. NHE in a 0.1 M phbf (pH 7) (red trace); theoretical O₂ from the CPE (black trace). A Faradaic efficiency value of 85 % was calculated. Right: current density vs. time trace for the CPE of the oligomer over 3200 seconds.*

Catalytic Tafel plots were constructed to benchmark the catalytic activity of (**n'(H₂O)@MWCNT**), and to compare it to related materials from the literature. For comparison, two oligomeric materials were used that differ in the equatorial ligands and the number of monomeric Ru units. The reference materials were [Ru(bda)(H₂O)₂(4,4'-bpy)₁₀(4,4'-bpy)][62] and [Ru(tda)(H₂O)(4,4'-bpy)₁₅(4,4'-bpy)].[61] The constructed Tafel plots relate the TOF of the catalyst to the applied potential with respect to the standard potential of the reaction.[120, 121] The catalytic Tafel graphs were drawn by plotting TOF as a function of overpotential (η), following equations 1 and 2 in this chapter for the FOWA for the hetero-WNA mechanisms[30].

The catalytic Tafel plots enable rapid and facile comparison between different coordination oligomers, with each Tafel plot reflecting the distinctive features of the catalyst. TOF_{max} shows the apparent rate at which the curve reaches a plateau. This provided a comprehensive evaluation of the performance of the catalyst as a function of overpotential. The Tafel plot show Ru-bda oligomer [Ru(bda)(H₂O)₂(4,4'-bpy)₁₀(4,4'-bpy)] does operate at a lower overpotential. However, at higher overpotential, both [Ru(bda)(H₂O)₂(4,4'-bpy)₁₀(4,4'-bpy)] and [Ru(dpa)(H₂O)(4,4'-bpy)ₙ(4,4'-bpy)] (**n'**) reach a comparable performance. However, [Ru(dpa)(H₂O)(4,4'-bpy)ₙ(4,4'-bpy)] has a similar catalytic profile as [Ru(tda)(H₂O)(4,4'-bpy)₁₅(4,4'-bpy)] (see Figure 6.20.).
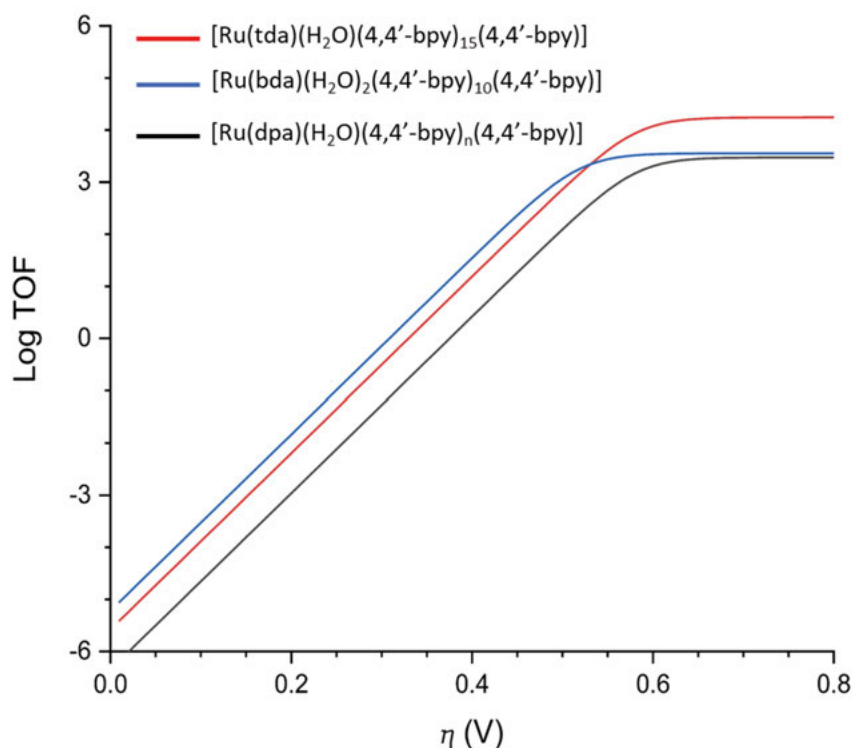
Figure 6.20. *Tafel plot of activated coordination oligomers in 0.1 M pH 7 phbf (S = 0.071 cm⁻²). Tafel plot of carbanion coordination oligomer [Ru(dpa)(4,4'-bpy)]ₙ(4,4'-bpy)] (black trace). Ru-bda coordination oligomer [Ru(bda)(4,4'-bpy)]₁₀(4,4'-bpy)] (blue trace). Ru-tda coordination oligomer [Ru(tda)(4,4'-bpy)]₁₅(4,4'-bpy)] (red trace).*

6.6 Conclusion

When the carbanion FAME complex is incorporated into a coordination oligomer (**n**) and stacked onto the surface of MWCNTs, the oligomer can engage in an oxidative transformation to yield an active water oxidation catalyst. at present, the mechanistic proposal of its catalytic cycle is based on analogies to published interpretations of Pourbaix diagrams, and further study using computational methods are ongoing. Additionally, the exact reason why the activation is not observed in the monomeric complex **IV** is still unclear at present. In the absence of any supramolecular interactions that assist in stabilising the proposed high energy intermediates, the equatorial ligand in **IV** may be more tightly bound to the metal centre, affecting its ability to irreversibly transform to the catalytically active state.

This work is another step in the development of durable electrochemical water oxidation catalysts. Most remarkably, unlike other previous examples of water oxidation coordination oligomers, monomeric **IV** is inactive towards water oxidation, but can be transformed into an active catalyst after incorporation into a molecular coordination oligomer. This represents an experimental confirmation that supramolecular interactions facilitate catalysis in complexes that are reported to be highly stable and inert, and opens up the scope of possible molecular complexes that can be used in electrocatalytic reactions.

7 Summary and Future Outlook

This thesis summarises efforts toward solving synthetic difficulties associated with the development of functional MOF platforms. More specifically, this work is focused on the design of MOFs, where molecular water oxidation catalyst linkers are incorporated via post-synthetic exchange, co-synthesis strategies and direct solvothermal synthesis. MOFs can be synthetically challenging and require particular attention with respect to the functional molecule of interest, the target topology, and other factors. Different linker motifs may require different synthetic strategies for their incorporation into crystalline MOF materials. This issue was investigated in detail in Chapter 3 of this thesis, where the incorporation of $Ru(tda)(py)_2$ water oxidation catalyst derivatives was investigated using various synthetic strategies. During the course of the work, post-synthetic modifications were found to be the most effective methods for introducing a Ru(tda)-based ditopic linker into a UiO-type MOF. Final investigation of the final UiO-based Ru-MOF products indicated that linker incorporation had proceeded mostly by filling missing-linker defects instead of exchanging structural linkers.

In chapter 4, a tetratopic version of the same Ru-tda molecular complex was used as a linker, and successfully incorporated with an inert co-linker to produce a mixed-linker version of NU-1000 using direct solvothermal synthesis. This mixed-linker MOF was characterised and its Faradaic efficiency for water oxidation was assessed at an applied potential of 1.30 V vs. NHE. At this potential, the TBAPy co-linkers are oxidatively transformed, resulting in a low Faradaic efficiency for water oxidation of 37%. Despite the low Faradaic efficiency for water oxidation, the use of redox-active pyrene moieties to facilitate hole transport could be established as a novel strategy that is unprecedented for anodic processes. This opens up the possibility of further investigation of other kinds of mixed-linker MOFs materials that engage in electrocatalysis by using a more stable inert linker that does not undergo transformation at water oxidation potentials.

These initial MOF studies used Ru-tda type of complexes, the dangling carboxylate of which interfered with the solvothermal synthesis of crystalline MOFs. This shortcoming could be eliminated when the catalyst motif was changed to Ru-bda type complexes. The resulting MOF reported in chapter 5 is the first example of a MOF that is constructed exclusively from Ru-based

water oxidation catalyst linkers. MOF incorporation of the catalyst linker leads to a substantial improvement of the structural stability of the catalyst. As a consequence, multiple CAN addition cycles could be performed, and water oxidation catalysis persisted for a considerable amount of time.

Lastly, a novel ruthenium carbanion molecular complex was explored as water oxidation catalyst. Interestingly, the molecular complex itself failed as a water oxidation catalyst, but led us to incorporate it into a coordination oligomer. In this oligomeric form and immobilised on MWCNTs, the supramolecular interaction between different strands of oligomer and the CH-π interactions with the nanotubes assisted in converting the pre-catalyst into an active catalyst. Water oxidation catalysed by the activated oligomer was observed at an applied potential of 1.4 V. Controlled potential electrolysis for one hour showed no sign of decomposition, and catalysis proceeded with a high Faradaic efficiency of 85 %. Moreover, the system is unique in that an inert, stable molecular complex can be turned into an active catalyst by incorporating it into a coordination oligomer.

In summary, the work presented in this thesis furthers our understanding of functional MOF platforms. It addresses different synthetic strategies to dope MOFs with functional molecules, to develop multi-functional MOFs, and furthers the scope of molecular complexes that can be used in electrocatalysis applications, by incorporating them into coordination oligomers.

Svensk Sammanfattning

Antropologiskt drivna klimatförändringar är en global utmaning som kräver samhälleliga, tekniska och politiska åtgärder. Energiförbrukningen är den största källan till antropologiska utsläpp av växthusgaser, som stod för 76 % av de globala växthusutsläppen 2019. För närvarande kommer majoriteten av den producerade energin från förbränning av fossila bränslen. Följaktligen är att ersätta icke-förnybara fossila bränslen med förnybara energikällor den viktigaste tekniska innovationen som är nödvändig för att minska utsläppen, öka energisäkerheten och skydda konsumenterna från de ständigt ökande kostnaderna för energi som produceras från fossila bränslen.

Vind och sol är förnybar energiteknik som är av kommersiell och statlig betydelse. Dessa källor producerar el som energibärare, men är också intermittenta, vilket begränsar deras effektivitet när de används i stor skala. Detta är en viktig fråga när energiefterfrågan plötsligt ökar vid olika perioder på en dag, vilket kan leda till strömavbrott om tillgången på el är otillräcklig på grund av miljöfaktorer som vindstillstånd eller svagt ljus. Därför bedrivs ytterligare forskning om teknik som syftar till att lagra överskottsenergi för senare användning när energibehovet ökar vid olika tidpunkter under en dag.

Energi lagrad i kemiska bindningar har en energitäthet som är hundra gånger mer energität än energilagring som finns i batterier när dess massa normaliseras i kilogram. Förutom bränslen kan elektroner användas för att driva andra kemiska produkter som används för andra kommersiella produkter.

Även om potentialen för denna nya och störande teknik inte kan underskattas, är det ofta komplicerat att omvandla elektrisk energi till kemisk energi. Detta fält inom elektrokemi kallas ofta för elektrokatalys. Detta är ett viktigt forskningsfält inom sektorn för förnybar energi, eftersom målet är att använda elektroner för att driva kemiska reaktioner. Detta kräver studier av katalysatorer och reaktionsförhållanden för att styra högenergielektroner att utföra specifika reaktioner.

För integrering i enheter måste dessa katalysatorer heterogeniseras på en yta. Dessa heterogeniserade elektroder för vattenoxidationskatalysatorer finns i två former, den ena är fastfas-nanopartikelbaserad och den andra är molekylärbaserad, vilket är ämnet för denna avhandling. Molekylära katalysatorer

kan inkorporeras i en mängd olika heterogeniserade strukturer; såsom 3-di-mensionella och porösa metallorganiska ramverk, där elektroner måste färdas genom materialet för att nå reaktionsställena för katalysatorerna. Ett annat al-ternativ är molekylära katalysatorer, som staplas icke-kovalent på grafitiska ytor för att bilda molekylära hybridmaterial. Dessa elektroner reagerar med råmaterial, som är kända som substrat, som färdas inuti eller på ytan av dessa molekylära anoder och hittar en elektron. När denna process inträffar sker en reaktion och en ny produkt bildas.

Denna avhandling beskriver integrering av molekylära katalysatorer i MOF och koordinationsoligomerer för att bilda molekylära anoder för vattenoxidat-ion. Inom denna avhandling beskrivs direkta, samsyntes och indirekta tekniker för inkorporering av ruteniummolekylära vattenoxidationskatalysatorer i MOF:er och tunna filmer, vilka strukturella och laddningsöverföringsegen-skaper är dessa MOF-material som beskrivs. Syntesen och användningen av molekylära koordinationsoligomerer för att inducera annars inerta molekylära katalysatorer att engagera sig i elektrokemisk vattenoxidation.

Denna avhandling ger nya perspektiv på molekylär katalys inom MOF:er ge-nom användning av indirekta, medierade elektron-/håltransportvägar för att oxidera avlägsna katalytiska centra för vattenoxidation. Detta arbete illustrerar också hur kraftfull inverkan supramolekylära interaktioner är, särskilt när det gäller att sänka aktiveringsbarriären för molekylär katalys.

Popular Science Summary

Anthropologically driven climate change is a global challenge, which requires societal, technological and political action to address. Energy consumption is the biggest source of anthropological greenhouse gas emissions, which was responsible for 76 % of global greenhouse emissions in 2019. Currently, the majority of the energy produced is derived from the combustion of fossil fuels. Consequently, replacing non-renewable fossil fuels with renewable sources of energy is the key technological innovation that is necessary to reduce emissions, increase energy security and insulate consumers from the ever-increasing cost of energy produced from fossil fuels.

Wind and solar are renewable energy technologies that are of commercial and governmental importance. These sources produce electricity as an energy carrier, but are also intermittent, which limits their effectiveness when used on a large scale. This is an important issue when energy demand suddenly spikes at different periods in a day, which could lead to power outages if supply of electricity is insufficient due to environmental factors such as no wind or low light conditions. Therefore, additional research is being carried out on technology aimed at storing surplus energy for later use when energy demand increases at different points in a day.

Energy stored in chemical bonds have an energy density that is more than one hundred times denser than energy storage found in batteries, when normalised by mass in kilograms. As well as fuels, electrons can be used to drive other chemical products that are used for other commercial products.

While the potential of this new and disruptive technology cannot be understated, converting electrical energy into chemical energy is often a complicated process. This field within electrochemistry is often referred to as electrocatalysis, which is an important field of research in the renewable energy sector, as the objective is to study catalysts to direct high-energy electrons to carry out specific reactions.

For integration into devices, these catalysts must be heterogenised on a surface. These heterogenised electrodes for water oxidation catalysts come in two forms, one is solid-phase nanoparticle based and the second is molecular based, which is the subject of this thesis. Molecular catalysts can be

incorporated into a variety of heterogenised structures; such as 3-dimensional and porous metal organic frameworks, where electrons must travel through the material to reach the reaction sites of the catalysts. Another option are molecular catalysts, which are non-covalently stacked onto graphitic surfaces to form molecular hybrid materials. These electrons react with raw materials, which are known as substrates, which travel inside or on the surface of these molecular anodes and find an electron. When this process occurs, a reaction occurs and a new product is formed.

This thesis discusses integration of molecular catalysts into MOFs and coordination oligomers to form molecular anodes for water oxidation. Within this thesis, direct, co-synthesis and indirect techniques for incorporation of ruthenium molecular water oxidation catalysts into MOFs and thin films are described. The synthesis and use of molecular coordination oligomers to induce otherwise inert molecular catalysts to engage in electrochemical water oxidation are also described.

This thesis provides new perspectives on molecular catalysis within MOFs through the use of indirect, mediated electron/hole transport pathways to oxidise remote catalytic centres for water oxidation. Also, this work illustrates how powerful the influence supramolecular interactions are, especially when it comes to lowering the activation barrier of molecular catalysis.

Acknowledgements

I would like to dedicate this thesis to my friends, family and colleagues. Without their advice and support, I couldn't be in the position of writing this thesis. Here, I would like to extend my gratitude to the following:

Prof. Sascha Ott, I thank you for the supervision, mentorship, support and advice throughout my time in Uppsala and during the eSCALED project. Thank you for giving me the opportunity to join your group and the freedom to explore new ideas.

Prof. Laurent Billon, I would like to thank you for your wisdom and guidance you provided me during eSCALED and during my stay in your group in IPREM.

Prof. Antoni Llobet, thank you for the support and guidance you provided me in the first year of my PhD, and ever since I left ICIQ. You are a first-class mentor, and I learned a phenomenal amount while working with you.

Dr. Carolina Gimbert-Suriñach, Thank you for your support and assistance both during my time in ICIQ and afterwards, which resulted in papers **II** and **IV**.

Dr. Marcos Gil-Sepulcre, thank you for your support and friendship during my time in ICIQ and your collaboration after I left, which has resulted in papers **II** and **IV**.

Dr. Laia Francesch, thank you for all the help and assistance you have given me and to everyone on the eSCALED project.

Prof. Antoine Bousquet, thank you for all the help and support during the eSCALED project. I appreciate all the efforts you have made in our development as PhD students and wish to thank you for all the interesting scientific discussions we have had and the guidance you provided during my stay at IPREM

Dr. Timofey Liseev, thank you for your friendship and collaboration while in Uppsala, which resulted in Papers **I** and **II**.

Thanks to my fellow ESRs in the eSCALED Project: **Ludovico**, **Andrew B**, **Afridi**, **Silvia, Domenico**, **Karell**, **Van**, **Ignasi**, **Diogo**, **Olivera**, **Robin** and **Bruno**.

I would like to thank the following in Uppsala, **Anna A**, **Salauat**, **Jordann**, **Ashleigh**, **Ben**, **Hemlata**, **Brian**, **Nicolas**, **Michele**, **Manuel**, **Kamal**, **Belinda**, **Holly**, **Nina**, **Wanja** for making the department a great place to work.

I would also like to thank everyone in ICIQ for their help inside and outside of the lab and for the warm, happy and welcoming atmosphere that I experience while there: **Marta**, **Nataliia**, **Primavera**, **Asmaul**, **Jan**, **Jan H**, **Sergi**, **Martina**, **Abi** and **Navid**.

Jessyka, **Patricia** and **Roger**, many thanks for all your care, help and support during my time in Pau. It was wonderful meeting all of you and gaining your friendship. Although we may be very far away, I know we will remain in touch.

Anna and **Ernesto**, I thank you both for all the moral support and friendship while in Uppsala. Thank you for helping me get settled in Uppsala and for including me in your family circle! I wish yourselves, Frank and your family all the best for the future.

Shauna, many thanks for always having my best interests at heart and for understanding me like nobody else, I couldn't have done got this far without you

Mam and Dad, many thanks for your support and encouragement over the years.

118

References

1. Rappaport, F.; Guergova-Kuras, M.; Nixon, P. J.; Diner, B. A.; Lavergne, J., Kinetics and Pathways of Charge Recombination in Photosystem II. *Biochemistry* **2002**, *41* (26), 8518-8527.

2. Brudvig, G. W., Water oxidation chemistry of photosystem II. *Philosophical Transactions of the Royal Society B: Biological Sciences* **2008**, *363* (1494), 1211-1219.

3. Nelson, N.; Ben-Shem, A., The complex architecture of oxygenic photosynthesis. *Nature Reviews Molecular Cell Biology* **2004**, *5* (12), 971-982.

4. McEvoy, J. P.; Brudvig, G. W., Water-splitting chemistry of photosystem II. *Chem Rev* **2006**, *106* (11), 4455-83.

5. Kawakami, K.; Umena, Y.; Kamiya, N.; Shen, J. R., Structure of the catalytic, inorganic core of oxygen-evolving photosystem II at 1.9 Å resolution. *J Photochem Photobiol B* **2011**, *104* (1-2), 9-18.

6. Nielander, A. C.; Shaner, M. R.; Papadantonakis, K. M.; Francis, S. A.; Lewis, N. S., A taxonomy for solar fuels generators. *Energy & Environmental Science* **2015**, *8* (1), 16-25.

7. McKone, J. R.; Lewis, N. S.; Gray, H. B., Will Solar-Driven Water-Splitting Devices See the Light of Day? *Chemistry of Materials* **2014**, *26* (1), 407-414.

8. Cao, R.; Lai, W.; Du, P., Catalytic water oxidation at single metal sites. *Energy & Environmental Science* **2012**, *5* (8), 8134-8157.

9. Barber, J., Photosynthetic energy conversion: natural and artificial. *Chemical Society Reviews* **2009**, *38* (1), 185-196.

10. Bozoglian, F.; Romain, S.; Ertem, M. Z.; Todorova, T. K.; Sens, C.; Mola, J.; Rodríguez, M.; Romero, I.; Benet-Buchholz, J.; Fontrodona, X.; Cramer, C. J.; Gagliardi, L.; Llobet, A., The Ru−Hbpp Water Oxidation Catalyst. *Journal of the American Chemical Society* **2009**, *131* (42), 15176-15187.

11. Li, F.; Yu, M.; Jiang, Y.; Huang, F.; Li, Y.; Zhang, B.; Sun, L., Chemical and photochemical oxidation of organic substrates by ruthenium aqua complexes with water as an oxygen source. *Chemical Communications* **2011**, *47* (31), 8949-8951.

12. Thompson, M. S.; De Giovani, W. F.; Moyer, B. A.; Meyer, T. J., Novel electrocatalytic procedure for the oxidation of alcohols, aldehydes, cyclic ketones, and carbon-hydrogen bonds adjacent to olefinic or aromatic groups. *The Journal of Organic Chemistry* **1984**, *49* (25), 4972-4977.

13. Stultz, L. K.; Huynh, M. H. V.; Binstead, R. A.; Curry, M.; Meyer, T. J., Allylic Oxidation of Cyclohexene and Indene by cis-[RuIV(bpy)2(py)(O)]2+. *Journal of the American Chemical Society* **2000**, *122* (25), 5984-5996.

14. Moyer, B. A.; Meyer, T. J., Oxobis(2,2'-bipyridine)pyridineruthenium(IV) ion, [(bpy)2(py)Ru:O]2+. *Journal of the American Chemical Society* **1978**, *100* (11), 3601-3603.

15. Nagle, J. K.; Bernstein, J. S.; Young, R. C.; Meyer, T. J., Charge-transfer excited states as molecular photodiodes. *Inorganic Chemistry* **1981**, *20* (6), 1760-1764.

16. Gilbert, J. A.; Eggleston, D. S.; Murphy, W. R.; Geselowitz, D. A.; Gersten, S. W.; Hodgson, D. J.; Meyer, T. J., Structure and redox properties of the water-oxidation catalyst [(bpy)2(OH2)RuORu(OH2)(bpy)2]4+. *Journal of the American Chemical Society* **1985**, *107* (13), 3855-3864.

17. Ngo, K. T.; Lee, N. A.; Pinnace, S. D.; Szalda, D. J.; Weber, R. T.; Rochford, J., Probing the Noninnocent π-Bonding Influence of N-Carboxyamidoquinolate Ligands on the Light Harvesting and Redox Properties of Ruthenium Polypyridyl Complexes. *Inorganic Chemistry* **2016**, *55* (5), 2460-2472.

18. Collin, J. P.; Sauvage, J. P., Synthesis and study of mononuclear ruthenium(II) complexes of sterically hindering diimine chelates. Implications for the catalytic oxidation of water to molecular oxygen. *Inorganic Chemistry* **1986**, *25* (2), 135-141.

19. Nagoshi, K.; Yamashita, S.; Yagi, M.; Kaneko, M., Catalytic activity of [(bpy)2(H2O)Ru–O–Ru(H2O)(bpy)2]4+ for four-electron water oxidation. *Journal of Molecular Catalysis A: Chemical* **1999**, *144* (1), 71-76.

20. Neudeck, S.; Maji, S.; López, I.; Dechert, S.; Benet-Buchholz, J.; Llobet, A.; Meyer, F., Establishing the Family of Diruthenium Water Oxidation Catalysts Based on the Bis(bipyridyl)pyrazolate Ligand System. *Inorganic Chemistry* **2016**, *55* (5), 2508-2521.

21. Zong, R.; Thummel, R. P., A New Family of Ru Complexes for Water Oxidation. *Journal of the American Chemical Society* **2005**, *127* (37), 12802-12803.

22. Tseng, H.-W.; Zong, R.; Muckerman, J. T.; Thummel, R., Mononuclear Ruthenium(II) Complexes That Catalyze Water Oxidation. *Inorganic Chemistry* **2008**, *47* (24), 11763-11773.

23. Murakami, M.; Hong, D.; Suenobu, T.; Yamaguchi, S.; Ogura, T.; Fukuzumi, S., Catalytic Mechanism of Water Oxidation with Single-Site Ruthenium–Heteropolytungstate Complexes. *Journal of the American Chemical Society* **2011**, *133* (30), 11605-11613.

24. Vigara, L.; Ertem, M. Z.; Planas, N.; Bozoglian, F.; Leidel, N.; Dau, H.; Haumann, M.; Gagliardi, L.; Cramer, C. J.; Llobet, A., Experimental and quantum chemical characterization of the water oxidation cycle catalysed by [RuII(damp)(bpy)(H2O)]2+. *Chemical Science* **2012**, *3* (8), 2576-2586.

25. Duan, L.; Fischer, A.; Xu, Y.; Sun, L., Isolated Seven-Coordinate Ru(IV) Dimer Complex with [HOHOH]− Bridging Ligand as an Intermediate for Catalytic Water Oxidation. *Journal of the American Chemical Society* **2009**, *131* (30), 10397-10399.

26. Duan, L.; Xu, Y.; Tong, L.; Sun, L., CeIV- and Light-Driven Water Oxidation by [Ru(terpy)(pic)3]2+ Analogues: Catalytic and Mechanistic Studies. *ChemSusChem* **2011**, *4* (2), 238-244.

27. Richmond, C. J.; Matheu, R.; Poater, A.; Falivene, L.; Benet-Buchholz, J.; Sala, X.; Cavallo, L.; Llobet, A., Supramolecular Water Oxidation with Ru–bda-Based Catalysts. *Chemistry – A European Journal* **2014**, *20* (52), 17282-17286.

28. Wang, L.; Duan, L.; Wang, Y.; Ahlquist, M. S. G.; Sun, L., Highly efficient and robust molecular water oxidation catalysts based on ruthenium complexes. *Chemical Communications* **2014**, *50* (85), 12947-12950.

29. Matheu, R.; Ertem, M. Z.; Benet-Buchholz, J.; Coronado, E.; Batista, V. S.; Sala, X.; Llobet, A., Intramolecular Proton Transfer Boosts Water Oxidation Catalyzed by a Ru Complex. *Journal of the American Chemical Society* **2015**, *137* (33), 10786-10795.

30. Matheu, R.; Neudeck, S.; Meyer, F.; Sala, X.; Llobet, A., Foot of the Wave Analysis for Mechanistic Elucidation and Benchmarking Applications in Molecular Water Oxidation Catalysis. *ChemSusChem* **2016,** *9* (23), 3361-3369.

31. Creus, J.; Matheu, R.; Peñafiel, I.; Moonshiram, D.; Blondeau, P.; Benet-Buchholz, J.; García-Antón, J.; Sala, X.; Godard, C.; Llobet, A., A Million Turnover Molecular Anode for Catalytic Water Oxidation. *Angewandte Chemie International Edition* **2016,** *55* (49), 15382-15386.

32. Matheu, R.; Moreno-Hernandez, I. A.; Sala, X.; Gray, H. B.; Brunschwig, B. S.; Llobet, A.; Lewis, N. S., Photoelectrochemical Behavior of a Molecular Ru-Based Water-Oxidation Catalyst Bound to TiO2-Protected Si Photoanodes. *Journal of the American Chemical Society* **2017,** *139* (33), 11345-11348.

33. McDaniel, N. D.; Coughlin, F. J.; Tinker, L. L.; Bernhard, S., Cyclometalated Iridium(III) Aquo Complexes: Efficient and Tunable Catalysts for the Homogeneous Oxidation of Water. *Journal of the American Chemical Society* **2008,** *130* (1), 210-217.

34. Brewster, T. P.; Blakemore, J. D.; Schley, N. D.; Incarvito, C. D.; Hazari, N.; Brudvig, G. W.; Crabtree, R. H., An Iridium(IV) Species, [Cp*Ir(NHC)Cl]+, Related to a Water-Oxidation Catalyst. *Organometallics* **2011,** *30* (5), 965-973.

35. Lalrempuia, R.; McDaniel, N. D.; Müller-Bunz, H.; Bernhard, S.; Albrecht, M., Water Oxidation Catalyzed by Strong Carbene-Type Donor-Ligand Complexes of Iridium. *Angewandte Chemie International Edition* **2010,** *49* (50), 9765-9768.

36. Savini, A.; Belanzoni, P.; Bellachioma, G.; Zuccaccia, C.; Zuccaccia, D.; Macchioni, A., Activity and degradation pathways of pentamethyl-cyclopentadienyl-iridium catalysts for water oxidation. *Green Chemistry* **2011,** *13* (12), 3360-3374.

37. Schley, N. D.; Blakemore, J. D.; Subbaiyan, N. K.; Incarvito, C. D.; D'Souza, F.; Crabtree, R. H.; Brudvig, G. W., Distinguishing Homogeneous from Heterogeneous Catalysis in Electrode-Driven Water Oxidation with Molecular Iridium Complexes. *Journal of the American Chemical Society* **2011,** *133* (27), 10473-10481.

38. Grotjahn, D. B.; Brown, D. B.; Martin, J. K.; Marelius, D. C.; Abadjian, M.-C.; Tran, H. N.; Kalyuzhny, G.; Vecchio, K. S.; Specht, Z. G.; Cortes-Llamas, S. A.; Miranda-Soto, V.; van Niekerk, C.; Moore, C. E.; Rheingold, A. L., Evolution of Iridium-Based Molecular Catalysts during Water Oxidation with Ceric Ammonium Nitrate. *Journal of the American Chemical Society* **2011,** *133* (47), 19024-19027.

39. Blakemore, J. D.; Schley, N. D.; Olack, G. W.; Incarvito, C. D.; Brudvig, G. W.; Crabtree, R. H., Anodic deposition of a robust iridium-based water-oxidation catalyst from organometallic precursors. *Chemical Science* **2011,** *2* (1), 94-98.

40. Wasylenko, D. J.; Ganesamoorthy, C.; Borau-Garcia, J.; Berlinguette, C. P., Electrochemical evidence for catalyticwater oxidation mediated by a high-valent cobalt complex. *Chemical Communications* **2011,** *47* (14), 4249-4251.

41. Dogutan, D. K.; McGuire, R.; Nocera, D. G., Electocatalytic Water Oxidation by Cobalt(III) Hangman β-Octafluoro Corroles. *Journal of the American Chemical Society* **2011,** *133* (24), 9178-9180.

42. Lei, H.; Han, A.; Li, F.; Zhang, M.; Han, Y.; Du, P.; Lai, W.; Cao, R., Electrochemical, spectroscopic and theoretical studies of a simple bifunctional cobalt corrole catalyst for oxygen evolution and hydrogen production. *Physical Chemistry Chemical Physics* **2014,** *16* (5), 1883-1893.

43. Wang, D.; Groves, J. T., Efficient water oxidation catalyzed by homogeneous cationic cobalt porphyrins with critical roles for the buffer base. *Proceedings of the National Academy of Sciences* **2013,** *110* (39), 15579-15584.

44. Nakazono, T.; Parent, A. R.; Sakai, K., Cobalt porphyrins as homogeneous catalysts for water oxidation. *Chemical Communications* **2013,** *49* (56), 6325-6327.

45. Pizzolato, E.; Natali, M.; Posocco, B.; Montellano López, A.; Bazzan, I.; Di Valentin, M.; Galloni, P.; Conte, V.; Bonchio, M.; Scandola, F.; Sartorel, A., Light driven water oxidation by a single site cobalt salophen catalyst. *Chemical Communications* **2013,** *49* (85), 9941-9943.

46. Fu, S.; Liu, Y.; Ding, Y.; Du, X.; Song, F.; Xiang, R.; Ma, B., A mononuclear cobalt complex with an organic ligand acting as a precatalyst for efficient visible light-driven water oxidation. *Chemical Communications* **2014,** *50* (17), 2167-2169.

47. Yin, Q.; Tan, J. M.; Besson, C.; Geletii, Y. V.; Musaev, D. G.; Kuznetsov, A. E.; Luo, Z.; Hardcastle, K. I.; Hill, C. L., A Fast Soluble Carbon-Free Molecular Water Oxidation Catalyst Based on Abundant Metals. *Science* **2010,** *328* (5976), 342-345.

48. Natali, M.; Bazzan, I.; Goberna-Ferrón, S.; Al-Oweini, R.; Ibrahim, M.; Bassil, B. S.; Dau, H.; Scandola, F.; Galán-Mascarós, J. R.; Kortz, U.; Sartorel, A.; Zaharieva, I.; Bonchio, M., Photo-assisted water oxidation by high-nuclearity cobalt-oxo cores: tracing the catalyst fate during oxygen evolution turnover. *Green Chemistry* **2017,** *19* (10), 2416-2426.

49. Rigsby, M. L.; Mandal, S.; Nam, W.; Spencer, L. C.; Llobet, A.; Stahl, S. S., Cobalt analogs of Ru-based water oxidation catalysts: overcoming thermodynamic instability and kinetic lability to achieve electrocatalytic O2 evolution. *Chemical Science* **2012,** *3* (10), 3058-3062.

50. Limburg, J.; Vrettos, J. S.; Liable-Sands, L. M.; Rheingold, A. L.; Crabtree, R. H.; Brudvig, G. W., A Functional Model for O-O Bond Formation by the O_2-Evolving Complex in Photosystem II. *Science* **1999,** *283* (5407), 1524-1527.

51. Karlsson, E. A.; Lee, B.-L.; Åkermark, T.; Johnston, E. V.; Kärkäs, M. D.; Sun, J.; Hansson, Ö.; Bäckvall, J.-E.; Åkermark, B., Photosensitized Water Oxidation by Use of a Bioinspired Manganese Catalyst. *Angewandte Chemie International Edition* **2011,** *50* (49), 11715-11718.

52. Arafa, W. A. A.; Kärkäs, M. D.; Lee, B.-L.; Åkermark, T.; Liao, R.-Z.; Berends, H.-M.; Messinger, J.; Siegbahn, P. E. M.; Åkermark, B., Dinuclear manganese complexes for water oxidation: evaluation of electronic effects and catalytic activity. *Physical Chemistry Chemical Physics* **2014,** *16* (24), 11950-11964.

53. Ellis, W. C.; McDaniel, N. D.; Bernhard, S.; Collins, T. J., Fast Water Oxidation Using Iron. *Journal of the American Chemical Society* **2010,** *132* (32), 10990-10991.

54. Fillol, J. L.; Codolà, Z.; Garcia-Bosch, I.; Gómez, L.; Pla, J. J.; Costas, M., Efficient water oxidation catalysts based on readily available iron coordination complexes. *Nature Chemistry* **2011,** *3* (10), 807-813.

55. Hong, D.; Mandal, S.; Yamada, Y.; Lee, Y.-M.; Nam, W.; Llobet, A.; Fukuzumi, S., Water Oxidation Catalysis with Nonheme Iron Complexes under Acidic and Basic Conditions: Homogeneous or Heterogeneous? *Inorganic Chemistry* **2013,** *52* (16), 9522-9531.

56. Matheu, R.; Francàs, L.; Chernev, P.; Ertem, M. Z.; Batista, V.; Haumann, M.; Sala, X.; Llobet, A., Behavior of the Ru-bda Water Oxidation Catalyst Covalently Anchored on Glassy Carbon Electrodes. *ACS Catalysis* **2015,** *5* (6), 3422-3429.

57. Karousis, N.; Tagmatarchis, N.; Tasis, D., Current Progress on the Chemical Modification of Carbon Nanotubes. *Chemical Reviews* **2010,** *110* (9), 5366-5397.

58. Neel, A. J.; Hilton, M. J.; Sigman, M. S.; Toste, F. D., Exploiting non-covalent π interactions for catalyst design. *Nature* **2017,** *543* (7647), 637-646.

59. Li, F.; Zhang, B.; Li, X.; Jiang, Y.; Chen, L.; Li, Y.; Sun, L., Highly Efficient Oxidation of Water by a Molecular Catalyst Immobilized on Carbon Nanotubes. *Angewandte Chemie International Edition* **2011,** *50* (51), 12276-12279.

60. Duan, L.; Bozoglian, F.; Mandal, S.; Stewart, B.; Privalov, T.; Llobet, A.; Sun, L., A molecular ruthenium catalyst with water-oxidation activity comparable to that of photosystem II. *Nature Chemistry* **2012,** *4* (5), 418-423.

61. Hoque, M. A.; Gil-Sepulcre, M.; de Aguirre, A.; Elemans, J. A. A. W.; Moonshiram, D.; Matheu, R.; Shi, Y.; Benet-Buchholz, J.; Sala, X.; Malfois, M.; Solano, E.; Lim, J.; Garzón-Manjón, A.; Scheu, C.; Lanza, M.; Maseras, F.; Gimbert-Suriñach, C.; Llobet, A., Water oxidation electrocatalysis using ruthenium coordination oligomers adsorbed on multiwalled carbon nanotubes. *Nature Chemistry* **2020,** *12* (11), 1060-1066.

62. Gil-Sepulcre, M.; Lindner, J. O.; Schindler, D.; Velasco, L.; Moonshiram, D.; Rüdiger, O.; DeBeer, S.; Stepanenko, V.; Solano, E.; Würthner, F.; Llobet, A., Surface-Promoted Evolution of Ru-bda Coordination Oligomers Boosts the Efficiency of Water Oxidation Molecular Anodes. *Journal of the American Chemical Society* **2021,** *143* (30), 11651-11661.

63. Materna, K. L.; Crabtree, R. H.; Brudvig, G. W., Anchoring groups for photocatalytic water oxidation on metal oxide surfaces. *Chemical Society Reviews* **2017,** *46* (20), 6099-6110.

64. Chen, Z.; Concepcion, J. J.; Jurss, J. W.; Meyer, T. J., Single-Site, Catalytic Water Oxidation on Oxide Surfaces. *Journal of the American Chemical Society* **2009,** *131* (43), 15580-15581.

65. Odrobina, J.; Scholz, J.; Pannwitz, A.; Francàs, L.; Dechert, S.; Llobet, A.; Jooss, C.; Meyer, F., Backbone Immobilization of the Bis(bipyridyl)pyrazolate Diruthenium Catalyst for Electrochemical Water Oxidation. *ACS Catalysis* **2017,** *7* (3), 2116-2125.

66. Bélanger, D.; Pinson, J., Electrografting: a powerful method for surface modification. *Chemical Society Reviews* **2011,** *40* (7), 3995-4048.

67. Ventosa, M.; Gil-Sepulcre, M.; Benet-Buchholz, J.; Gimbert-Suriñach, C.; Llobet, A., Anode Based on a Molecular Ru Water Oxidation Catalyst Covalently Bonded to Polythiophene. *ACS Applied Energy Materials* **2021,** *4* (9), 9775-9782.

68. Jackson, M. N.; Oh, S.; Kaminsky, C. J.; Chu, S. B.; Zhang, G.; Miller, J. T.; Surendranath, Y., Strong Electronic Coupling of Molecular Sites to Graphitic Electrodes via Pyrazine Conjugation. *Journal of the American Chemical Society* **2018,** *140* (3), 1004-1010.

69. Batten, S. R.; Champness, N. R.; Chen, X.-M.; Garcia-Martinez, J.; Kitagawa, S.; Öhrström, L.; O'Keeffe, M.; Suh, M. P.; Reedijk, J., Coordination polymers, metal–organic frameworks and the need for terminology guidelines. *CrystEngComm* **2012,** *14* (9), 3001-3004.

70. Batten, S. R.; Champness, N. R.; Chen, X.-M.; Garcia-Martinez, J.; Kitagawa, S.; Öhrström, L.; O'Keeffe, M.; Suh, M. P.; Reedijk, J., Terminology of metal–organic frameworks and coordination polymers (IUPAC Recommendations 2013). *Pure and Applied Chemistry* **2013,** *85* (8), 1715-1724.

71. Cavka, J. H.; Jakobsen, S.; Olsbye, U.; Guillou, N.; Lamberti, C.; Bordiga, S.; Lillerud, K. P., A New Zirconium Inorganic Building Brick Forming Metal Organic Frameworks with Exceptional Stability. *Journal of the American Chemical Society* **2008,** *130* (42), 13850-13851.

72. Mondloch, J. E.; Bury, W.; Fairen-Jimenez, D.; Kwon, S.; DeMarco, E. J.; Weston, M. H.; Sarjeant, A. A.; Nguyen, S. T.; Stair, P. C.; Snurr, R. Q.; Farha, O. K.; Hupp, J. T., Vapor-Phase Metalation by Atomic Layer Deposition in a Metal–Organic Framework. *Journal of the American Chemical Society* **2013,** *135* (28), 10294-10297.

73. Sartorel, A.; Carraro, M.; Scorrano, G.; Zorzi, R. D.; Geremia, S.; McDaniel, N. D.; Bernhard, S.; Bonchio, M., Polyoxometalate Embedding of a Tetraruthenium(IV)-oxo-core by Template-Directed Metalation of [γ-SiW10O36]8−: A Totally Inorganic Oxygen-Evolving Catalyst. *Journal of the American Chemical Society* **2008,** *130* (15), 5006-5007.

74. Geletii, Y. V.; Botar, B.; Kögerler, P.; Hillesheim, D. A.; Musaev, D. G.; Hill, C. L., An All-Inorganic, Stable, and Highly Active Tetraruthenium Homogeneous Catalyst for Water Oxidation. *Angewandte Chemie International Edition* **2008,** *47* (21), 3896-3899.

75. Fick, A., Ueber Diffusion. *Annalen der Physik* **1855,** *170* (1), 59-86.

76. Fick, A., V. On liquid diffusion. *The London, Edinburgh, and Dublin Philosophical Magazine and Journal of Science* **1855,** *10* (63), 30-39.

77. Roy, S.; Huang, Z.; Bhunia, A.; Castner, A.; Gupta, A. K.; Zou, X.; Ott, S., Electrocatalytic Hydrogen Evolution from a Cobaloxime-Based Metal–Organic Framework Thin Film. *Journal of the American Chemical Society* **2019,** *141* (40), 15942-15950.

78. Ahrenholtz, S. R.; Epley, C. C.; Morris, A. J., Solvothermal Preparation of an Electrocatalytic Metalloporphyrin MOF Thin Film and its Redox Hopping Charge-Transfer Mechanism. *Journal of the American Chemical Society* **2014,** *136* (6), 2464-2472.

79. Usov, P. M.; Huffman, B.; Epley, C. C.; Kessinger, M. C.; Zhu, J.; Maza, W. A.; Morris, A. J., Study of Electrocatalytic Properties of Metal–Organic Framework PCN-223 for the Oxygen Reduction Reaction. *ACS Applied Materials & Interfaces* **2017,** *9* (39), 33539-33543.

80. Kornienko, N.; Zhao, Y.; Kley, C. S.; Zhu, C.; Kim, D.; Lin, S.; Chang, C. J.; Yaghi, O. M.; Yang, P., Metal–Organic Frameworks for Electrocatalytic Reduction of Carbon Dioxide. *Journal of the American Chemical Society* **2015,** *137* (44), 14129-14135.

81. Johnson, B. A.; Bhunia, A.; Fei, H.; Cohen, S. M.; Ott, S., Development of a UiO-Type Thin Film Electrocatalysis Platform with Redox-Active Linkers. *Journal of the American Chemical Society* **2018,** *140* (8), 2985-2994.

82. Wade, C. R.; Li, M.; Dincă, M., Facile Deposition of Multicolored Electrochromic Metal–Organic Framework Thin Films. *Angewandte Chemie International Edition* **2013,** *52* (50), 13377-13381.

83. Ding, B.; Chan, B.; Proschogo, N.; Solomon, M. B.; Kepert, C. J.; D'Alessandro, D. M., A cofacial metal–organic framework based photocathode for carbon dioxide reduction. *Chemical Science* **2021,** *12* (10), 3608-3614.

84. Doheny, P. W.; Clegg, J. K.; Tuna, F.; Collison, D.; Kepert, C. J.; D'Alessandro, D. M., Quantification of the mixed-valence and intervalence charge transfer properties of a cofacial metal–organic framework via single crystal electronic absorption spectroscopy. *Chemical Science* **2020,** *11* (20), 5213-5220.

85. Goswami, S.; Hod, I.; Duan, J. D.; Kung, C.-W.; Rimoldi, M.; Malliakas, C. D.; Palmer, R. H.; Farha, O. K.; Hupp, J. T., Anisotropic Redox Conductivity within a Metal–Organic Framework Material. *Journal of the American Chemical Society* **2019,** *141* (44), 17696-17702.

86. Lin, S.; Usov, P. M.; Morris, A. J., The role of redox hopping in metal–organic framework electrocatalysis. *Chemical Communications* **2018,** *54* (51), 6965-6974.

87. Andrieux, C. P.; Saveant, J. M., Electroneutrality coupling of electron hopping between localized sites with electroinactive counterion displacement. 1. Potential-step plateau currents. *The Journal of Physical Chemistry* **1988,** *92* (23), 6761-6767.

88. Savéant, J.-M., Electron hopping between fixed sitesEquivalent diffusion and migration laws. *Journal of Electroanalytical Chemistry* **1986**.

89. McCarthy, B. D.; Beiler, A. M.; Johnson, B. A.; Liseev, T.; Castner, A. T.; Ott, S., Analysis of Electrocatalytic Metal-Organic Frameworks. *Coord Chem Rev* **2020,** *406*.

90. Blauch, D. N.; Savéant, J.-M., Dynamics of electron hopping in assemblies of redox centers. Percolation and diffusion. *Journal of the American Chemical Society* **1992,** *114*, 3323-3332.

91. Dahms, H., Electronic conduction in aqueous solution. *The Journal of Physical Chemistry* **1968,** *72* (1), 362-364.

92. Ruff, I.; Korosi-Odor, I., Application of diffusion constant measurement to the determination of the rate constant of electron-exchange reactions. *Inorganic Chemistry* **1970,** *9* (1), 186-188.

93. Ruff, I.; Friedrich, V. J., Transfer diffusion. I. Theoretical. *The Journal of Physical Chemistry* **1971,** *75* (21), 3297-3302.

94. Ruff, I.; Friedrich, V. J.; Demeter, K.; Csillag, K., Transfer diffusion. II. Kinetics of electron exchange reaction between ferrocene and ferricinium ion in alcohols. *The Journal of Physical Chemistry* **1971,** *75* (21), 3303-3309.

95. Buttry, D. A.; Anson, F. C., Electron hopping vs. molecular diffusion as charge transfer mechanisms in redox polymer films. *Journal of Electroanalytical Chemistry and Interfacial Electrochemistry* **1981,** *130*, 333-338.

96. Andrieux, C. P.; Savéant, J. M., Electron transfer through redox polymer films. *Journal of Electroanalytical Chemistry and Interfacial Electrochemistry* **1980,** *111* (2), 377-381.

97. Peerce, P. J.; Bard, A. J., Polymer films on electrodes: Part III. Digital simulation model for cyclic voltammetry of electroactive polymer film and electrochemistry of poly(vinylferrocene) on platinum. *Journal of Electroanalytical Chemistry and Interfacial Electrochemistry* **1980,** *114* (1), 89-115.

98. White, H. S.; Leddy, J.; Bard, A. J., Polymer films on electrodes. 8. Investigation of charge-transport mechanisms in Nafion polymer modified electrodes. *Journal of the American Chemical Society* **1982,** *104* (18), 4811-4817.

99. D'Alessandro, D. M., Exploiting redox activity in metal–organic frameworks: concepts, trends and perspectives. *Chemical Communications* **2016,** *52* (58), 8957-8971.

100. Anson, F. C.; Blauch, D. N.; Saveant, J. M.; Shu, C. F., Ion association and electric field effects on electron hopping in redox polymers. Application to the tris(2,2'-bipyridine)osmium(3+)/tris(2,2'-bipyridine)osmium(2+) couple in Nafion. *Journal of the American Chemical Society* **1991,** *113* (6), 1922-1932.

101. Johnson, B. A.; Beiler, A. M.; McCarthy, B. D.; Ott, S., Transport Phenomena: Challenges and Opportunities for Molecular Catalysis in Metal–Organic Frameworks. *Journal of the American Chemical Society* **2020,** *142* (28), 11941-11956.

102. Hod, I.; Bury, W.; Gardner, D. M.; Deria, P.; Roznyatovskiy, V.; Wasielewski, M. R.; Farha, O. K.; Hupp, J. T., Bias-Switchable Permselectivity and Redox Catalytic Activity of a Ferrocene-Functionalized, Thin-Film Metal-Organic Framework Compound. *J Phys Chem Lett* **2015,** *6* (4), 586-91.

103. Celis-Salazar, P. J.; Cai, M.; Cucinell, C. A.; Ahrenholtz, S. R.; Epley, C. C.; Usov, P. M.; Morris, A. J., Independent Quantification of Electron and Ion Diffusion in Metallocene-Doped Metal–Organic Frameworks Thin Films. *Journal of the American Chemical Society* **2019,** *141* (30), 11947-11953.

104. Hirai, K.; Uehara, H.; Kitagawa, S.; Furukawa, S., Redox reaction in two-dimensional porous coordination polymers based on ferrocenedicarboxylates. *Dalton Transactions* **2012,** *41* (14), 3924-3927.

105. Saveant, J. M., Electron hopping between localized sites: effect of ion pairing on diffusion and migration; general rate laws and steady-state responses. *The Journal of Physical Chemistry* **1988,** *92* (15), 4526-4532.

106. Yap, W. T.; Durst, R. A.; Blubaugh, E. A.; Blubaugh, D. D., Chronoamperometry of polymer-modified electrodes: Charge transport by diffusion and migration. *Journal of Electroanalytical Chemistry and Interfacial Electrochemistry* **1983,** *144* (1), 69-75.

107. Costentin, C.; Saveant, J.-M., Cyclic Voltammetry Analysis of Electrocatalytic Films. *The Journal of Physical Chemistry C* **2015,** *119* (22), 12174-12182.

108. Andrieux, C. P.; Dumas-Bouchiat, J. M.; Savéant, J.-M., Catalysis of electrochemical reactions at redox polymer electrodes: Kinetic model for stationary voltammetric techniques. *Journal of Electroanalytical Chemistry* **1982,** *131*, 1-35.

109. Daum, P.; Murray, R. W., Chemically modified electrodes: Part XXII. Solvent effects on the electrochemistry of thin films of plasma polymerized vinylferrocene. *Journal of Electroanalytical Chemistry and Interfacial Electrochemistry* **1979,** *103* (2), 289-294.

110. Jean-Michel Savéant, C. C., *Elements of Molecular and Biomolecular Electrochemistry: an electrochemical approach to electron transfer chemistry*. Second Edition ed.; John Wiley & sons Inc.: Hoboken, NJ, 2019; p 640.

111. Elgrishi, N.; Rountree, K. J.; McCarthy, B. D.; Rountree, E. S.; Eisenhart, T. T.; Dempsey, J. L., A Practical Beginner's Guide to Cyclic Voltammetry. *Journal of Chemical Education* **2018,** *95* (2), 197-206.

112. Andrieux, C. P.; Savéant, J. M., Kinetics of electrochemical reactions mediated by redox polymer films: Reversible cross-exchange reactions. *Journal of Electroanalytical Chemistry and Interfacial Electrochemistry* **1982,** *142* (1), 1-30.

113. Compton, R. G. B. C. E., *Understanding voltammetry*. 2018.

114. Johnson, B. A.; Bhunia, A.; Ott, S., Electrocatalytic water oxidation by a molecular catalyst incorporated into a metal–organic framework thin film. *Dalton Transactions* **2017,** *46* (5), 1382-1388.

115. Beiler, A. M.; McCarthy, B. D.; Johnson, B. A.; Ott, S., Enhancing photovoltages at p-type semiconductors through a redox-active metal-organic framework surface coating. *Nature Communications* **2020,** *11* (1), 5819.

116. Brett, C. M. A.; Brett, A. M. O., *Electrochemistry : principles, methods, and applications*. Oxford : Oxford university press: 1993.

117. Zeng, Y.; Yu, D.; Yu, Y.; Zhou, T.; Shi, G., Differential pulse voltammetric determination of methyl parathion based on multiwalled carbon nanotubes–poly(acrylamide) nanocomposite film modified electrode. *Journal of Hazardous Materials* **2012,** *217-218*, 315-322.

118. Lin, S.; Pineda-Galvan, Y.; Maza, W. A.; Epley, C. C.; Zhu, J.; Kessinger, M. C.; Pushkar, Y.; Morris, A. J., Electrochemical Water Oxidation by a Catalyst-Modified Metal–Organic Framework Thin Film. *ChemSusChem* **2017,** *10* (3), 514-522.

119. Shimoni, R.; He, W.; Liberman, I.; Hod, I., Tuning of Redox Conductivity and Electrocatalytic Activity in Metal–Organic Framework Films Via Control of Defect Site Density. *The Journal of Physical Chemistry C* **2019,** *123* (9), 5531-5539.

120. Costentin, C.; Savéant, J.-M., Multielectron, Multistep Molecular Catalysis of Electrochemical Reactions: Benchmarking of Homogeneous Catalysts. *ChemElectroChem* **2014,** *1* (7), 1226-1236.

121. Costentin, C.; Drouet, S.; Robert, M.; Savéant, J.-M., Turnover Numbers, Turnover Frequencies, and Overpotential in Molecular Catalysis of Electrochemical Reactions. Cyclic Voltammetry and Preparative-Scale Electrolysis. *Journal of the American Chemical Society* **2012,** *134* (27), 11235-11242.

122. Bard, A. J.; Fox, M. A., Artificial Photosynthesis: Solar Splitting of Water to Hydrogen and Oxygen. *Accounts of Chemical Research* **1995,** *28* (3), 141-145.

123. Lee, J.; Farha, O. K.; Roberts, J.; Scheidt, K. A.; Nguyen, S. T.; Hupp, J. T., Metal–organic framework materials as catalysts. *Chemical Society Reviews* **2009,** *38* (5), 1450-1459.

124. Downes, C. A.; Marinescu, S. C., Electrocatalytic Metal–Organic Frameworks for Energy Applications. *ChemSusChem* **2017,** *10* (22), 4374-4392.

125. Zhang, T.; Lin, W., Metal–organic frameworks for artificial photosynthesis and photocatalysis. *Chemical Society Reviews* **2014,** *43* (16), 5982-5993.

126. Bhunia, A.; Johnson, B. A.; Czapla-Masztafiak, J.; Sá, J.; Ott, S., Formal water oxidation turnover frequencies from MIL-101(Cr) anchored Ru(bda) depend on oxidant concentration. *Chemical Communications* **2018,** *54* (56), 7770-7773.

127. Jia, H.; Yao, Y.; Zhao, J.; Gao, Y.; Luo, Z.; Du, P., A novel two-dimensional nickel phthalocyanine-based metal–organic framework for highly efficient water oxidation catalysis. *Journal of Materials Chemistry A* **2018,** *6* (3), 1188-1195.

128. Lin, S.; Ravari, A. K.; Zhu, J.; Usov, P. M.; Cai, M.; Ahrenholtz, S. R.; Pushkar, Y.; Morris, A. J., Insight into Metal–Organic Framework Reactivity: Chemical Water Oxidation Catalyzed by a [Ru(tpy)(dcbpy)(OH2)]2+-Modified UiO-67. *ChemSusChem* **2018,** *11* (2), 464-471.

129. Natarajan, K.; Gupta, A. K.; Ansari, S. N.; Saraf, M.; Mobin, S. M., Mixed-Ligand-Architected 2D Co(II)-MOF Expressing a Novel Topology for an Efficient Photoanode for Water Oxidation Using Visible Light. *ACS Applied Materials & Interfaces* **2019,** *11* (14), 13295-13303.

130. Micheroni, D.; Lan, G.; Lin, W., Efficient Electrocatalytic Proton Reduction with Carbon Nanotube-Supported Metal–Organic Frameworks. *Journal of the American Chemical Society* **2018,** *140* (46), 15591-15595.

131. Wang, C.; Xie, Z.; deKrafft, K. E.; Lin, W., Doping Metal–Organic Frameworks for Water Oxidation, Carbon Dioxide Reduction, and Organic Photocatalysis. *Journal of the American Chemical Society* **2011,** *133* (34), 13445-13454.

132. Wang, W.; Xu, X.; Zhou, W.; Shao, Z., Recent Progress in Metal-Organic Frameworks for Applications in Electrocatalytic and Photocatalytic Water Splitting. *Advanced Science* **2017,** *4* (4), 1600371.

133. Kung, C.-W.; Mondloch, J. E.; Wang, T. C.; Bury, W.; Hoffeditz, W.; Klahr, B. M.; Klet, R. C.; Pellin, M. J.; Farha, O. K.; Hupp, J. T., Metal–Organic Framework Thin Films as Platforms for Atomic Layer Deposition of Cobalt Ions To Enable Electrocatalytic Water Oxidation. *ACS Applied Materials & Interfaces* **2015,** *7* (51), 28223-28230.

134. Lu, X.-F.; Liao, P.-Q.; Wang, J.-W.; Wu, J.-X.; Chen, X.-W.; He, C.-T.; Zhang, J.-P.; Li, G.-R.; Chen, X.-M., An Alkaline-Stable, Metal Hydroxide Mimicking Metal–Organic Framework for Efficient Electrocatalytic Oxygen Evolution. *Journal of the American Chemical Society* **2016,** *138* (27), 8336-8339.

135. Shen, J.-Q.; Liao, P.-Q.; Zhou, D.-D.; He, C.-T.; Wu, J.-X.; Zhang, W.-X.; Zhang, J.-P.; Chen, X.-M., Modular and Stepwise Synthesis of a Hybrid Metal–Organic Framework for Efficient Electrocatalytic Oxygen Evolution. *Journal of the American Chemical Society* **2017,** *139* (5), 1778-1781.

136. Usov, P. M.; Ahrenholtz, S. R.; Maza, W. A.; Stratakes, B.; Epley, C. C.; Kessinger, M. C.; Zhu, J.; Morris, A. J., Cooperative electrochemical water oxidation by Zr nodes and Ni–porphyrin linkers of a PCN-224 MOF thin film. *Journal of Materials Chemistry A* **2016,** *4* (43), 16818-16823.

137. Elcheikh Mahmoud, M.; Audi, H.; Assoud, A.; Ghaddar, T. H.; Hmadeh, M., Metal–Organic Framework Photocatalyst Incorporating Bis(4′-(4-carboxyphenyl)-terpyridine)ruthenium(II) for Visible-Light-Driven Carbon Dioxide Reduction. *Journal of the American Chemical Society* **2019,** *141* (17), 7115-7121.

138. Maza, W. A.; Padilla, R.; Morris, A. J., Concentration Dependent Dimensionality of Resonance Energy Transfer in a Postsynthetically Doped Morphologically Homologous Analogue of UiO-67 MOF with a Ruthenium(II) Polypyridyl Complex. *Journal of the American Chemical Society* **2015,** *137* (25), 8161-8168.

139. Maza, W. A.; Haring, A. J.; Ahrenholtz, S. R.; Epley, C. C.; Lin, S. Y.; Morris, A. J., Ruthenium(ii)-polypyridyl zirconium(iv) metal–organic frameworks as a new class of sensitized solar cells. *Chemical Science* **2016,** *7* (1), 719-727.

140. Yao, L.-Y.; Yang, F.; Liang, W.-B.; Hu, G.-B.; Yang, Y.; Huang, W.; Yuan, R.; Xiao, D.-R., Ruthenium complex doped metal-organic nanoplate with high electrochemiluminescent intensity and stability for ultrasensitive assay of mucin 1. *Sensors and Actuators B: Chemical* **2019,** *292*, 105-110.

141. Zhang, S.; Li, L.; Zhao, S.; Sun, Z.; Luo, J., Construction of Interpenetrated Ruthenium Metal–Organic Frameworks as Stable Photocatalysts for CO2 Reduction. *Inorganic Chemistry* **2015,** *54* (17), 8375-8379.

142. Shao, H.; Lu, J.; Zhang, Q.; Hu, Y.; Wang, S.; Guo, Z., Ruthenium-based metal organic framework (Ru-MOF)-derived novel Faraday-cage electrochemiluminescence biosensor for ultrasensitive detection of miRNA-141. *Sensors and Actuators B: Chemical* **2018,** *268*, 39-46.

143. Romain, S.; Vigara, L.; Llobet, A., Oxygen−Oxygen Bond Formation Pathways Promoted by Ruthenium Complexes. *Accounts of Chemical Research* **2009,** *42* (12), 1944-1953.

144. Sala, X.; Romero, I.; Rodríguez, M.; Escriche, L.; Llobet, A., Molecular Catalysts that Oxidize Water to Dioxygen. *Angewandte Chemie International Edition* **2009,** *48* (16), 2842-2852.

145. Gersten, S. W.; Samuels, G. J.; Meyer, T. J., Catalytic oxidation of water by an oxo-bridged ruthenium dimer. *Journal of the American Chemical Society* **1982,** *104* (14), 4029-4030.

146. Sens, C.; Romero, I.; Rodríguez, M.; Llobet, A.; Parella, T.; Benet-Buchholz, J., A New Ru Complex Capable of Catalytically Oxidizing Water to Molecular Dioxygen. *Journal of the American Chemical Society* **2004,** *126* (25), 7798-7799.

147. Polyansky, D. E.; Muckerman, J. T.; Rochford, J.; Zong, R.; Thummel, R. P.; Fujita, E., Water Oxidation by a Mononuclear Ruthenium Catalyst: Characterization of the Intermediates. *Journal of the American Chemical Society* **2011,** *133* (37), 14649-14665.

148. Concepcion, J. J.; Jurss, J. W.; Templeton, J. L.; Meyer, T. J., One Site is Enough. Catalytic Water Oxidation by [Ru(tpy)(bpm)(OH2)]2+ and [Ru(tpy)(bpz)(OH2)]2+. *Journal of the American Chemical Society* **2008,** *130* (49), 16462-16463.

149. Thummel, R. P.; Jahng, Y., N-Oxides of 2,2':6',2"-terpyridine. *The Journal of Organic Chemistry* **1985,** *50* (19), 3635-3636.

150. Fife, W. K., Regioselective cyanation of pyridine 1-oxides with trimethylsilanecarbonitrile: a modified Reissert-Henze reaction. *The Journal of Organic Chemistry* **1983,** *48* (8), 1375-1377.

151. Yun, R.; Jiang, Y.; Luo, S.; Chen, C., Three-dimensional coordination polymers constructed from C2-symmetric linkers of pyridyl dicarboxylate ligands. *RSC Advances* **2014,** *4* (69), 36845-36848.

152. Liseev, T.; Howe, A.; Hoque, M. A.; Gimbert-Suriñach, C.; Llobet, A.; Ott, S., Synthetic strategies to incorporate Ru-terpyridyl water oxidation catalysts into MOFs: direct synthesis vs. post-synthetic approach. *Dalton Transactions* **2020,** *49* (39), 13753-13759.

153. Ayala, S.; Zhang, Z.; Cohen, S. M., Hierarchical structure and porosity in UiO-66 polyMOFs. *Chemical Communications* **2017,** *53* (21), 3058-3061.

154. Ayala, S.; Bentz, K. C.; Cohen, S. M., Block co-polyMOFs: morphology control of polymer–MOF hybrid materials. *Chemical Science* **2019,** *10* (6), 1746-1753.

155. Thommes, M.; Kaneko, K.; Neimark, A. V.; Olivier, J. P.; Rodriguez-Reinoso, F.; Rouquerol, J.; Sing, K. S. W., Physisorption of gases, with special reference to the evaluation of surface area and pore size distribution (IUPAC Technical Report). *Pure and Applied Chemistry* **2015,** *87* (9-10), 1051-1069.

156. Lv, X.-L.; Tong, M.; Huang, H.; Wang, B.; Gan, L.; Yang, Q.; Zhong, C.; Li, J.-R., A high surface area Zr(IV)-based metal–organic framework showing stepwise gas adsorption and selective dye uptake. *Journal of Solid State Chemistry* **2015,** *223*, 104-108.

157. Ren, J.; Ledwaba, M.; Musyoka, N. M.; Langmi, H. W.; Mathe, M.; Liao, S.; Pang, W., Structural defects in metal–organic frameworks (MOFs): Formation, detection and control towards practices of interests. *Coordination Chemistry Reviews* **2017,** *349*, 169-197.

158. Yuan, L.; Tian, M.; Lan, J.; Cao, X.; Wang, X.; Chai, Z.; Gibson, J. K.; Shi, W., Defect engineering in metal–organic frameworks: a new strategy to develop applicable actinide sorbents. *Chemical Communications* **2018,** *54* (4), 370-373.

159. Wang, K.; Li, C.; Liang, Y.; Han, T.; Huang, H.; Yang, Q.; Liu, D.; Zhong, C., Rational construction of defects in a metal–organic framework for highly efficient adsorption and separation of dyes. *Chemical Engineering Journal* **2016,** *289*, 486-493.

160. Hod, I.; Bury, W.; Karlin, D. M.; Deria, P.; Kung, C. W.; Katz, M. J.; So, M.; Klahr, B.; Jin, D.; Chung, Y. W.; Odom, T. W.; Farha, O. K.; Hupp, J. T., Directed growth of electroactive metal-organic framework thin films using electrophoretic deposition. *Advanced materials* **2014,** *26* (36), 6295-6300.

161. Chen, Q.; Sun, J.; Li, P.; Hod, I.; Moghadam, P. Z.; Kean, Z. S.; Snurr, R. Q.; Hupp, J. T.; Farha, O. K.; Stoddart, J. F., A Redox-Active Bistable Molecular Switch Mounted inside a Metal–Organic Framework. *Journal of the American Chemical Society* **2016,** *138* (43), 14242-14245.

162. Matheu, R.; Ertem, M. Z.; Gimbert-Surinach, C.; Sala, X.; Llobet, A., Seven Coordinated Molecular Ruthenium-Water Oxidation Catalysts: A Coordination Chemistry Journey. *Chem Rev* **2019,** *119* (6), 3453-3471.

163. Islamoglu, T.; Otake, K.-i.; Li, P.; Buru, C. T.; Peters, A. W.; Akpinar, I.; Garibay, S. J.; Farha, O. K., Revisiting the structural homogeneity of NU-1000, a Zr-based metal–organic framework. *CrystEngComm* **2018,** *20* (39), 5913-5918.

164. Mondloch, J. E.; Bury, W.; Fairen-Jimenez, D.; Kwon, S.; DeMarco, E. J.; Weston, M. H.; Sarjeant, A. A.; Nguyen, S. T.; Stair, P. C.; Snurr, R. Q.; Farha, O. K.; Hupp, J. T., Vapor-phase metalation by atomic layer deposition in a metal-organic framework. *J. Am. Chem. Soc.* **2013,** *135* (28), 10294-10297.

165. Burrows, A. D.; Fisher, L. C.; Richardson, C.; Rigby, S. P., Selective incorporation of functional dicarboxylates into zinc metal-organic frameworks. *Chem. Commun.* **2011,** *47* (12), 3380-3382.

166. Lin, S.; Usov, P. M.; Morris, A. J., The role of redox hopping in metal-organic framework electrocatalysis. *Chem. Commun.* **2018,** *54* (51), 6965-6974.

167. Mijangos, E.; Roy, S.; Pullen, S.; Lomoth, R.; Ott, S., Evaluation of two- and three-dimensional electrode platforms for the electrochemical characterization of organometallic catalysts incorporated in non-conducting metal-organic frameworks. *Dalton Trans* **2017,** *46* (15), 4907-4911.

168. Mohammad-Pour, G. S.; Hatfield, K. O.; Fairchild, D. C.; Hernandez-Burgos, K.; Rodriguez-Lopez, J.; Uribe-Romo, F. J., A Solid-Solution Approach for Redox Active Metal-Organic Frameworks with Tunable Redox Conductivity. *J Am Chem Soc* **2019**.

169. McCarthy, B. D.; Beiler, A. M.; Johnson, B. A.; Liseev, T.; Castner, A. T.; Ott, S., Analysis of electrocatalytic metal-organic frameworks. *Coordination chemistry reviews* **2020,** *406*, 213137.

170. Feng, D.; Gu, Z.-Y.; Li, J.-R.; Jiang, H.-L.; Wei, Z.; Zhou, H.-C., Zirconium-Metalloporphyrin PCN-222: Mesoporous Metal–Organic Frameworks with Ultrahigh Stability as Biomimetic Catalysts. *Angewandte Chemie International Edition* **2012,** *51* (41), 10307-10310.

171. Tong, L.; Duan, L.; Xu, Y.; Privalov, T.; Sun, L., Structural modifications of mononuclear ruthenium complexes: a combined experimental and theoretical study on the kinetics of ruthenium-catalyzed water oxidation. *Angewandte Chemie International Edition* **2011,** *50* (2), 445-449.

172. Tsubonouchi, Y.; Lin, S.; Parent, A. R.; Brudvig, G. W.; Sakai, K., Light-induced water oxidation catalyzed by an oxido-bridged triruthenium complex with a Ru–O–Ru–O–Ru motif. *Chemical Communications* **2016,** *52* (51), 8018-8021.

173. Song, N.; Concepcion, J. J.; Binstead, R. A.; Rudd, J. A.; Vannucci, A. K.; Dares, C. J.; Coggins, M. K.; Meyer, T. J., Base-enhanced catalytic water oxidation by a carboxylate–bipyridine Ru (II) complex. *Proceedings of the National Academy of Sciences* **2015,** *112* (16), 4935-4940.

174. Shekhah, O.; Wang, H.; Kowarik, S.; Schreiber, F.; Paulus, M.; Tolan, M.; Sternemann, C.; Evers, F.; Zacher, D.; Fischer, R. A.; Wöll, C., Step-by-Step Route for the Synthesis of Metal−Organic Frameworks. *Journal of the American Chemical Society* **2007,** *129* (49), 15118-15119.

175. Shekhah, O.; Wang, H.; Zacher, D.; Fischer, R. A.; Wöll, C., Growth Mechanism of Metal–Organic Frameworks: Insights into the Nucleation by Employing a Step-by-Step Route. *Angewandte Chemie International Edition* **2009,** *48* (27), 5038-5041.

176. Virmani, E.; Rotter, J. M.; Mähringer, A.; Von Zons, T.; Godt, A.; Bein, T.; Wuttke, S.; Medina, D. D., On-surface synthesis of highly oriented thin metal–organic framework films through vapor-assisted conversion. *Journal of the American Chemical Society* **2018,** *140* (14), 4812-4819.

177. Liu, T.; Li, G.; Shen, N.; Ahlquist, M. S. G.; Sun, L., Hydrophobic Interactions of Ru-bda-Type Catalysts for Promoting Water Oxidation Activity. *Energy & Fuels* **2021,** *35* (23), 19096-19103.

178. Zhan, S.; Zhang, B.; Sun, L.; Ahlquist, M. S. G., Hydrophobic/Hydrophilic Directionality Affects the Mechanism of Ru-Catalyzed Water Oxidation Reaction. *ACS Catalysis* **2020,** *10* (22), 13364-13370.

179. Zhang, B.; Sun, L., Ru-bda: Unique Molecular Water-Oxidation Catalysts with Distortion Induced Open Site and Negatively Charged Ligands. *Journal of the American Chemical Society* **2019,** *141* (14), 5565-5580.

180. Schulze, M.; Kunz, V.; Frischmann, P. D.; Würthner, F., A supramolecular ruthenium macrocycle with high catalytic activity for water oxidation that mechanistically mimics photosystem II. *Nature Chemistry* **2016,** *8* (6), 576-583.

181. Kunz, V.; Lindner, J. O.; Schulze, M.; Röhr, M. I. S.; Schmidt, D.; Mitrić, R.; Würthner, F., Cooperative water oxidation catalysis in a series of trinuclear metallosupramolecular ruthenium macrocycles. *Energy & Environmental Science* **2017,** *10* (10), 2137-2153.

182. Kunz, V.; Schulze, M.; Schmidt, D.; Würthner, F., Trinuclear Ruthenium Macrocycles: Toward Supramolecular Water Oxidation Catalysis in Pure Water. *ACS Energy Letters* **2017,** *2* (2), 288-293.

183. Matheu, R.; Ertem, M. Z.; Gimbert-Suriñach, C.; Benet-Buchholz, J.; Sala, X.; Llobet, A., Hydrogen Bonding Rescues Overpotential in Seven-Coordinated Ru Water Oxidation Catalysts. *ACS Catalysis* **2017,** *7* (10), 6525-6532.

184. Xie, Y.; Shaffer, D. W.; Lewandowska-Andralojc, A.; Szalda, D. J.; Concepcion, J. J., Water Oxidation by Ruthenium Complexes Incorporating Multifunctional Bipyridyl Diphosphonate Ligands. *Angewandte Chemie International Edition* **2016,** *55* (28), 8067-8071.

185. Kamdar, J. M.; Marelius, D. C.; Moore, C. E.; Rheingold, A. L.; Smith, D. K.; Grotjahn, D. B., Ruthenium Complexes of 2,2′-Bipyridine-6,6′-diphosphonate Ligands for Water Oxidation. *ChemCatChem* **2016,** *8* (19), 3045-3049.

186. Shaffer, D. W.; Xie, Y.; Szalda, D. J.; Concepcion, J. J., Lability and Basicity of Bipyridine-Carboxylate-Phosphonate Ligand Accelerate Single-Site Water Oxidation by Ruthenium-Based Molecular Catalysts. *Journal of the American Chemical Society* **2017,** *139* (43), 15347-15355.

187. Vereshchuk, N.; Holub, J.; Gil-Sepulcre, M.; Benet-Buchholz, J.; Llobet, A., Fate of the Molecular Ru–Phosphonate Water Oxidation Catalyst under Turnover Conditions. *ACS Catalysis* **2021,** *11* (9), 5240-5247.

188. Vereschchuk, N. Rational design of the molecular Ru-based Water Oxidation Catalysts. Universitat Rovira I Virgili, Tarragona 2021.

189. Anantharaj, S.; Karthik, P. E.; Noda, S., The Significance of Properly Reporting Turnover Frequency in Electrocatalysis Research. *Angewandte Chemie International Edition* **2021,** *60* (43), 23051-23067.

Acta Universitatis Upsaliensis

Digital Comprehensive Summaries of Uppsala Dissertations
from the Faculty of Science and Technology 2190

Editor: The Dean of the Faculty of Science and Technology

A doctoral dissertation from the Faculty of Science and
Technology, Uppsala University, is usually a summary of a
number of papers. A few copies of the complete dissertation
are kept at major Swedish research libraries, while the
summary alone is distributed internationally through
the series Digital Comprehensive Summaries of Uppsala
Dissertations from the Faculty of Science and Technology.
(Prior to January, 2005, the series was published under the
title "Comprehensive Summaries of Uppsala Dissertations
from the Faculty of Science and Technology".)